UNIVERSITY OF GENOA

PH.D. PROGRAM IN PHYSICS

The nucleus under the microscope. A biophysical approach.

Luca Pesce

XXXI cycle

Tutors: Prof. Alberto Diaspro, Dr. Paolo Bianchini.

Contents

Abbreviations

4-HT	4-hydroxy-TEMPO
AcX	6-((acryloyl)amino)hexanoic acid
APS	ammonium persulfate
BSA	Bovine serum albumin
CLEM	Correlative light and electron microscopy
CLSM	confocal laser scanning microscopy
CSREM	Correlative super-resolution optical and electron microscopy
EF	Expansion factor
EM	Electron microscopy
ExM	Expansion microscopy
ExFISH	Expansion fluorescence in situ hybridization
ExSTED	Expansion microscopy combined to STED nanoscopy
FM	Fluorescence microscopy
GA	Glutaraldehyde
GFP	Green fluorescent protein
HGPS	Hutchinson–Gilford progeria syndrome
INM	Inner nuclear membrane
iExM	iterative expansion microscopy
LA	Lamin A (protein)
LB1	Lamin B1 (protein)
LB2	Lamin B2 (protein)
LC	Lamin C (protein)
LADs	Lamina-associated domains
LMNA/C	Lamin A/C (gene)
LMNB1	Lamin B1 (gene)
LMNB2	Lamin B2 (gene)
MAP	magnified analysis of the proteome
MA-NHS	methacrylic acid N-hydroxysuccinimidyl ester
NE	Nuclear envelope
NL	Nuclear lamins
NLS	Nuclear localization sequence
NPC	Nuclear pore complex
NR	Nucleoplasmic reticulum
ONM	Outer nuclear membrane
PFA	Paraformaldehyde
PBS	Phosphate-buffered saline
ProExM	Protein-retention expansion microscopy
PSF	Point spread function
STED	Stimulated emission depletion

TAE	Buffer containing a mixture of Tris base, acetic acid and EDTA
TDE	2,2′-thiodiethanol
TEMED	N, N,N', N'-tetramethylethylenediamine
ΔLA50	Progerin (truncated form of lamin A)

Exams

The table shows the main courses attended during my Ph.D. In addition, I followed several schools concerning fluorescence microscopy and super resolution techniques.

Courses	Professors	Hours
Fisica Moderna	Magnoli	40
Proprietà ottiche di sistemi complessi alla nanoscala	Canepa, Bisio	40
Dynamic light scattering and AFM	Rolandi, Canale	20
Advanced Optical Fluorescence Microscopy Methods I	Diaspro	9
Advanced Optical Fluorescence Microscopy Methods II	Lanzanò	9
Super-resolution Optical Fluorescence Microscopy	Bianchini	9
Laboratory of Optical Fluorescence Microscopy Methods	Damora	9

Publications

1. Rodriguez S, Gatto F, **Pesce L**, Canale C, Pompa PP, Bardi G, Lopez D, Torres G. Monitoring cell substrate interactions in exopolysaccharide-based films reinforced with chitin whiskers and starch nanoparticles used as cell substrates. International Journal of Polymeric Materials and Polymeric Biomaterials. 2017.

2. Sarmento MJ, Oneto M, Pelicci S, **Pesce L**, Scipioni L, Faretta M, Furia L, Dellino GI, Pelicci PG, Bianchini P, Diaspro A, Lanzanò L. Exploiting the tunability of stimulated emission depletion microscopy for super-resolution imaging of nuclear structures. Nature Communications. 2018.

3. Le Gratiet A, **Pesce L**, Oneto M, Marongiu R, Zanini G, Bianchini P, Diaspro A. Circular Intensity Differential Scattering (CIDS) scanning microscopy to image Chromatin-DNA nuclear organization. OSA Continuum. 2018.

4. **Pesce L**, Cozzolino M, Lanzano L, Diaspro A and Bianchini P. 2018. Enigma at the nanoscale: can the NPC act as an intrinsic reporter for isotropic expansion microscopy? BioRxiv. 2018. Submitted to Nanoscale.

Poster

- Cainero I, Oneto M, **Pesce L**, Zanini G, Lanzanò L, Diaspro A, Bianchini P. (2017) Combining Expansion Microscopy and STED nanoscopy for the study of cellular organization. Biophysical Society, New Orleans.

- **Pesce L**, Cainero I, Oneto M, Cozzolino M, Lanzanò L, Diaspro A, Bianchini P. (2017) Expansion and STED nanoscopy: a new tool for pushing the resolution at the limit, the fluorescent label. FOM, Bordeaux.

- **Pesce L**, Cozzolino M, Lanzanò L, Diaspro A, Bianchini P (2018) Expansion Microscopy: a tool to investigate Hutchinson-Gilford Progeria Syndrome at molecular level. Biophysical Society, San Francisco.

- Cozzolino M, **Pesce L**, Oneto M, Montali C, Bianchini P, Abbruzzetti S, Viappiani C, Diaspro A. (2018) Study of Tumor Cellular Damage Induced by Photosensitizing Molecules. Biophysical Society, San Francisco.

- Diaspro A, Cainero I, Lanzano L, Bianchini P, Vicidomini G, Zanacchi FC, **Pesce L**, Pelicci P, Oneto M, Di Bona M, Faretta M, Barboro P, Le Gratiet A. (2018) A liquid tunable microscope as a new paradigm in optical microscopy to paint 4D chromatin organization in the cell nucleus. Biophysical Society, San Francisco.

- Bianchini P, **Pesce L**, Cozzolino M, Le Gratiet A, Lanzanò L, Diaspro A. (2018) Tunable and multimodal microscopy for accessing different levels of cellular organization, from molecules to organoids. Elmi, Dublino.

Award

In 2018 Travel Award for the abstract "Quantification of the chemical process involved in Expansion Microscopy (ExM) technique, studying the nuclear pore complex structure". Società Italiana di Biofisica Pura e Applicata (SIBPA), Ancona.

Teaching activity

In 2017/18 Lesson and practical course on “Sample preparation for super resolution techniques and Expansion Microscopy”, 4th and 5th Nikon School-Practical workshop on advanced microscopy, Genova.

1 Introduction

At the beginning of 1950, many researchers challenged the possibility to overcome the fundamental Abbe limit. An attempt was made by Giuliano Toraldo di Francia, who showed that the width of the point-spread function can be reduced applying a filtering technique (called apodozation) (*1*). In 1994, a revolutionary event took place in the field of optical microscopy: Hell described a method for circumventing the light diffraction barrier (*2*). In this way, details that were not visible in diffraction-limited techniques could be imaged using a fluorescence microscopy. Nowadays, these methods termed Far-field fluorescence microscopy or nanoscopy techniques, has become an indispensable tool for scientist to address important biological and biophysical questions at the single molecule level. To highlight the outstanding importance of such techniques, the Royal Swedish Academy of Sciences awarded Eric Betzig, Stefan W. Hell, and William E. Moerner the Nobel Prize in Chemistry 2014 "for the development of super-resolved fluorescence microscopy". In addition, several important technical improvements, including confocal laser scanning microscopy (CLSM) (*3*), multiphoton microscopy, 4Pi (*4*) and I^5M (*5*) have had an important role in the field of optical microscopy.

On the other side, in 2015 Boyden and colleagues developed a new method termed Expansion Microscopy (ExM), which allows expanding uniformly biological samples by increasing the relative distances among fluorescent molecules labelling specific cellular components (*6*). ExM permits to achieve a lateral resolution of about 65 nm, using a conventional - diffracted microscope.

However, all super resolution methods demand a particular attention in the sample preparation. Achieving super resolved images require the optimization of every steps involved in the labelling process, from the expression of a fluorescent proteins to the fixation of the biological samples. In the last years, these labelling strategies have obtained a critical role in the field of fluorescence microscopy. In particular, the design and the localization precision of specific affinity probes are crucial features that can restrict the applicability of these techniques.

During my Ph.D., I have had the opportunity to test several labelling approaches and optimize different staining protocol for super resolution techniques. My effort was focused on STED nanoscopy and ExM, and how to optimize the labelling protocol, the

fluorophores choice for a high labelling density. The optimization of the steps involved in the labelling processes allows me combining ExM with STED nanoscopy (ExSTED), to enhance the final resolution (*7*). In addition, these techniques were used to decipher molecular assemblies in the cellular nuclei. In particular, my attention was focused on an important layer termed nuclear envelope (NE) (*8*). This nuclear region encases the genetic material, maintains the regular shape of the nucleus and regulates the gene expression. NE is composed by two lipid bilayer and different class of proteins, which pass through or are strictly linked to the nuclear membranes. Nuclear pore complexes (NPCs) and nuclear lamins, two classes of proteins belonging to the NE, were investigated in this work. In particular, NPCs was used to evaluate the isotropy and calculate the expansion factor (EF) at the nanoscale level in ExM. On the other side, nuclear lamins, in particular lamin A (LA) and its mutation ΔLA50, were used to investigate the physiological and pathological nuclear membrane invagination in normal and aging cells. The rare premature ageing disorder Hutchinson-Gilford progeria syndrome, caused by *LMNA* mutation, is a powerful model system to identify and characterize the molecular mechanism involved in physiological ageing. In addition, a better comprehension of common disease associate with ageing, including neurological disorders, diabetes, cardiovascular diseases and cancer, can be investigated using this rare genetic syndrome (*9*).

2 Resolution concept in optical microscopy

Wide field deconvolution and CLSM have long been the standard method in life sciences. However, the diffraction limit of light is a limitation for investigating the dynamic processes that occur in cells, tissues and animals. Fortunately, several new technologies termed nanoscopy are able to circumvent this limit.

2.1 Abbe's diffraction limit

Optical microscopy is one of the oldest tools used to investigate life. In particular, the fluorescence process is the favorite methods in the field of the microscopy, because the commonly wavelength used (visible light between 450 nm and 700 nm) are generally not toxic for biological samples. Using specific fluorescent labelling methods like immunofluorescence, in situ hybridization and fluorescent proteins, the dynamics process and the spatial distribution of specific biomolecules can be investigated in living or fixed samples (*10*). Indeed, compared to other scientific disciplines, like electron microscopy (EM) or biochemical approach, fluorescent microscopy (FM) has been considered one of the least invasive investigation methods. Although EM is able to achieve up 100X greater resolving power respect to a conventional fluorescent microscopy, it is characterized by a long sample preparation, incompatibility with live cell imaging and relatively costly. Instead, biochemical method needs the complete disintegration and fractionating of the specimens.

However, the maximum resolution of lens-based microscopy is limited by the diffraction limit of light. The principle described by Abbe (*11*) claims that the minimum distance between two fluorescent fluorophores depends on the wavelength of the excitation light and the numerical aperture (NA) of the lens used.

$$\Delta d_{x,y} = \frac{\lambda}{2n \sin \alpha}$$

This limitation restricts the ability of optical microscopy to distinguish between two fluorescent molecules separated by a distance of about 250 nm. Moreover, the axial resolution can be approximated by the following equation:

$$\Delta d_z = \frac{\lambda}{2n(sin\alpha)^2}$$

What defines the NA of the objective is the size and the specific geometrical shape of the lens. In addition to the diffraction phenomenon, the process of interference plays an important role in the image formation (Fig. 1). In fact, both interference and diffraction are the principal responsible of the real image formation of the sample. It is possible to have a constructive or destructive interference when two wavefronts are perfectly in phase or out of phase by 180 degrees, respectively.

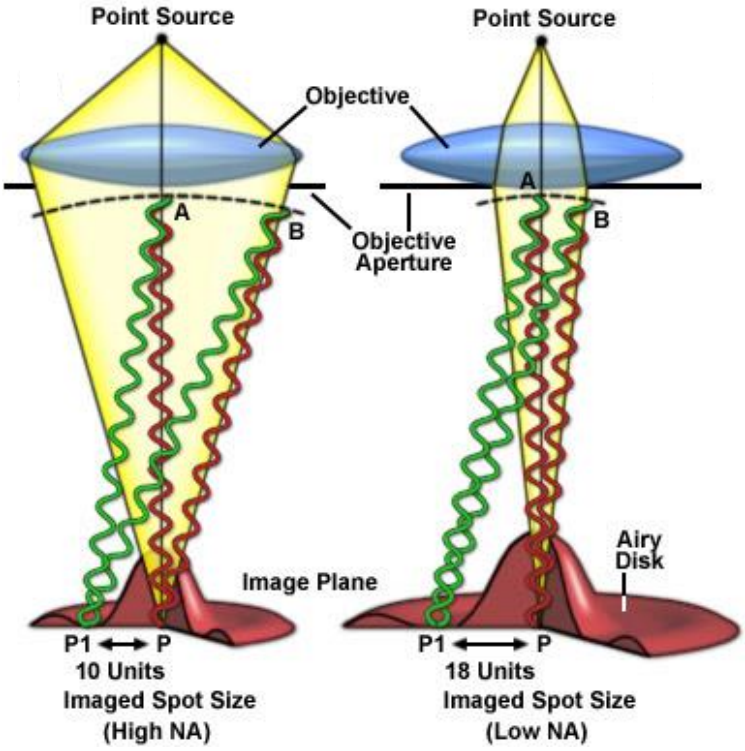

Fig. 1. Resolution limit imposed by wave nature of light. Image is reproduced with permission from MicroscopyU - The Source for Microscopy Education.

2.2 Super resolution fluorescence microscopy

For over a century, the diffraction-limited phenomenon restricted the performance of optical microscopy. In the early 1990s, this fundamental and unbreakable rule was circumvented thanks to the properties of specific fluorescent markers and their capacity to switch between different states. Indeed, several new exciting approaches in imaging have emerged that can 'break' this law under certain circumstances. STimulated Emission Depletion (STED) microscopy became the first method able to break the diffraction barrier, generating a new scientific field called super resolution fluorescence microscopy or nanoscopy. All far-field fluorescence nanoscopy methods use fluorescent molecules at subdiffraction length scales by arranging them

in two distinguishable states. Indeed, the transition between two molecular states of a fluorophore or fluorescent protein are modulated spatially and/or temporally. STORM and STED, which are the most representative techniques of SMLM and RESOLFT family respectively, are able to force a subset of fluorophores to be non-fluorescent, while another subsets to be capable of fluorescence. This common strategy for controlling the fluorescence emission are critical to achieve super resolved images of biological samples (Fig. 2).

In the case of wide-field microscopy, the resulting image is a combination of the overlapping blur caused by the diffraction-limited image of each fluorescent molecule, because all the fluorophores are imaged at the same time. To overcome the diffraction limit, in STORM and in general in all of the SMLM techniques, the fluorophores are imaged in a single-fluorophore regime (i.e. one molecule at a time). Indeed, for the assignment of the fluorophores to non-fluorescent and fluorescent states, STORM uses a random approach, where the localization of each fluorophore is obtained by calculating with high precision the centroid of the fluorescent signal. This process required that the fluorophores could be switched between fluorescent and non-fluorescent state for each frame, generating a subset of localizations. With this method, a resolution of below 40 nm has been measured.

Differently to STORM, STED uses a targeted approach where designated fluorophores are directly assigned to their appropriate states in the specific areas of the sample. STED is based on a confocal microscope, where the size of the excitation spot is restricted by inhibiting the fluorescence in the outer regions. This translates in a reduction of the PSF of the optical system to a size below the diffraction limit of light. The inhibition of the fluorescent signal at the periphery of the imaging spot is achieved by combining of two different beams: the excitation and the depletion beam. As result of this process, the depletion photons tend to relax the excited electrons of the fluorescent molecules, emitting a photon that replicates both the phase and wavelength of the depletion photons. Obviously, a spectral filter can be used to reject photons at that wavelength.

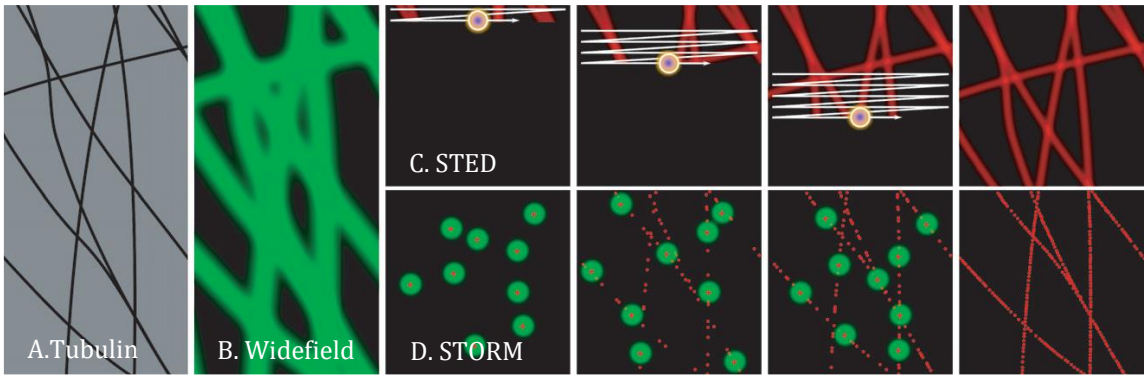

Fig. 2. Schematic illustration of the different acquisition strategies in STORM and STED. (A) Example of labelled tubulin filaments, which has features that are smaller than the optical diffraction limit. (B) Example of images acquired using a conventional fluorescence microscopy, where the fluorophores are illuminated at the same time, obtaining a diffraction limited image. (C) STED nanoscopy uses two different sources to achieve super resolved images. The first source (in blue) turns on all fluorophores while the second source (in orange) turns off the fluorophores in a region surrounding a small point. In this way, only the fluorescence in the blue area is detected. (D) Finally, In STORM, the combination of imaging buffers and appropriate light source maintain all the fluorophores in an off-state. A second light source permits to turn on randomly a small subset of fluorophores, and imaged briefly before they return to the off-state (D) (*12*).

An important feature of STORM is the possibility that same fluorophores may become fluorescent more than once for quantitative imagining at the single molecule. Also, the efficiency of fluorophore cycling, that is the number of times that a fluorophore is excited compared to the number of times that it is imaged, is better for STORM than for STED.

Instead, the simplicity of controlling fluorophores makes STED a more versatile option among all the super resolution methods.

Finally, STED microscopy allows the direct acquisition of super-resolved images and it does not require any further computational post-processing analysis.

2.3 Other super resolution methods

In the last 50 years, super resolution techniques have become an essential tool to investigate at the molecular level important biological and biophysical processes. In addition, the development of these new technologies has allowed to understand in more details the temporal evolution of living system, in correlation with the

biochemical and sequencing approach. Unfortunately, these new methods are prohibitively expensive, and hence are not available in many biological laboratories. In 2015, Boyden's group developed a new method called Expansion Microscopy (ExM), which allows obtaining super resolved image using a conventional diffracted microscope (*6*) (Fig. 3). The improvement in the resolution resides on the biological preparation rather than the optical characteristics of the microscope. The key point resides on the possibility of physically expand the sample, increasing the relative distances among biomolecules labelled with fluorescent dyes. We can image this process as polymer chains, which uniformly wrap the biomolecules in the biological sample, pulling them apart from each other. In this mode, every biomolecule in and between the cells will be moved apart from its neighbors in isotropic way. We can think to draw on a balloon and after blowing up: the ink particles will separate apart from each other, maintaining their relative organization.

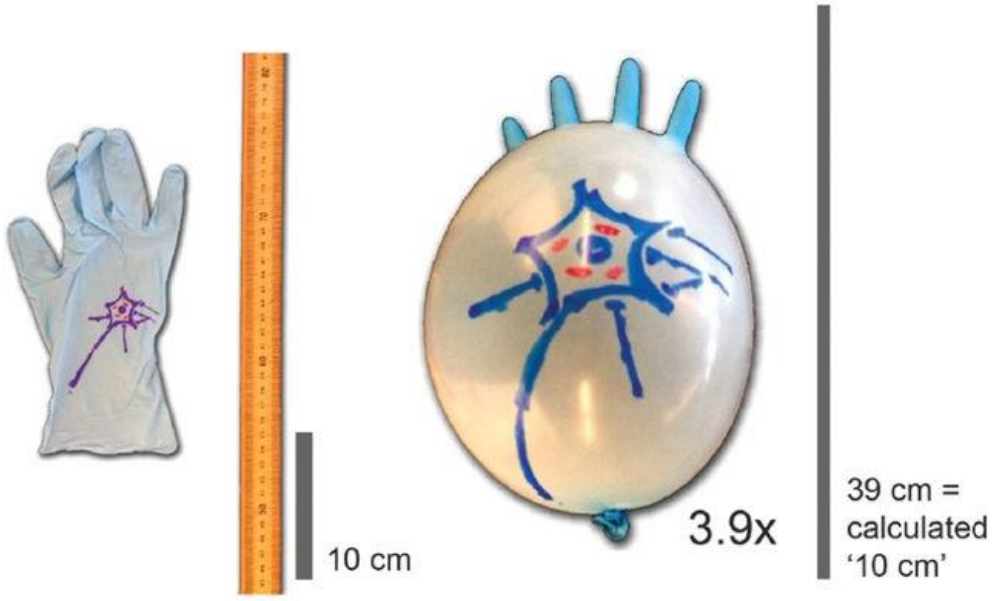

Fig. 3. Similar to the expansion of a balloon that reveals details of a drawing on its surface, Expansion microscopy expands tissue embedded in a hydrogel (*13*).

Contrary to other protocols for tissues preparation, like CLARITY (*14*) and CUBIC (*15*) methods, in which the expansion phenomena is a side effect and it requires to be minimized. In ExM, the expansion is deliberately performed to increase the distance between biomolecules, with an accuracy down the nanoscale, achieving a lateral resolution about 65 nm.

3 Super resolution methods

During my Ph.D., I had the chance to try different super resolution methods. In particular, my attention was focused on STED nanoscopy and ExM, and how to combine them to improve the final resolution. In the next chapters, I will describe in more details how STED and ExM work separately, the different protocols and the advantages and disadvantages of these methods.

3.1 STED Nanoscopy

STimulated Emission Depletion (STED) microscopy is a super resolution technique, which allows to bypass the diffraction limit and to shift the optical resolution down to macromolecular or even molecular levels (*2, 16, 17*). Similar to CLSM, STED microscope assembles an image by scanning pixel by pixel with a laser and it removes the out-of-focus light using a pinhole in the optical path. The improvement in lateral resolution relies on the conjunct illumination of the sample with a second long-wavelength laser able to selectively "silence" a population of the excited fluorophores. In order to use this concept, the PSF of the depletion beam must have zero fields in the center and non-zero at the periphery. By positioning an optical component in the path of the depletion laser, termed vortex phase plate, a doughnut-shaped beam is generated. In this mode, by increasing the STED power, the stimulated emission process saturates only the toroid area of the excitation volume. Therefore, the spontaneous fluorescence emission will occur only in the center of the excited volume, with a final resolution described by the following relationship:

$$\Delta d_{x,y} = \frac{\lambda}{2(n \sin \alpha)\sqrt{\frac{I}{I_s}}}$$

Where I is the maximum intensity of the STED beam, and the saturation intensity I_S is the intensity required for the STED beam to quench the spontaneous fluorescence emission by half.

In general, to enhance the final resolution, there are several issues to consider. As seen previously, the maximum of the excitation beam has to coincide with the zero-intensity point of the depletion beam. For this reason, it is important to accurately co-align the excitation and depletion beam. Another important factor that limit the

resolution is the temporal condition. In order to maximize the STED effect, the depletion beam should arrive at the sample when the electron of the fluorescent molecule is in the excited state. To synchronize these events, the onset of the depletion beam should be after a few picoseconds from the offset of the excitation beam, inducing the decay of the excited electron from S_1^{vib} to S_1.

Finally, the STED beam should not excite the fluorophores. In order to minimize the excitation and maximize the stimulated emission process, it is necessary to match the red–shifted wavelength of the STED beam with the tail of the emission spectrum of the fluorescent dye.

3.2 Correlative light and electron microscopy (CLEM)

Following the same physical rule for the diffraction limit of light, but with 10^5 times smaller wavelength, electron microscopy (EM) is characterized by a higher resolving power than light microscopy. EM and FM provide complementary biological information (*18*). Indeed, FM supplies protein specific details that are harder to obtain using with EM, but in a "dark space", where the context of the localization is lost. Instead, EM is able to get structural information of the entire biological sample, but it lacks of the specificity and compatibility with living sample. (*19*). For these reasons, the combination between EM with FM allows achieving a specific protein localization in the context of a global structure.

Fluorescence and electron microscopy can be used in two different ways. A vary common and useful approach is to investigate the biological sample by FM, for instance time-lapse studies of FP-tagged proteins - followed by fixation and further EM processing, acquisition and analysis. Otherwise, ultrathin sections prepared are imaged with both FM and EM (Fig. 4), using an immunolabeling method (*20*). In the last case, the antibodies require fixation and permeabilization of cells, that can change and damage the ultrastructural level of the sample. For this reason, genetic tagging is not an invasive method, because compatible with live cell imaging and strong fixation, and allows ultrastructural preservation (*21, 22*).

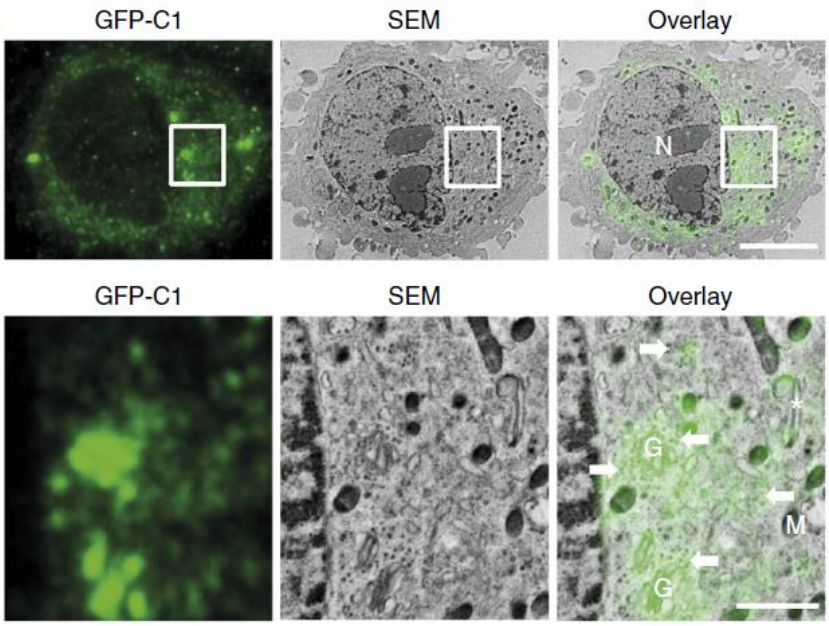

Fig. 4. The image shows an example of CLEM. Resin-embedded HeLa cells expressing GFP-C1, a diacylglycerol sensor, are prepared with high-pressure freezing followed by freeze substitution (*23*). Fluorescence from a 200-nm section (left), the matching back-scattered electron image (center) and the overlay (right) are shown.

Obviously, using nanoscopy method, we can match the resolution with EM, and, thus, to correlate the images obtained with a similar resolution scale.

Today, several examples of Correlative super-resolution optical and electron microscopy (CSREM) are reported. CSREM was first demonstrated as a combination of PALM and transmission electron microscopy (TEM) performed consecutively on Tokuyasu cryosections (*24, 25*). After, PALM and SEM as well as STED and SEM were demonstrated in plastic-embedded sections (*26*). iPALM and Pt replica TEM (*27*) as well as dSTORM and SEM (*28*) were combined for studies of membrane-bound structures. Finally, new OsO_4—resistant version of fluorescent protein mEos allowed for CSREM in plasticized sections of cells fixed with OsO_4 a high ultrastructure preservation (*29*) (Fig. 5).

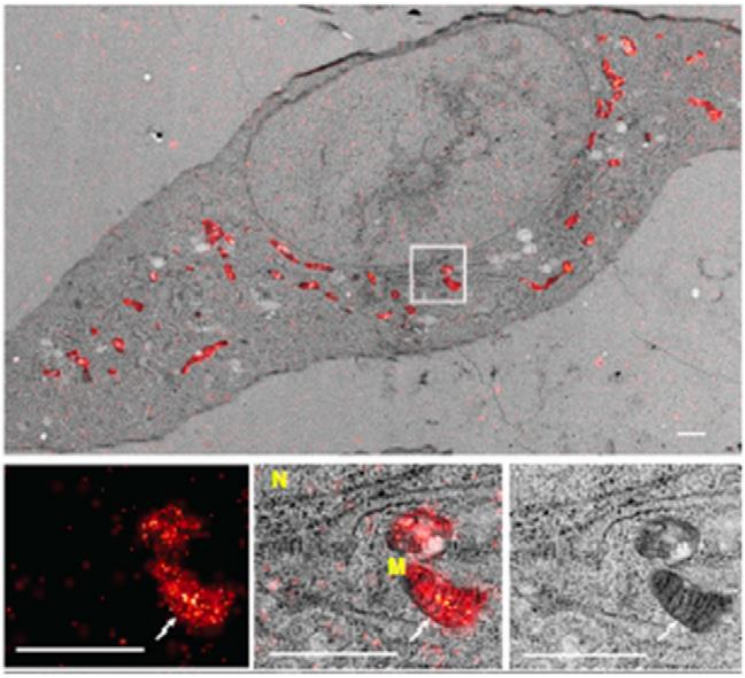

Fig. 5. Correlative PALM and TEM images of GMA section of 3T3 cells expressing mitochondrially targeted mEos4a (*29*). Labels indicate nucleus (N) and mitochondrion (M). Scale bars, 1 μm.

3.3 Expansion Microscopy (ExM)

Ed Boyden's group developed the first version of ExM in 2015 (*6*). Differently from the other techniques described previously, this new super resolution method allows to obtain super resolved imaging by physically expanding biological sample. This technique consists in soaking the cells with a polymer containing monomers (sodium acrylate and acrylamide), crosslinker (e.g. N-N'-methylenebisacrylamide), initiator (ammonium persulfate, APS) and accelerator (N, N,N', N'-tetramethylethylenediamine, TEMED) (*6, 30*). The polymerization process is a standard free radical reaction, initiated by the generation of free radicals by an initiator. The addition of the accelerator (TEMED) and the polymerization inhibitor (4-hydroxy-TEMPO, 4-HT) allow to diffuse the monomers throughout the sample before the polymerization reaction take off. Applying commercially available small molecules like 6-((acryloyl)amino)hexanoic acid (AcX) or methacrylic acid N-hydroxysuccinimidyl ester (MA-NHS) (*30, 31*), the key molecules or labels are functionalized with chemical handles, which allow them to be covalently anchored to the polymer (Fig. 6).

Next, the biological sample soaked in a swellable gel is mechanically homogenized (Fig. 6). It can be realized by treatment with proteases (e.g. proteinase K) or by high temperature and detergents (*6, 30, 31*). This step is essential to maintain the mechanical properties of the hydrogel and allows an isotropic expansion.

Finally, the sample is soaked in deionized water (Fig. 6). Thanks to the presence of sodium acrylate in the hydrogel and subsequent washed away the positively charged sodium ions with water, the negative charged carboxyl groups on the polymer backbone cause repulsion and, then, expansion of the gel. The swelling of the polymer leads to a fourfold isotropic stretching of the sample. The hydrogel is designed to be extremely dense, polyelectrolyte for high swelling force and with numerous cross-linked sites. In this mode, the relative organization of biomolecules and the nanoscale information are preserved after expansion (*6*). To understand better how ExM works, we consider two biomolecules that were 100 nm apart before the expansion. In this case, a diffracted limited microscope like scanning confocal microscope, with a resolution of 250 nm, cannot resolve them. However, it possible to resolve them using the same microscope after 4.5 times expansion, increasing the distance of the two objects of ~400 nm.

The optical free-aberration and the high resolution are the principle advantages of this technique, which make it very useful for tissue imaging. Unfortunately, it is not clear the robustness at the nanoscale level, as such process like gelation and digestion can alter the position and introduce artefacts in the distribution and organization of proteins in the cells.

In this chapter, I will discuss in more detail the different protocols, the applications and the pros and cons of this innovative method.

Fig. 6. Schematic representation of the steps involved in ExM (*32*).

3.3.1 Protocols

In the last years, to answer to biological problems, many versions of ExM techniques have been developed. These six techniques (including the first one) use different approaches and methods, but they are characterized by a common idea: physically

expanding biological samples to increase the final resolution. It is possible to divide these methods in two groups, depending on the labelling strategy used. Indeed, expansion microscopy (ExM) (*6*), ExM with conventional antibodies (*30*), and iterative expansion microscopy (iExM)(*33*) use specific probes before the hydrogel synthesis. Instead, magnified analysis of the proteome (MAP) (*34*), expansion fluorescence in-situ hybridization (ExFISH) (*35*) and protein-retention ExM (ProExM) (*31*) first synthetized a swallable gel and, after expansion in MilliQ water, the probes are introduced in the samples.

In the original protocol, a specific protein is labelled with the primary antibody and, successively, with a DNA-conjugated secondary antibody. After antibody staining, a complementary DNA characterized by a tri-functional labelling (a gel-anchoring group, a chemical fluorophore and the oligonucleotide that can hybridize to the complementary sequence of the tag) is added to the sample to visualize it after expansion. In this mode, during the gelation, the complementary DNA is incorporated to the polymer backbones through the gel-anchoring labelling (*6*). The resistance of the oligonucleotides to the proteinase digestion is the principle benefit of this first version. On the other hand, the conjugation of DNA with a secondary antibody is expensive and time-consuming labelling strategy. For these reasons, two new versions of this technique were proposed (*30, 31*). In these cases, the oligonucleotide functionalized with gel-anchoring group was substitute with commercially available chemicals (Fig. 7). The proteins in the sample are labelled with conventional antibodies (primary and secondary antibody) and successively treated with methacrylic acid N-hydroxysuccinimidyl ester (MA-NHS), glutaraldehyde (GA) (*30*) or 6-((acryloyl)amino)hexanoic acid (AcX) (*31*), necessary for the linking of the peptides or proteins to the hydrogels. After, the samples are digested and expanded in deionized water. In addition, these two studies demonstrate that fluorescent proteins (GFP) preserve their fluorescence even after the proteinase treatment, using opportunely digestion time (Fig. 7). In this mode, it is possible to visualize fluorescent fusion proteins without the need for a long antibody incubation.

Indeed, a drawback of these methods is the diminution of the fluorescence signal at the final expansion. To overcome these limitations, the post-expansion labelling variants were created (Fig. 7). For example, proExM (*31*) demonstrates that all

proteins of a biological sample can anchored to the hydrogel via AcX and then expanded after a denaturation step, and not digested. For this reason, it is possible to stain the gel-anchored denatured proteins with conventional antibodies after expansion.

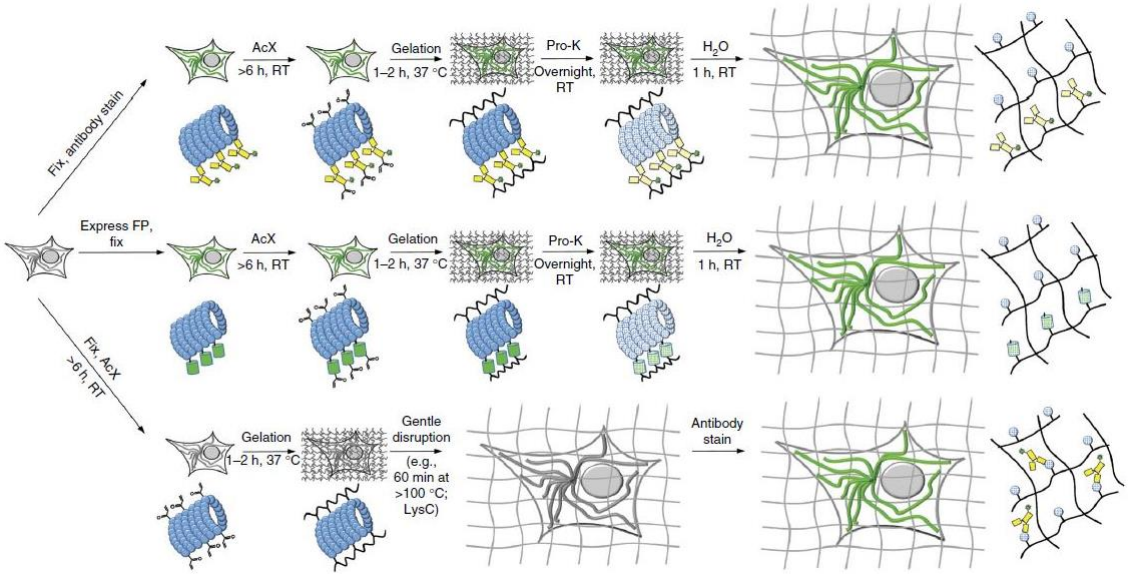

Fig. 7. The principal methods of ExM with protein retention. Samples are chemically fixed and stained with conventional antibodies, before AcX treatment and subsequent expansion (top). In the middle, the samples expressing FPs are fixed before AcX treatment. Finally, the samples treated with AcX, followed by gelation, are then homogenizate (for example, alkaline hydrolysis and denaturation, or digestion with LysC), and finally are labelled with an antibody staining in the expanded state (bottom) (*31*).

In 2016, Ku et al published a paper demonstrating a new expansion method called magnified analysis of the proteome (MAP) (*34*), for super resolution imaging of intact tissue organization. They notice that the protease digestion step in ExM causes a loss of proteins and limits the number of proteins that can be detected in the same sample. For this reason, this protocol uses the possibility to anchor all the proteins to the hydrogel, and after denaturation and expansion of the specimen, the antibody staining is applied. On the other hand, the antibodies are diffuse into expanded hydrogel in which all proteins are cross-linked and denatured. This strategy allows to remove antibodies from the hydrogel and labelling other proteins again, imaging them with different colors. A drawback of this technique is the loss of some epitopes during the denaturation step, but this protocol works with 80% of antibodies attempted.

Expansion fluorescence in situ hybridization (ExFISH) (*35*) is another version of ExM in which RNAs are covalently anchored to the gel with the molecule LabelX (Fig. 8). Therefore, RNAs are labelled with FISH probes after expansion for imaging. An advantage of this method is the possibility to apply the protein anchoring reagent (AcX), to retain proteins/RNAs to the hydrogel and imaged them simultaneously.

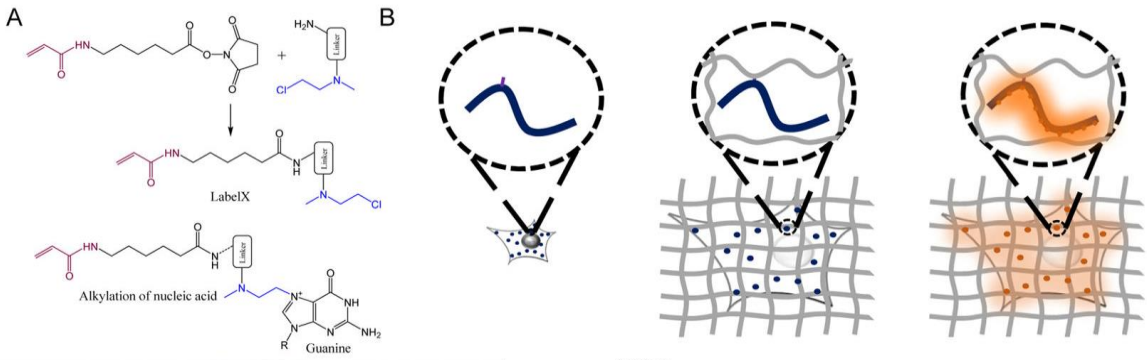

Fig. 8. (A) Acryloyl-X SE (top left) is reacted to Label-IT amine (top right) via NHS-ester chemistry to form LabelX (middle), which serves to make RNA gel-anchorable by alkylating its bases (bottom). (B) In ExFISH experiment, the biological specimens are treated with LabelX (left), which enables RNA to be anchored to the ExM gel.

The original expansion and its variants generate an expansion of 4.5x linear expansion, while the expansion factor of ExFISH is 3-4.5x (due to the buffers used), resulting in 60-70 nm resolution obtainable using a diffracted-limited microscope. In 2017, Ed Boyden's group developed a technique called iExM (*33*), which allows expanding biological samples more than 20-fold (Fig. 9). To achieve this goal, it is necessary a twice expansion process, which allows an effective resolution of 25 nm using a confocal microscope.

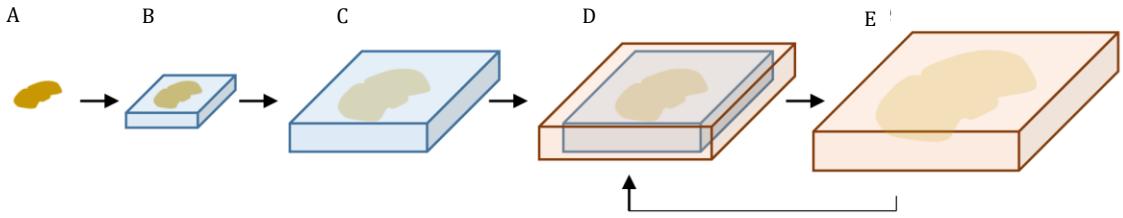

Fig. 9. Schematic representation of iExM, which shows how a biological sample can be expanded multiple times. First, a swellable polyelectrolyte gel network is formed throughout the sample (A), then mechanically homogenized and expanded (B, C). After expansion, a second swellable polyelectrolyte gel network is formed throughout the first hydrogel (D), and then expanded after dissolving the first gel (E). This process (D, E) can be applied repeatedly to increase the physical magnification still further, if desired (*33*).

In summary, different ExM protocols are developed in these last years, to resolve different biological questions and for different kinds of specimens. Our attention is focused on Chozinsky method (*30*), where, as seen previously, is performed by staining with primary and secondary antibody before expansion.

3.3.2 Distortion analysis

It is possible to quantify the isotropy and, therefore, the distortion due to the gelation and expansion process. A common method is to image a pre-expansion sample with a diffracted limited or super-resolved microscope (for example, SIM or STORM), and then take a post-expansion images using a conventional microscope (confocal microscope). By performing a non-rigid registration of the two images, aligning as much as possible through the rigid transformations, we can calculate the amount of distortion (Fig. 10). For each ExM variant was showed a distortion in length of 1–4% across length scales of tens to hundreds of microns (*6, 30, 34*).

To calculate the expansion factor and the resolution obtainable, one way is to measure the gel size before and after expansion, but this method is not accurate. Instead, by deconvolving of the microtubule diameter after expansion and comparing the real size obtained by electron microscopy, it is possible to acquire the effective resolution of ~60–70 nm for ~4.5× of expansion (*6*).

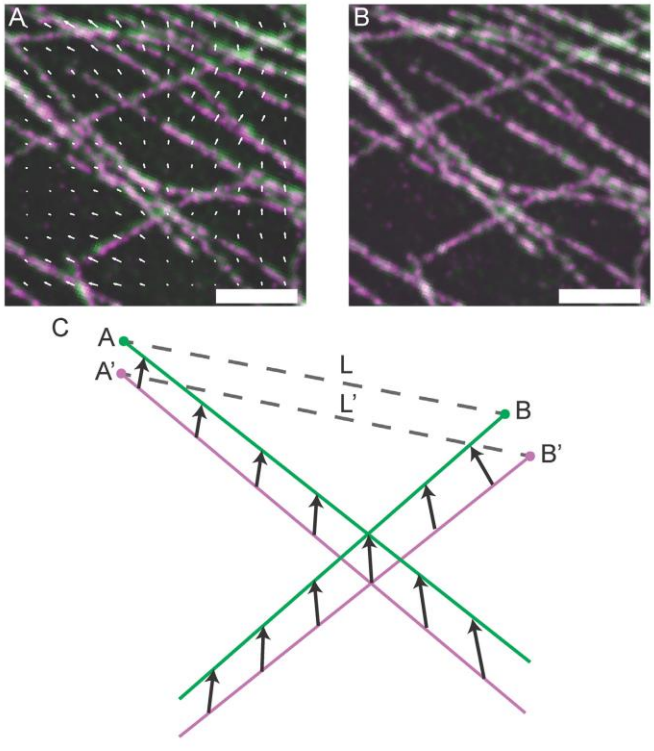

Fig. 10. By deforming the post-Ex image via non-rigid registration to match to the pre-Ex image, it is possible to calculate the error of ExM. In this example, the pre-ex image is acquired by using super resolution technique (Sim), while the post-ex image using a confocal microscope (*6*).

In addition, the homogenization of the sample plays an important role in the correct expansion. In fact, if this step is not correctly performed, the specimens resists to the expansion, causing fracturing of cells and tissues (*30*) (Fig. 11).

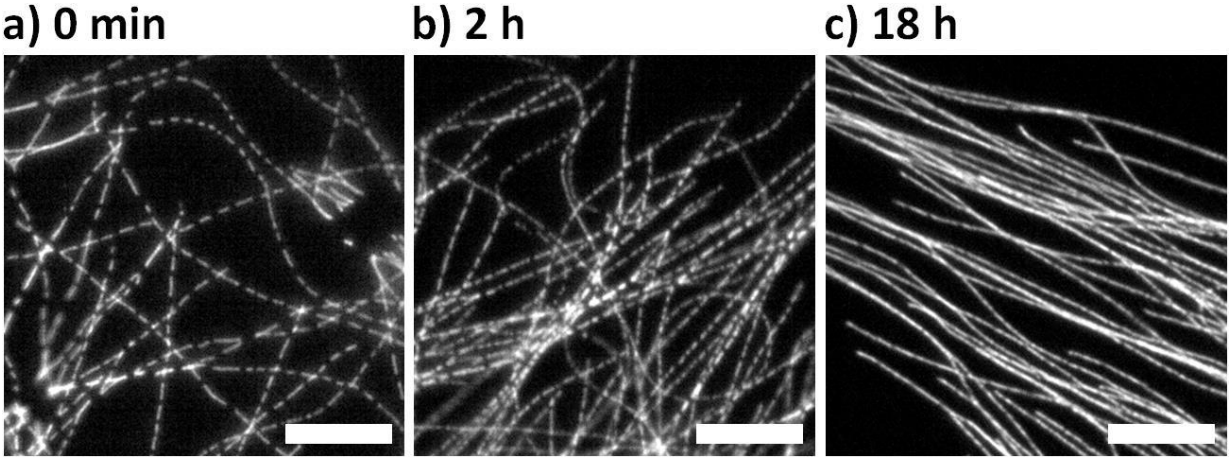

Fig.11. Epifluorescence images of expanded BS-C-1 cells stained for tyrosinated tubulin, treated with MA-NHS, and digested at different period (*30*). Low incubation time of the proteinase K causes discontinuity in the microtubule architecture at the final expansion.

3.3.3 Applications

The main purpose of ExM is related to the neurobiological applications. Therefore, Boyden et al demonstrated that ExM could be used to imaged synaptic contact between neurons in mouse hippocampus. Successively, this technique was used to image other brain regions, synapses and synaptic proteins (e.g. excitatory and inhibitory neurotransmitter receptors, presynaptic scaffolding proteins, postsynaptic scaffolding proteins, etc.) (*6, 31*). In addition, it was applied to expand culture mammalian cells (*2, 6, 30, 35, 36*), *Escherichia Coli* bacteria (*37*), lung, pancreas, spleen, and nonhuman primate brain (*31*), with many other species (including Drosophila, zebrafish, and human) and tissue types (including skin, kidney, colon, liver, and others). In 2017, the possibility to use ExM was demonstrated for medical uses, in particular for disease diagnosis. This technique, called ExPath, was used for optical diagnosis of kidney minimal-change disease, which previously required electron microscopy (EM) analysis (*38*).

3.3.4 Advantages and disadvantages

In addition to provide a nanoscale resolution using a diffracted limited microscope, ExM enables other advantages. Considering at the maximum expansion, the sample is 99% water, resulting completely transparent and optical aberration free. A second important benefit is the decrowding of protein complexes, generating room around biomolecules due to the expansion of the sample (*31*). In general, for an immunofluorescence protocol, it is difficult to label densely packed proteins, because the antibodies are larger than the proteins to label. For these reasons, the image can be in poor staining and not sufficient bright for super resolution imaging. By generating molecular decrowding, more space around the biomolecules is generated, revealing epitopes previously cancelled in the protein complexes.

Finally, ExM is a good method to investigate biological problems using 3-4 colors and it is the cheapest technique respect to the other super resolution methods.

However, this technique is not compatible with live cell imaging and requires a long preparation (many several stages, i.e., immunostaining, gelation, digestion, and expansion) and protocol optimization for each protein to investigate (Tab. 1).

	Confocal	STED	SIM	PALM/STORM	ExM
Resolution	~ 250 nm	≥ 50 nm	≥ 110 nm	~ 30 nm	~ 65 nm
Good for thick samples?	thick ok	thin-moderate possible	thin-moderate possible	no, typically thin (<1µm)	thick ok
Multicolour	3-4 channels	> 2 channels difficult	3-4 channels	difficult	3-4 channels
Hardware cost	200000 €	800000 €	500000 €	800000 €	use existing hardware
Live imaging?	yes	difficult	yes	difficult	no, fixed only

Table 1. The table reassume the main advantages and disadvantages of ExM compared to the other super resolution methods.

3.4 Labelling protocols for super resolution techniques

In the last years, with the development of the super resolution techniques, all biological sample preparations need a particular attention imposed by the capacity to overcome the diffraction limit of light. This aspect is neglect for conventional imaging techniques, but become extremely relevant for super-resolution methods and ExM. Therefore, inadequate sample preparation may not be noticed with conventional microscopy, but is clearly visible with super resolution microscopy. Instead, the field of EM, due to the high resolution obtainable, refined the techniques for the preparation of biological samples. In the last years, the field of fluorescent super-resolution microscopy is encountering similar problems, and some technical solutions were borrowed from EM (*39*).

First, the use of immersion lenses with high numerical aperture is compromised by spherical aberrations, due to the refractive index mismatch between the immersion and embedding medium. Moreover, the right mounting media has the capacity to reduce the optical aberrations and the photo-bleaching. For example, the principal embedding medium extensively used in STED microscopy are Mowiol and TDE (*40*). Subsequently, the other critical steps involved in the sample preparation for super resolved fluorescent microscopy are fixation, permeabilization (*39*) and right dyes selection.

Fixation of cells or tissues is a crucial step involved in an immunofluorescence protocol, and it is necessary for the immobilization of proteins and structural preservation. To do this, it is possible to use paraformaldehyde (PFA) or glutaraldehyde (GA) to cross-link neighboring peptides or proteins. PFA is a small molecule characterized by only one aldehyde group that reacts with free amino groups (NH_2) in the protein N-terminus and side chain of lysins (*41, 42*). Instead GA, thanks to its two aldehyde groups, is a strong cross-linker but permeate the biological membrane slowly (*43*). For these reasons, GA is used for the preparation of EM samples because allows a better structural preservation (*44*). However, the field of conventional fluorescence microscopy prefers PFA than GA, because is faster and do not compromise proteins epitope for the immunodetection. Moreover, conventional PFA-based protocols used in fluorescence microscopy are not sufficient to immobilize cellular structures (*45*) and can invalidate the staining

quality and generate artifact (Fig. 12) (*46*). For these reasons, to stabilize biological samples and to image them with super resolution techniques, it is extremely important to investigate several combinations at different ratio of these fixatives (*20, 47*).

Permeabilization is subsequent process to fixation, which generates "openings" in biological membranes by extracting lipids. The aim is to guarantee access to affinity probes to the interior of a cell. This process is performed using mild detergents, such as Tween 20, Triton X-100, digitonin and saponin (*48*). It is important to notice that permeabilization not only extracts lipids, but also transmembrane proteins. For this step, it is crucial to optimize the amount, the incubation, the temperature and the choice of detergent, to detect accurately intracellular epitopes. If fixation step is not complete, the loss of cytosolic elements can occur, generating low staining quality and signal to noise ratio for super resolution techniques.

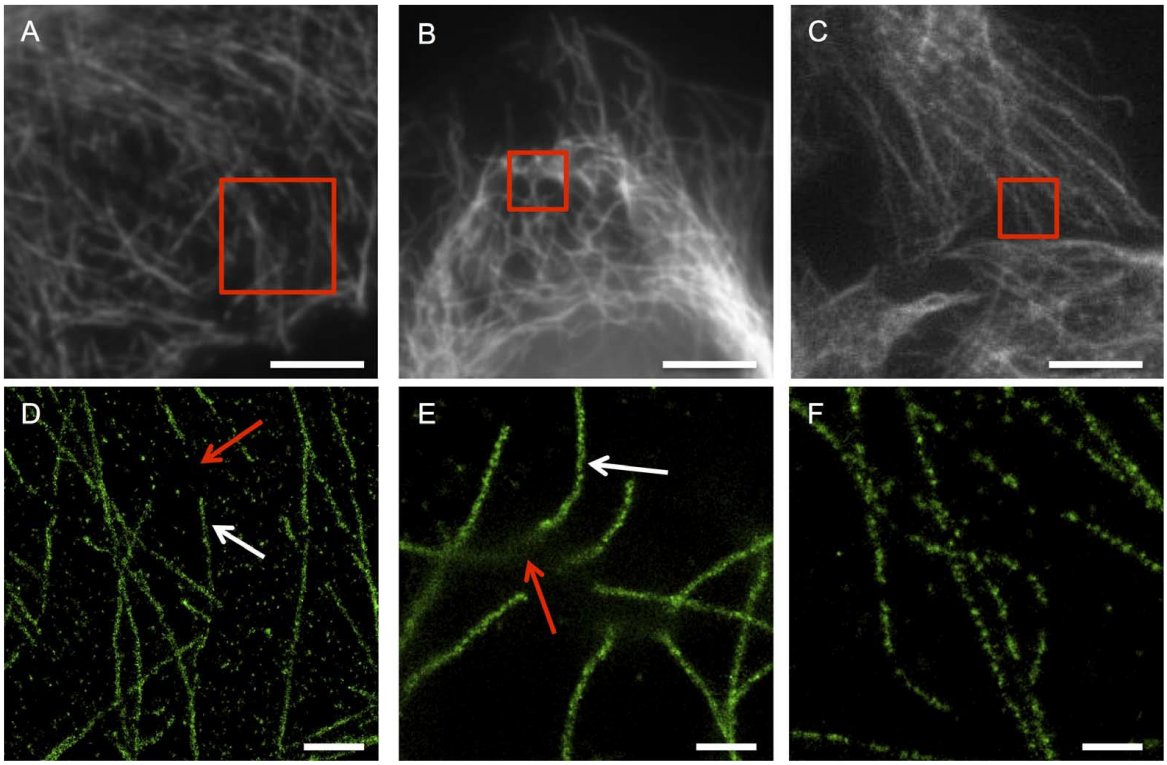

Fig. 12. (A-C) show the epifluorescence images of COS-7 cells labelled for tubulin with Alexa Fluor 647. The PFA fixation is applied with a shorter period than optimal (A), at lower concentration than optimal (B) and for longer period than optimal (C). These images do not show fixation artifacts. (D–F) corresponding SMLM images of sub-areas from A–C show sub-diffraction scale damage and discontinuity in the microtubule architecture (*46*).

3.5 Affinity probes in super-resolution microscopy

The high specificity and the large selection make the antibodies the most widely tool used in fluorescence microscopy. The capability to carry on several fluorophores permit to adapt them to different biological problems. The principle advantage is the capacity to obtain a bright and specific staining, essential in optical microscopy and in particular for super resolution methods. The most popular method used to increase the signal is to use the indirect immunofluorescence. The non-fluorescent primary antibody labels a specific protein, and successively a secondary antibody, which is conjugated with many fluorochromes, recognizes the primary antibodies. The first advantage respect to a direct immunostaining is that more than one secondary antibody can attach the primary antibody, increasing the signal from each protein detected. The second advantage is a more flexibility in the experimental design, because several secondary antibodies can be used with a wide range of commercial fluorophores for each primary antibody (*49*). However, the relative large dimensions (150 kDa, 15 nm) and the dual bind capability of these probes can introduce artefact and lack in the localization precision of the target proteins. For these reasons, the continuous improvement of super resolution techniques, have caused the development of smaller affinity probes with monovalent binding. One way to overcome these limitations is to use a protease (papain) to generate antibodies fragment (Fab, 50 kDa, 9 nm, (*50*)). Successively, Hamers-Casterman and colleagues discovered that camels naturally produce single chain antibodies (*51*) called nanobodies or VHHS (13 kDa, 3 nm), that can be cloned and produced in microorganisms easily. Nanobodies are able to detect accurately the protein target compared to the conventional immunostaining (Fig. 13; 14, A and B).

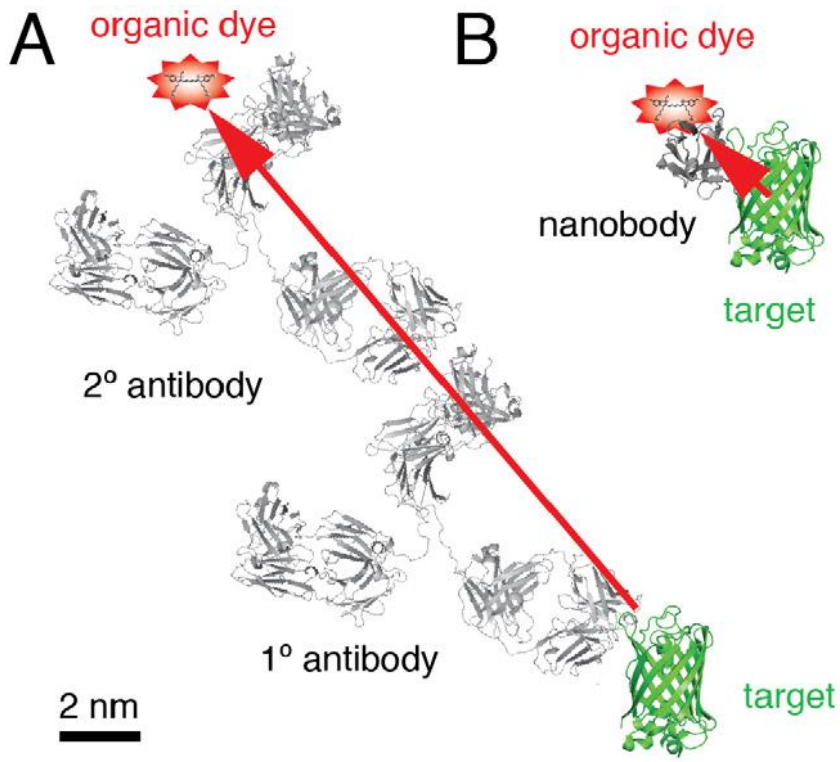

Fig. 13. Comparison between a conventional immunostaining and nanobodies technologies. For labelling a protein of interest (in this case GFP), the complex formed by a primary and secondary antibody coupled to an organic fluorophore generate an important error in the detection of the target protein (A). Instead, when a dye is coupled to a nanobody, it is delivered into closest proximity of the target structure (B). This strategy is extremely important in the field of the super resolution techniques (*18*).

At the same time, thorough a process called systematic evolution of ligands by exponential enrichment (SELEX) (*52*), it was possible to produce a new affinity probe based on short single stranded oligonucleotides (15 kDa, 4 nm) termed aptamers, very useful for super resolution technique like STED (Fig. 14, A and B). However, in these cases, the cells have to be fixed and permeabilized to ensure that these affinity probes reach the antigen. Therefore, live cell imaging is not compatible, which leads to a severe confinement of the possible applications of super resolution microscopy in biology. Recently, researchers have produced affinity red fluorescent probes based on silicon-rhodamine (e.g. SiR-actin, SiR-DNA), able to bind selectively cytoskeletal element and DNA, characterized by florigenic effect (they became ~10-fold brighter upon binding actin for example) and very low cytotoxicity (*53, 54*).

Name	Molecular weight	Linear size	Composition
IgGs	~150 kDa	~15 nm	Protein
Fabs	~50 kDa	~9 nm	Protein
scFvs	~30 kDa	~6 nm	Protein
VHHs (nanobodies)	~15 kDa	~3 nm	Protein
Affibodies	~6 kDa	~2 nm	Protein
DARPins	~10–30 kDa	~2–3 nm	Protein
Fibronectin III (FN3, Monobodies)	~10 kDa	~2 nm	Protein
Aptamers	~10–20 kDa	~2–3 nm	Single stranded DNA or RNA

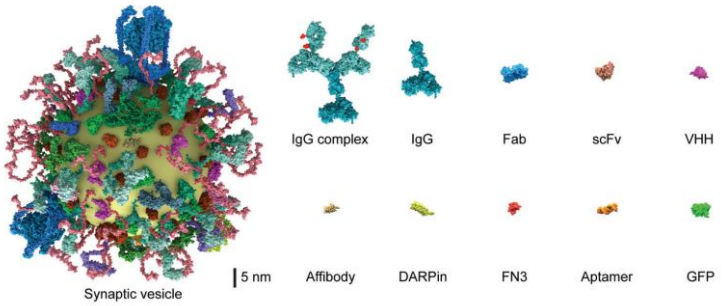

Fig. 14. (A) The table reassumes the main affinity probes and their corresponding linear size used in fluorescence microscopy. (B) Comparison between structure and size of different probes using the synaptic vesicle as a size reference (*39*).

Another approach for live cell imaging is based on the green fluorescent protein (GFP) from *Aequorea Victoria*. Discovered in the 1960s (*55*), cloned in the early 1990s (*56*) and expressed in model organisms (*57*), GFP and its mutants revolutionized cell biology. In combination with fluorescence microscopes, they have used to explore cellular events at high spatiotemporal resolution. GFP family allows monitoring dynamics and expression of a protein of interest (*58*). They are characterized by a barrel-shaped structure, where 11 beta-sheets generate a cylinder around the chromophore, which is autocatalytically formed via a cyclization of three amino acids. The formation of the chromophore required only the presence of oxygen (*56*). However, GFP-like proteins have some drawbacks: the large size of the β-barrel structure (4.2 nm x 2.4 nm x 2.4 nm, ~30 KDa), the low photostability and the limitations in absorbance and fluorescence to visible spectrum.

Recently, a new class of fluorescent proteins have been developed from bacterial phytochromes, which allow to extend the spectral characteristics of GFP family proteins (Fig. 15). These optical tools are used as templates for engineering far-red and infra-red FPs, because they use the low molecular weight Biliverdin (BV) as chromophore. BV is abundant in mammalian cells and it is characterized by red-shifted absorbance (approximately 650–900 nm) (*59*). In this spectrum, these markers for fluorescence microscopy show many advantages: scattering and autofluorescence are reduced, absorbance hemoglobin, melanin and water is minimal and red light is less phototoxic for biological samples (*59, 60*).

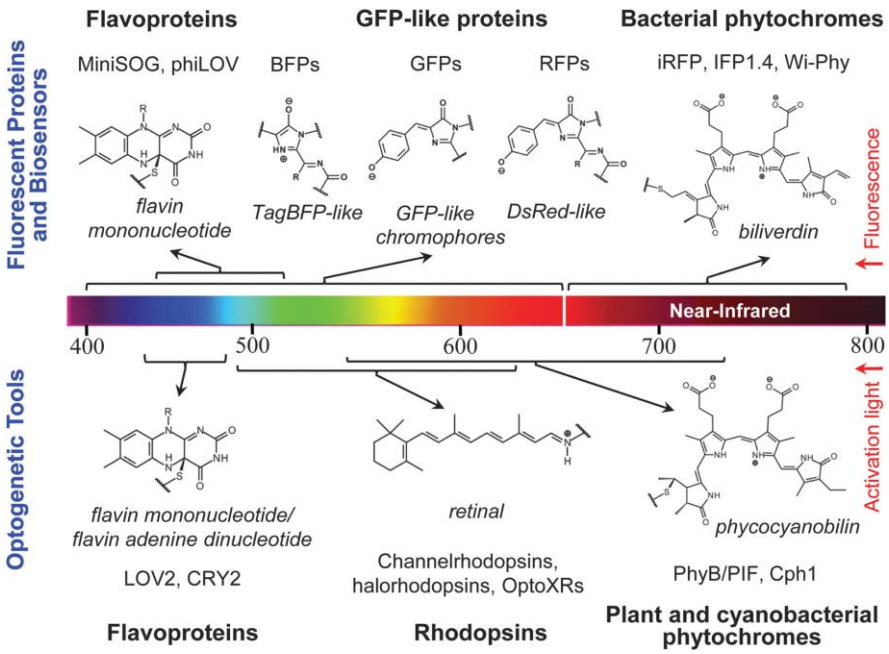

Fig. 15. The diversity of the chromophores in the principal groups of the available fluorescent proteins used as biosensors and optogenetic tools developed for biotechnological applications.

However, a common drawback of these encoding fluorescent probes is the low photo-stability for super resolution techniques. For this reason, functionalizing a specific protein with a chemically synthesized fluorophores, we achieve superior characteristic to the fluorescent proteins in terms of photo-stability and quantum yield. A popular method is based on the self-labeling SNAP-tag, where the protein of interest is expressed as a fusion with a modified form monomeric DNA repair enzyme (20 kDa), human O^6-alkylguanine-DNA-alkyltransferase (AGT), or SNAP-tag. The SNAP-tag can be specifically labeled with synthetic O^6-benzylguanine (BG)-conjugated substrates, resulting in a stable thioether bond between a reactive cysteine residue in the tag and the probe (*61, 62*) (Fig. 16). For fluorescence microscopy, BG derivatives have to functionalize with specific organic fluorophores. In this mode, a single construct can be used with different fluorophores substrates to label a protein of interest, with a high quantum yield and photo-stabile fluorescent dye. Another similar approach is a modified version of SNAP-tag, called CLIP-tag, engineered to react with benzylcytosine rather than benzylguanine derivatives (*63*). SNAP and CLIP proteins can be labeled simultaneously and specifically with different substrates, to investigate two bio-molecules at the same time in living cells using super resolved STED imaging (*64*).

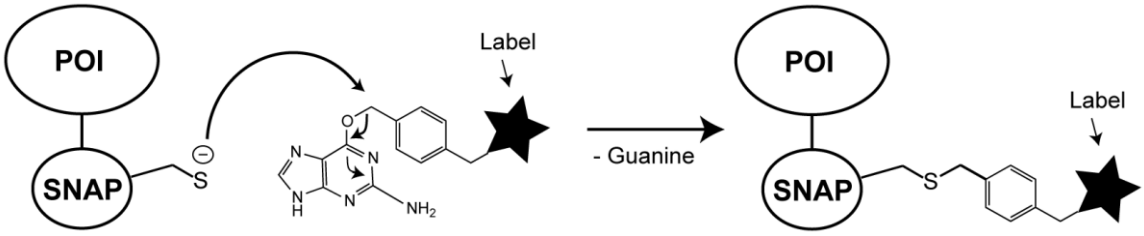

Fig. 16. Reaction involved in the formation of a covalent bond between SNAP-tag and O^6-benzylguanine (BG) derivatives. A protein of interest (POI) is fused to the SNAP-tag for expression in cells.

In general, the right fluorophores choice plays an important role in the sample preparation for super resolved images.

Indeed, for STED nanoscopy, the fluorescent dyes and proteins must be characterized by high photo-stability and photo-bleaching resistance (*65*). This is due to the high intense excitation and depletion beams used (Tab. 2).

Instead, for ExM, the fluorescent dye must have different characteristics, in particular for pre-expansion staining. The principle limitation on the selection of fluorophores is due to the bleaching during the polymerization process. Indeed, fluorophores such as Cy3, Cy5 and Alexa 647 (cyanine family) were completely degraded during the polymerization step. Instead, Alexa 488, Atto 565 and Atto 647N are compatible with this process, because retain more than 50% of their initial fluorescence (*6, 30*). Finally, using proExM method, any fluorescent dyes can work, because the antibodies are added after expansion and they do not go through the gelation process (*31*).

Fluorescent proteins used in super-resolution imaging

STED fluorophores	Notes	λ_{ex} (nm)	λ_{em} (nm)	λ_{STED} (nm)	ε (M^{-1} cm^{-1})	Φ	Resolution reported
EGFP	m	490	510	575	55000	0.6	~70 nm
EYFP	m	514	527	598	36500	0.63	<100 nm
Citrine	m	516	529	592	77000	0.76	<60 nm
E2Crimson	t	611	646	760	126000	0.23	<100 nm
TagRFP657	m	611	657	750	34000	0.1	~74 nm

Organic fluorophores used in super-resolution imaging

STED fluorophore	Notes	λ_{ex} (nm)	λ_{em} (nm)	λ_{STED} (nm)	ε (M^{-1} cm^{-1})	Φ	Resolution reported
Chromeo 488		488	517	592	73000	0.38	30 nm
Chromeo 494		494	628	760	55000	0.28	~80 nm
Atto 565		563	592	~662	120000	0.9	30–60 nm
Atto 647N		644	669	~765	150000	0.5	30–60 nm
Fl-Rhodamine		633	653	~762	75000	0.92	~40 nm
Si-Rhodamine		645	662	~775	100000	0.39	~50 nm
AbberiorSTAR635P		635	655	~775	75000	0.92	~20 nm

Tab. 2. List of the main fluorescent proteins and fluorophores used in STED nanoscopy (*65*).

4 A biophysical challenge

Despite all the technological improvements related to the sequencing of the human genome and other organism models, our capacity to decipher genome sequences are limited. It is a utopian dream to understand the expression and the silencing activity of thousands of genes, simply reading the basis of DNA sequences. Therefore, which are the changes in the nuclear architecture and DNA organization that permit to develop and maintain complex multicellular organism require to be investigate more deeply.

In the last years, in the chromatin research has played an important role the epigenetic modifications, corresponding to the phenotype changes that are not involved in the DNA sequences. For example, some specific mechanisms of gene regulation, such as DNA methylation and histone modification, can partially answer at this biophysical challenge (*66*).

Another region localized at the nuclear periphery, called nuclear envelope (NE), has been the subject of intense discussion about its possible role in almost everything that happens in the nucleus, from the nuclear architecture to the chromatin organization. In addition, recent studies have demonstrated that the alteration in the NE proteins can be associated to different diseases. In particular, a wide group of human disorders called laminopathies is caused by the mutations in *LMNA* gene, encoding for lamin A protein (LA). In the last years, research on the nuclear lamins and laminopathies has contributed to understand the function of the NE and the interaction with the chromatin DNA in normal and pathology conditions.

The principal aim of this work is to understand how LA and its mutant form (called progerin or ΔLA50) are organized in normal and pathological condition. The expression of ΔLA50 induces many cellular defects, as lobulated nuclei, loss of peripheral heterochromatin, accumulation of DNA damage, telomere aberration, clustering of nuclear pores, leading to premature cellular senescence (*67*). In addition, different forms of cancer are associated with these characteristics (Fig. 17).

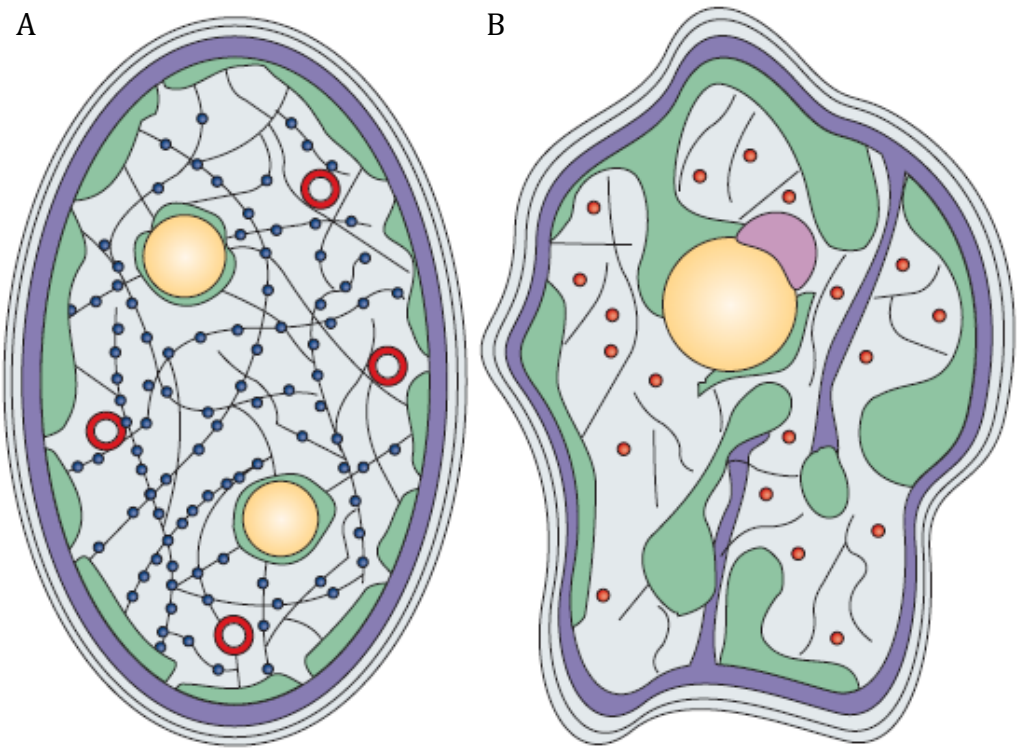

Fig. 17. Comparison between normal (A) and aged/cancer nuclear cell (B).

In the last years, several approaches have developed in the microscopy field. These extraordinary tools could help me to investigate the NE and its role in the chromatin-DNA organization. During my Ph.D., I optimized different staining protocol to image the NE. In particular, my attention was focused on CLEM (Correlate Light and Electron Microscopy) and super resolution microscopy techniques. Indeed, our laboratory developed a protocol that combines two super resolution methods: Stimulated Emission Depletion (STED) and Expansion Microscopy (ExM), termed ExSTED (*7*). As described previously, these methods use different ways to achieve super resolved images. STED employs the overlapping of two laser beams to obtain a smaller PSF shape to overcome the diffraction limit of light. Instead, ExM, expands physically the biological samples.

Thanks to the resolution achievable, ExSTED can help me to verify the isotropy and characterized accurately the expansion process. A drawback of ExM is the difficulty of precisely defining the expansion factor and the distortion of the sample embedded in the gel. To quantify the expansion factor of biological structures, the ratio between the hydrogel sizes might not a sensible and reliable method. In addition, process like gelation and digestion can alter the position and introduce artefacts in the distribution and organization of proteins in the cells. For these reasons, it is

extremely important to investigate the native conformation of proteins assembling after expansion. For the quantification of this process, our idea is to use a conserved, known structure as calibrator method not resolved using a conventional light microscopy, localized in the NE. Due to the size of 100 nm and the symmetric structure, Nuclear Pore Complex (NPC) is a good candidate for this analysis. This highly complex structure is characterized by eightfold rotational symmetry consisting of a cytoplasmic and nuclear ring connected by scaffold proteins built around a central channel. Each side of this channel is associated with eight filament subunits, where they form a highly ordered structure called “nuclear basket” inside the nucleus. Thanks to electron microscopy and super resolution techniques, a precise description of the NPC structure was obtained. In particular, our attention is focused on a specific subunit called Nup153 localized on the nucleoplasmatic side.

Before to investigate the nuclear lamins using ExM, it is extremely important to validate the isotropic expansion and the EF. The combination between ExSTED and NPC as biological reporter can help me to verify the isotropic expansion of the hydrogel (Fig. 18). My principal goal is to determine quantitative pre-expansion (Pre-Ex), post-digestion (Post-Dig) and Post-Expansion (Post-Ex) analysis, and accurately defined the nanoscale expansion and the distortion for biological structures. In addition, these gel properties were evaluated at the microscale and macroscale level, measuring the distance and its deformations between pore-pore and the gel size, respectively (Fig. 18).

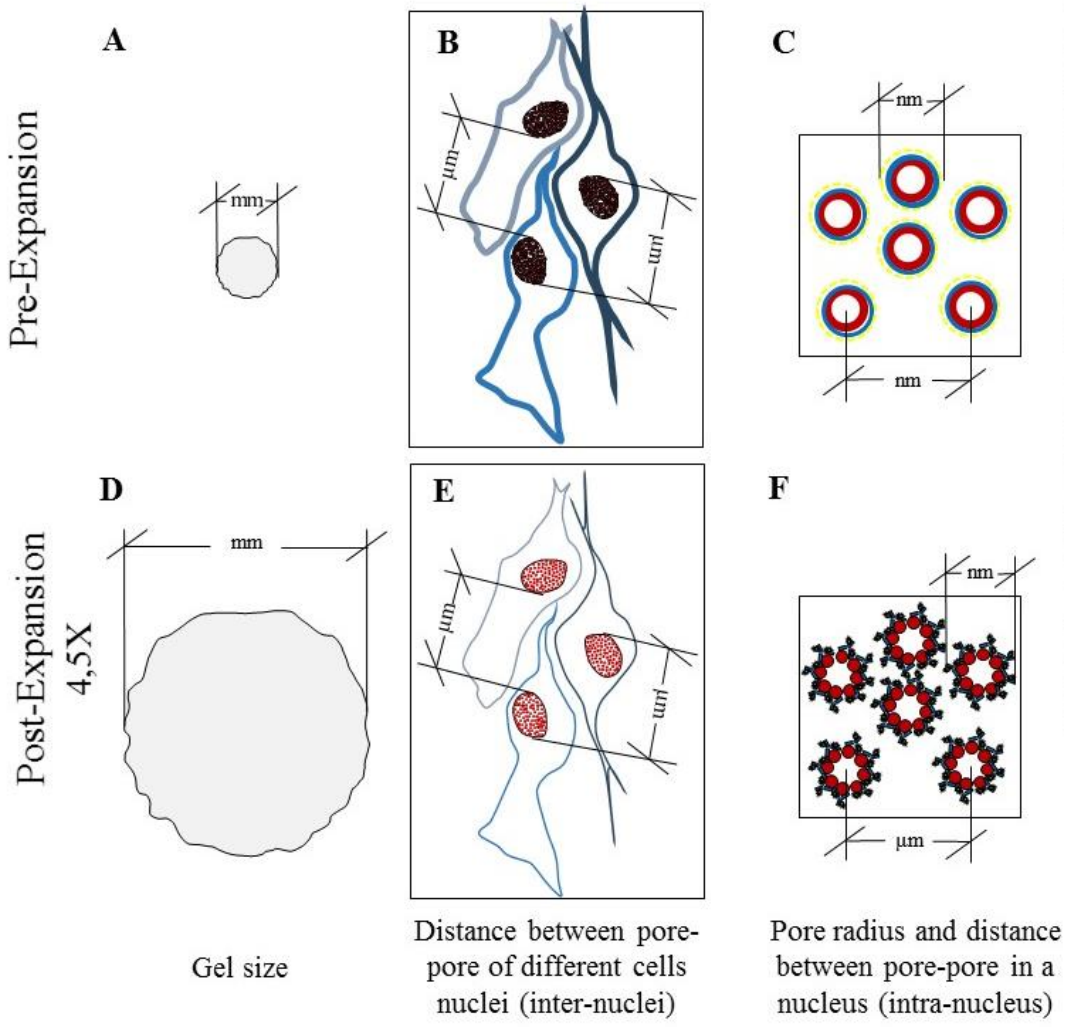

Fig. 18. Schematic representation of the correlation between macro-, micro- and nano-scale expansion of the sample labeled for NPCs. The top and the bottom row show a scheme of Pre- and Post-Ex samples and the strategy to confirm the isotropy and the expansion factor (EF) at different magnitude. At the macroscale level, measuring the gel size Pre- (A), Post-Dig (not showed) and Post-Ex (D). At the microscale level, quantifying the distance between pores in a same nucleus and/or different nuclei in Pre- (B, C) and Post-Ex (E, F); and, finally, at the nanoscale level, applying a Pre- (C), Post-Dig (not showed) and Post-Ex (F) quantitative radius analysis on NPC. The microscale analysis requires the same cells labelled for NPCs before and after expansion, while at the nanoscale is not necessary.

In the next chapters, I will introduce a quantum model to describe the mutations in DNA molecule. Successively, such mutations involved in cancer and aging permit me to introduce the principal components of the NE, focusing on LA and its mutations, responsible for several clinically disorders.

4.1 Point mutation

NE plays an important role in the nuclear stability and gene expression. It is not surprising that mutations involved in *LMNA* and other gene encoding for NE proteins can cause several medical diseases, termed laminopathies. However, is it possible to model a point mutation in a DNA sequence?

In general, mutation is one of the basic phenomena, because without it the development of life from inorganic matter would not have been impossible. However, it can cause rare disease by substitution of single bases in important regions of genome. Before ascribing the hereditary information to DNA, Schrödinger described the mutation as a quantum process, where the carrier molecules of genetic information push from one stable configuration to another configuration, overcoming an energy barrier (*68*).

Subsequently, in 1963, Löwdin described the proton tunneling in the hydrogen bonds between the base pairs in the Watson - Crick Model of DNA (*69*). This model explains the quantum mechanical nature of the hydrogen bonds in DNA nucleotides. In fact, a single proton is shared between two separate atoms, which are in competition to catch the protons in the surrounding environment. The nitrogenous bases involved in this bond are Adenine (A), which specifically pairs with Thymine (T) and Guanine (G), which pairs with Cytosine (C), allowing keeping the two strands of a DNA helix together. In addition to these specific pairing, by moving the protons from its original lone pair into another position, it is possible to obtain a tautomeric form, which can introduce errors into DNA (Fig. 19).

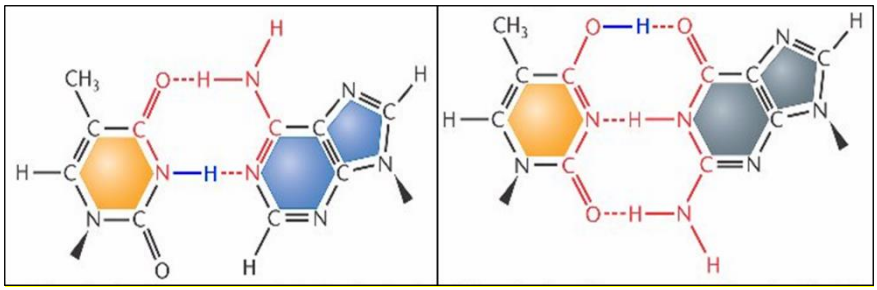

Fig. 19. Tautomeric transition between Adenine and Thymine. Fig. (A) shows the standard base-pairing, while in (B) is the anomalous base-pairing arrangement in the DNA molecule.

Due to the competition of the two electron lone pairs for a single proton, the hydrogen bond can be represented as a double-well potential. In this mode, there is a bump, or potential barrier, separating the two equilibrium positions. In a quantum

mechanical system, the proton can be considered as a wave packet, which penetrates into areas that were forbidden before in the classical system. This "quantum jump" from one state to another, is achieved by means of tunneling through the potential barrier (Fig. 20). For this reason, there is a small but finite probability that the protons will change place within the hydrogen bond, leading to the formation of the tautomeric forms

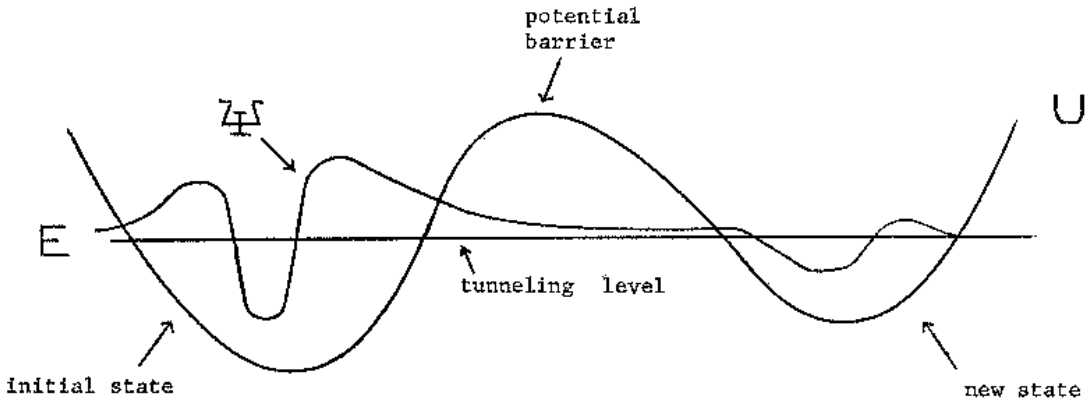

Fig. 20. Tunneling effect of the wave packet that permit to penetrate from one potential to another.

The behavior of the proton is regulated by the time-dependent Schrödinger equation:

$$H\psi = -\frac{h}{2\pi i}\frac{\partial \psi}{\partial t}$$

and the probability of a proton tunneling through the barrier is given by:

$$g = e^{-2s} \qquad s = \frac{2\pi}{h}\int_{x_1}^{x_2} \sqrt{2m(V(x) - E)}\, dx$$

This variation in the base pairing can altering the genetic code, introducing mutations in according to the following scheme (Fig. 21):

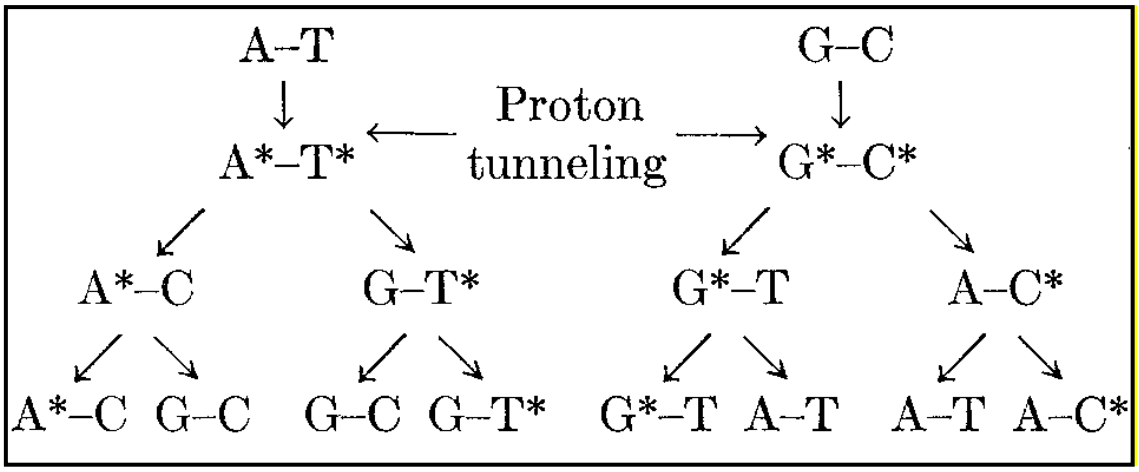

Fig. 21. Formation of the mutations during the cell division.

In this mode, it is possible to model the hydrogen bond as a quantum body problem, by treating the proton as a quantum "wave packet". Obviously, this kind of mutations are reversible (termed transitions) but could be the cause of several medical conditions, such as aging and cancer (*69*).

4.2 Nuclear envelope

Nuclear envelope consists in a highly organized double membranes, divided in an inner nuclear (INM, communicating with the nucleoplasm), and an outer nuclear membrane (ONM, connected to the endoplasmic reticulum in the cytoplasmic side), separate by the periplasmic space (*8*). Both ONM and INM are assemble of lipids and different proteins. In this part, I will introduce briefly the four principal groups of proteins belonging to NE.

The first group of proteins are NPCs, belonging to the NE. They are aqueous channels localized in the nuclear membrane, necessary for the bidirectional exchange of proteins and RNA between the cytosol and the nucleus. They consist of ~30 different polypeptides, called nucleoporins or Nups, which show eightfold rotational symmetry, with an outer diameter of 100 nm and a central transport channel of 40 nm in diameter (*70-72*).

A second group of NE proteins are NETs or NE transmembrane proteins, specifically localizes to the INM (*73*). Although the role of these ~60 proteins is not still characterized, probably they play an important role in the nuclear function such as gene expression and chromatin organization (*74-76*). For example, it has documented the interaction of some of them, such as lamin B receptor (LBR), lamina-

associated polypeptide (LAP) 1, LAP2, emerin, and MAN1 with lamins and chromatin-DNA (*77, 78*). Importantly, mutations or different localizations of INM proteins are linked to numerous human diseases (*79, 80*).

The third group includes the integral membrane proteins localized on the OMN, characterized by a transmembrane domain called KASH (acronym for Klarsicht, ANC-1, Syne Homology), which interacts with SUN (Sad1p/UNC-84)-domain proteins of the INM. This class of proteins, which includes Nesprin1-2, form a dense network, which permits to associate the cytoskeletal filaments (actin) with nuclear elements, like lamins (*81, 82*). This connection is responsible of the mechanosensory role in cells, which transfer force from the nucleoskeleton to the cytoplasmic cytoskeleton.

The last group is represented by nuclear lamins (NL), a meshwork of intermediate filaments which covered the INM, stabilizing the entire nuclear membrane and regulating the chromatin function and expression (*83*) (Fig. 22).

In the next chapter, my attention will be focused on NL, in particular the physiological role and the mutations that cause rare genetic disorder, including dystrophy and premature aging.

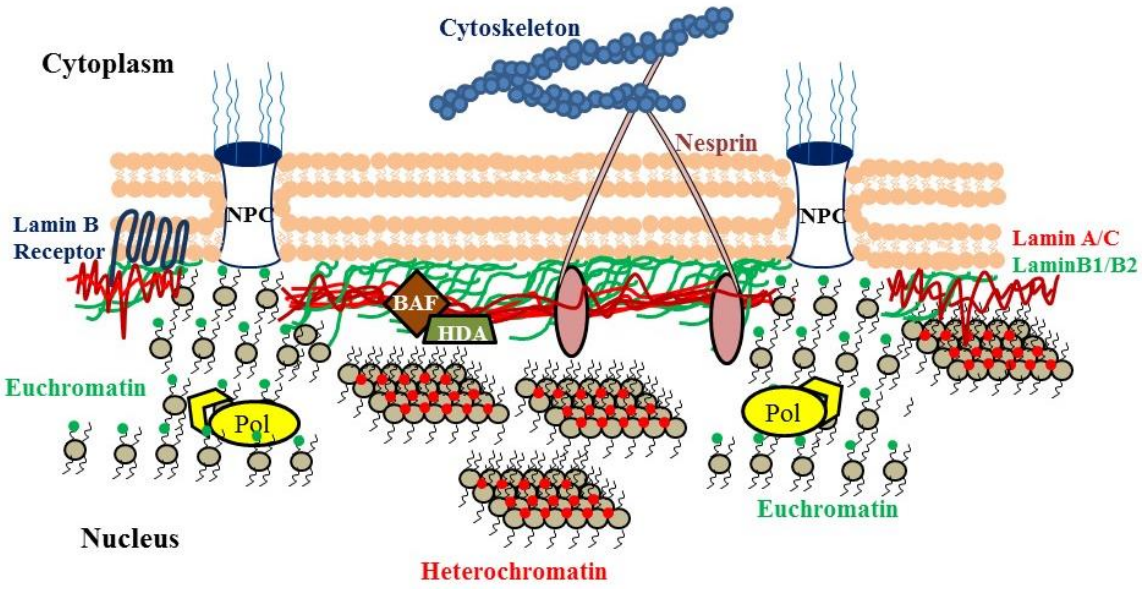

Fig. 22. Schematic illustration of NE and its principal components in normal cells (*84*).

4.3 Nuclear lamins

In the last years, electron microscopy studies showed a filamentous layer between the INM and the peripheral heterochromatin. This high conserved meshwork, later

termed nuclear lamins, is classified as type V intermediate filaments. Based on to their molecular weight, sequence homology and structural features, lamins are subdivided in A- and B-types. By alternative splicing of the *LMNA* gene are produced the isoforms lamin A and C (LA/C) (*85*), while lamin B1 (LB1) and B2 (LB2) are encoded by two separates genes: *LMNB1* and *LMNB2*, respectively (*85, 86*).

The nuclear lamins are characterized by a tripartite structure typical of the intermediate filament, consisting of a highly α-helical central rod domain flanked by a short globular amino-terminal "head" domain and a longer carboxy-terminal "tail" domain (*87*). The central rod domain is divided in four sub-helical regions (coil 1A, 1B, 2A, and 2B), separated by three short linker segments, L1, L12, and L2, of which L12 is the most flexible (*87*). Finally, the tail domain is characterized by a highly conserved structural motif similar to a type s immunoglobulin fold, while the end of all lamins present the NLS sequence for the nuclear localization (*88*) (Fig. 23).

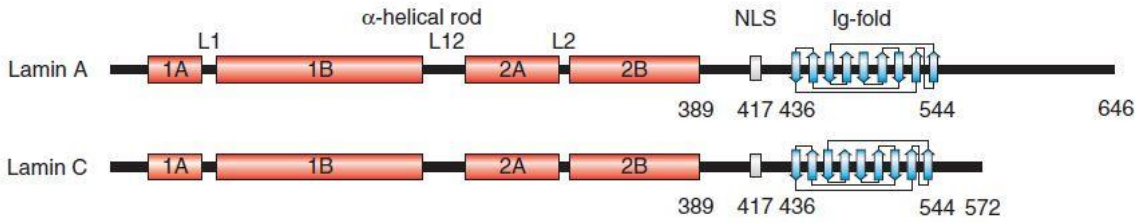

Fig. 23. Schematic representation of mature LA and LC polypeptide chains. The lamin structure consists of a short amino terminal head domain, a central a-helical rod domain (red), and the carboxy-terminal domain containing the NLS and the Ig-fold (*89*).

The process involved in the maturation of nuclear lamins consists in several steps with temporal sequence of controlled posttranslational modifications. These steps, which start with the expression of prelamins, allows obtaining mature lamins forms (*90*). The first posttranslational modification involved in the maturation is the farnesylation by a farnesyltransferase of the cysteine residue, which removes the –AAX by a CAAX prenyl protease (Fig. 24, B). This enzymatic cutting is operate by Rce1 (Ras-converting enzyme 1) and/or Zmpste24 (Zinc metalloprotease related to the STE24 homolog in yeast), also known as FACE1 (farnesylated-proteins converting enzyme) (*90, 91*). Subsequently, a process catalyzed by the enzyme isoprenylcysteine carboxyl methyltransferase permits of carboxymethylated the cysteine residue (Fig. 24, B) (*92*). At this step, while the maturation of B-type lamins is terminated (resulting permantly carboxymethylated and farnesylated), LA is

further processed by Zmpste24/FACE1 to form mature structure, lacking the carboxy-terminal farnesyl- and carboxymethyl-modifications (Fig. 24, B) (*91*). Since LC is 74 residues shorter than the other lamins, does not required these modifications due to the lack of the –CAAX box.

Figure 24. Schematic drawing of a pre-lamin polypeptide chain (A) and the post-translational processes involved in the maturation of lamin A (B) (*93*).

Nuclear lamins determines the shape and size of the cell nucleus, and it is involved in the recruitment of several nuclear membrane-associated proteins, transcription factors and the peripheral heterochromatin. For these reasons, it plays an important role for most of the nuclear activities, such as chromatin organization, DNA replication and transcription, cell cycle regulation, nuclear positioning within the cell and assembly/disassembly of the nucleus during cell division (*93*). In fact, 40% of the mammalian genome is constituted by lamina-associated domain (LADs), enriched in $(GA)_n$ repeats and recruited by the NLs through specific DNA-binding proteins (*94*). Not only DNA sequence, but also it can interact with chromatin. In general, the NL tends to be in contact with compact chromatin (heterochromatin), while NPCs are surrounded by much less or decondensed chromatin (*95*). It has documented that this interaction, whether direct or indirect, has effect on the epigenetic modification of the histones. In fact, $LMNA^{-/-}$ cells or the expression of

mutated form of LA (called progerin, see Hutchinson-Gilford Progeria Syndrome (HGPS)) leads a partial loss of peripheral heterochromatin (*96-98*). These changes in the chromatin organization are linked to the alterations in histone modifications including reductions in trimethylated H3K9, trimethylated H3K27 and an increase in trimethylation of H4K20 in that pathological state (*96, 99*).

In addition, nuclear lamins control the mechanical properties of the cell by connecting to the cytoskeleton. In fact, LA/C-deficient cells show alteration in the mechanotransduction signal, a reduction of the mechanical stiffness and defective cell migration (*100-102*). These characteristics are attribute to the altered connection between the nucleoskeleton and the cytoskeleton.

The complexity and the role of this network can be understood by studying mutated forms of the lamins gene. In fact, mutation in *LMNA* gene caused more than 10 different disorder called laminopathies, which include neuropathies, muscular dystrophies, cardiomyopathies, lipodystrophies and progeroid syndromes.

4.4 *LMNA*: one gene, many diseases

LMNA was characterized in 1993 and subsequently mapped in the chromosome 1q21.2-q21.3 (*103*). The first disease caused by *LMNA* mutations was Emery-Dreifuss muscular dystrophy (*104*). Patients with this autosomal dominant syndrome present early contractures of the elbows, Achilles tendons, and posterior neck, rigidity of the spine, slowly progressive muscle weakness in the upper arms and lower legs, and dilated cardiomyopathy (*105*). Subsequently, other mutations on this gene were linked to other dominantly diseases affecting striated muscle, including dilated cardiomyopathy 1A (*106*) and limb girdle muscular dystrophy type 1B (*107*).

In 1998 was demonstrated that Dunnigan-type familial partial lipodystrophya was also connected to *LMNA* mutations. This group of disorders, termed Lipodystrophies, are characterized by the absence or reduction of subcutaneous adipose tissue, associated with insulin resistance and frequently diabetes mellitus (*108, 109*). In fact, Cao and Hegele identified a missense mutation linked to the lipodystrophy phenotype in exon 8 leading to a R482Q amino-acid substitution (*110*). Subsequently, missense mutations in exon 11 of LMNA were identified in

other cases, leading to R582H and R584H aminoacid substitutions in the lamin A proteins (*111, 112*).

In addition, *LMNA* mutations can damage peripheral nerves. Indeed, patients with Charcot Marie-Tooth type 2 diseases have slight or absent reduction of nerve conduction velocities, loss of large myelinated fibers, and axonal degeneration (*113*). Another clinical example of *LMNA* mutations are the progeroid syndromes, in particular Hutchinson-Gilford Progeria Syndrome (HGPS). HGPS is a lethal congenital disorder characterized by accelerate ageing in children and early death (*114-116*). The genetic basis for HGPS is a single nucleotide mutation in the *LMNA* gene. The substitution 1824 C > T is the most prevalent of the 18 mutations associated with HGPS, which activates a cryptic splice site during the mRNA maturation, missing 150 nucleotides (*117*). Next, this aberrant mRNA is then translate into a protein termed ΔLA50 or progerin, that is lamin A lacking 50 amino acids within its C terminus (*117, 118*). Other mutations are involved in this abnormal splicing event, and are 1822 G > A, 1821 G > A, and 1968 + 1 G > A (*117, 119*). As seen previously for lamin A, in HGPS the first steps involved in the maturation are performed, but the last cannot be completed due to the point mutation. This results in the production of a permanently farnesylated form of the protein, characterized by high affinity with the nuclear membrane, which causes abnormalities in the nuclear structure and function. In fact, fibroblast from HGPS patients are characterized by altered nuclear size and shape, pathological blebs, thickening of the nuclear lamina with nuclear pore complexes clustering and loss of peripheral heterochromatin (*99, 120-123*) (Fig. 25).

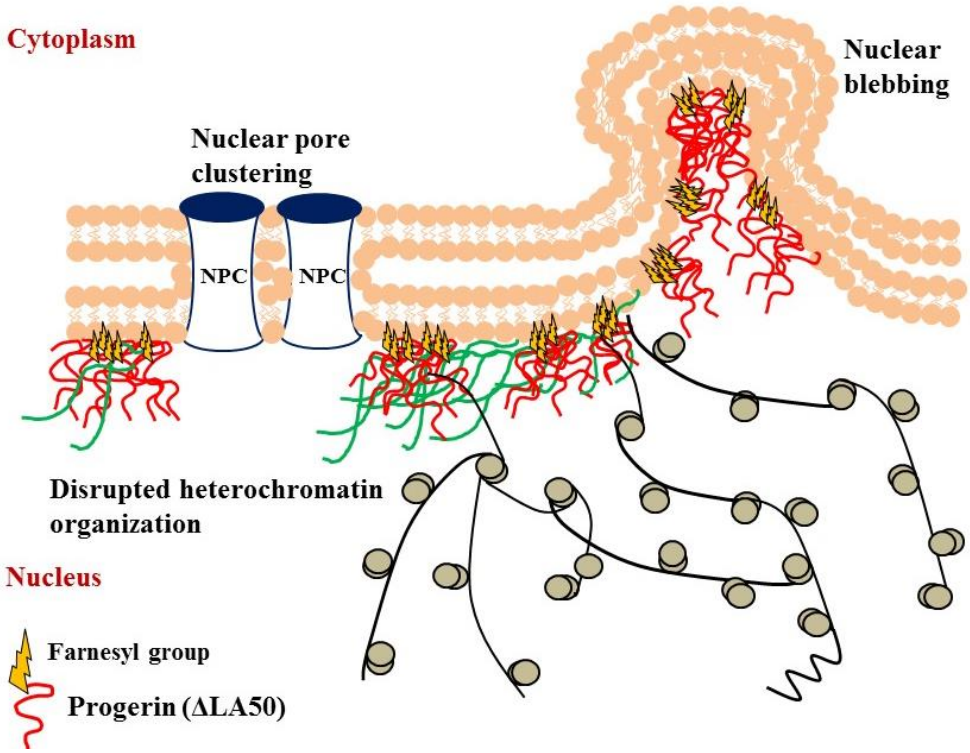

Fig. 25. Schematic illustration of the genomic instability due to the expression of progerin (*84*).

At birth, infants with HGPS are healthy and showed signs of premature ageing only after 1-2 years. The typical phenotypic characteristics are alopecia, protruding ears with absent lobes, prominent scalp veins and forehead, classical facial features including frontal bossing, a glyphic (broad, mildly concave nasal ridge) nose, prominent eyes, thin lips and micrognathia (*124*). In addition, HGPS patients have short stature (100-110 cm) with thin legs, low weight (10-15 kg), limited joint mobility, incomplete sexual maturation and lack of subcutaneous fat. Caused by progressive atherosclerosis of the coronary and cerebrovascular arteries, the death occurs, on average, at 13 years old (*116, 124*) (Fig. 26).

Fig. 26. Photographs of a 7 year-old girl with HGPS (LMNA c.1824C>T, p.G608G). This patient presents the typical phenotypes described before, including alopecia, thin and tight skin, loss of subcutaneous fat, prominent scalp veins and forehead, prominent eyes, protruding ears, thin lips, and small jaw (*125*).

In 2007, McClintock et al showed that the sporadic cryptic splice in exon 11 of *LMNA* occurs *in vivo* in normal fibroblasts, demonstrating a possible role of progerin in the terminal differentiation or senescence (*126*). These evidences proved that HGPS could be a useful model to understand the molecular mechanism involved in the normal aging. In addition, possible therapeutic strategies, such as farnesyltransferase inhibitors already used on HGPS cells, might be used to prevent normal aging and other age-related pathologies.

In summary, since the late 1990s genetic studies have shown that *LMNA* mutations can cause about a dozen clinical disorders with different names and characteristics. These can be classified into diseases affecting predominantly striated muscle, adipose tissue, peripheral nerve, or multiple tissues resulting in progeroid phenotypes. Another classification is based on the tissue – selective functions correlate with the mutation at different proteins domains (Fig. 27). In fact, the majority of the mutations that cause Dunnigan-type familial partial lipodystrophy and mandibuloacral dysplasia are caused by aminoacid substitutions in the immunoglobulin type fold in the tails of lamins A and C. Instead, substitution in the

rod domain, in general are associated with the peripheral neuropathy. Frame deletion of 50 amino acids from the tail of prelamin A, caused by mutations in the exon 11 of *LMNA*, is representative for classical HGPS.

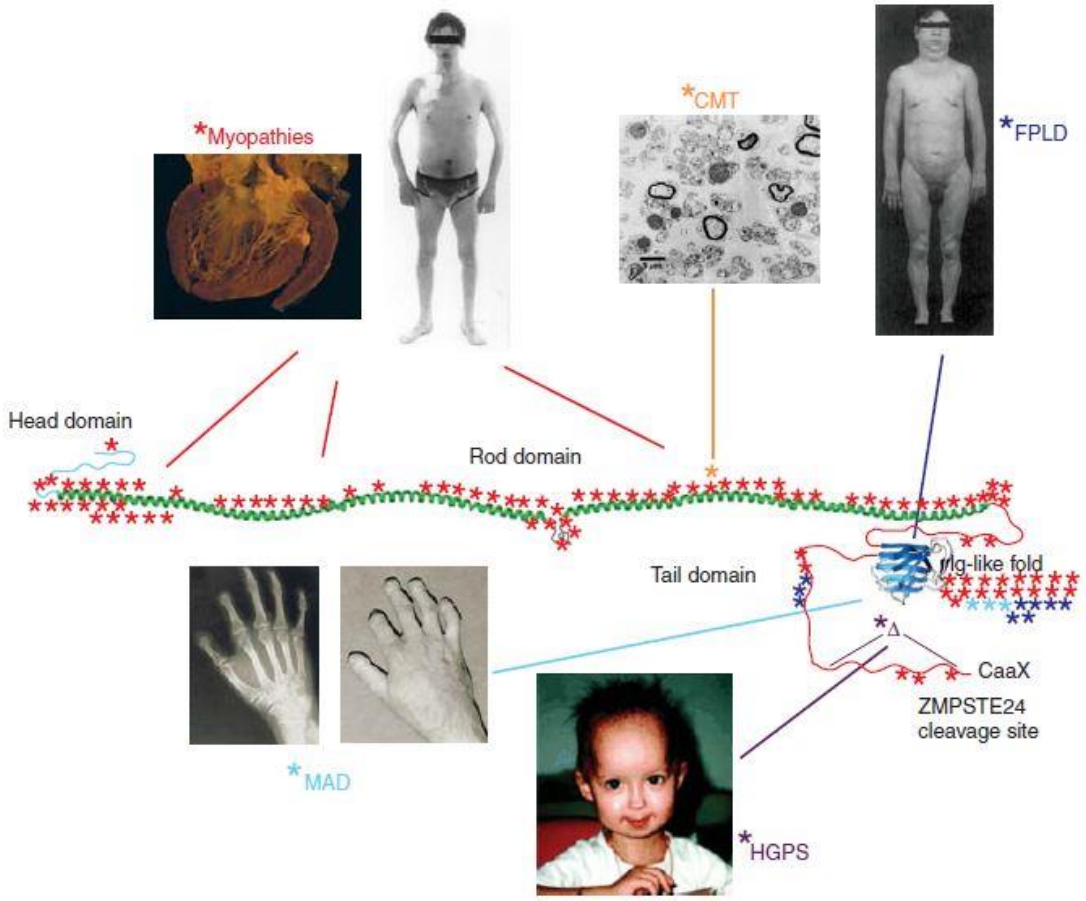

Fig. 27. Correlation between the mutations that affected different protein domain and tissue specificity in the *LMNA* gene. Diagram of a prelamin A molecule with mutations causing laminopathies indicated. Mutations causing Dunnigan-type famililal partial lipodystrophy (FPLD, dark blue asterisks), Charcot-Marie-Tooth disease (CMT, orange asterisk), mandibuloacral dysplasia (MAD, light blue asterisks), or Hutchinson-Gilford progeria syndrome (HGPS, purple asterisk) are correlated with specific areas of the molecule, whereas mutations causing myopathies (red asterisks) are found throughout. Photographs are reproduced with permission from Elsevier (*127-129*), Macmillan Publishers Ltd (*109, 130*), and the American Association for the Advancement of Science (*118*).

5 Material and Methods

5.1 Bright monomeric near-infrared fluorescent proteins for live cell imaging

During my Ph.D., I had the opportunity to test different fluorescent organic dyes and proteins for live and fixed biological samples. In the first part of my research project, my attention was focused on a new genetically encoded monomeric protein engineered from bacterial phytochrome, called miRFP (*131*). These new class of proteins are excited and fluoresce close to or within an NIR tissue transparency "optical window" (approximately 650-900 nm) where background autofluorescence is low and light scattering is reduced (*60*). We obtained from the Department of Anatomy and Structural Biology, Albert Einstein College of Medicine in US two plasmids encoding for two fusion proteins: miRFP703-tubulin and miRFP703-H2B (spectral characteristics of miRFP in Fig. 28).

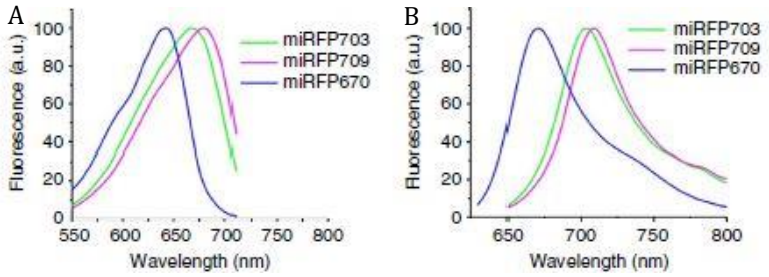

Fig. 28. Fluorescence excitation (A) and emission (B) spectra of engineered miRFP670, miRFP703 and miRFP709. My attention was focused on the miRFP703 variant (*131*).

5.1.1 Bacteria transformation, cell culture and transfection

Transformation in DH5α competent bacteria of two plasmids encoding miRFP703-Tubulin and miRFP703-H2B was performed by heat shock at 42 °C. DNA plasmid purification was executed using Mini-prep kit (Macherey-Nagel). For fluorescence microscopy, HeLa cells were grown in DMEM medium supplemented with 10% FBS, 1% penicillin – streptomycin and 1% glutamine. PC3 cells were grown in F12 medium supplemented with 7% FBS and 1% penicillin – streptomycin. Cells were seeded on 18 mm cover glass inside a 12-well plate at 60-80% confluence. Transfection was performed by Effectene reagent (Qiagen). Cells were incubated at 37 °C and 5% CO_2 24 h before imaging. A stable cell-line obtained from HeLa cells

was selected with 0.7 mg/ml of antibiotic G418. The positive cells were sorted by FACS equipped with 633 nm laser line and 780/60 BP emission filter.

5.1.2 Multicellular tumor spheroids

HeLa stable cell-line expressing miRFP703 fused to histone H2B was used to obtain multicellular tumor spheroids (*132*) using suitable microplates with non-adherent surfaces to maintain the cells in a unattached state (Corning) (Fig. 29). The number of cells seeded was around 10^3 – $2x10^3$ and they were incubated at 37 °C and 5% CO_2 for at least 48 h before imaging. Imaging of spheroids was performed using Confocal Spinning Disk equipped with an incubator (Okolab system) and inverted Selective Plane Illumination Microscopy (iSPIM).

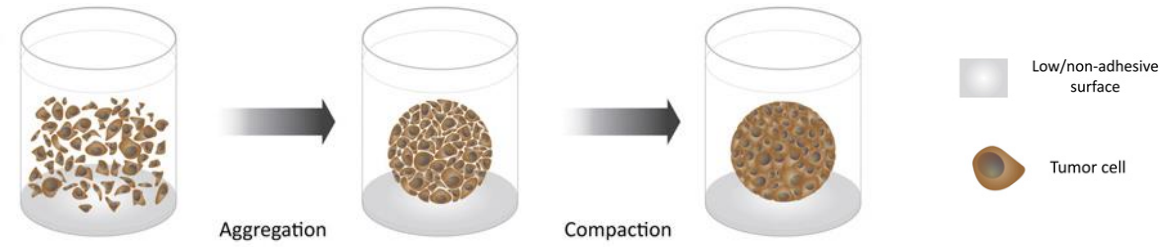

Fig. 29. Steps involved in the tumor spheroid formation (*132*).

5.2 Correlative light and Electron Microscopy (CLEM)

Correlative light and electron microscopy (CLEM) is a powerful tool that allows investigating the dynamic processes *in vivo* using fluorescence microscope with the resolution of the electron microscope. In this part of the work, the diaminobenzidine (DAB) polymerization was used for the direct visualization of fluorophores involved in the photo-bleaching process. In their exited state, some fluorescent proteins (such as GFP (*133, 134*)) (Fig. 30) and organic dyes (such as TMR and DRAQ5 (*135, 136*)) can generate reactive oxygen radicals ($^1O_2$) during the bleaching process, which interact very fast in their immediate vicinity with DAB monomers. This process produces an electron dense precipitate (the insoluble DAB polymer) detectable after staining with osmium (OsO_4), and visualized by EM through thin sections and by electron tomography for 3D analysis (*19, 133, 137*) (Fig. 30). This method is considered one of the best labelling strategy, because allows obtaining a resolution in the range of 5–10 nm (*134*).

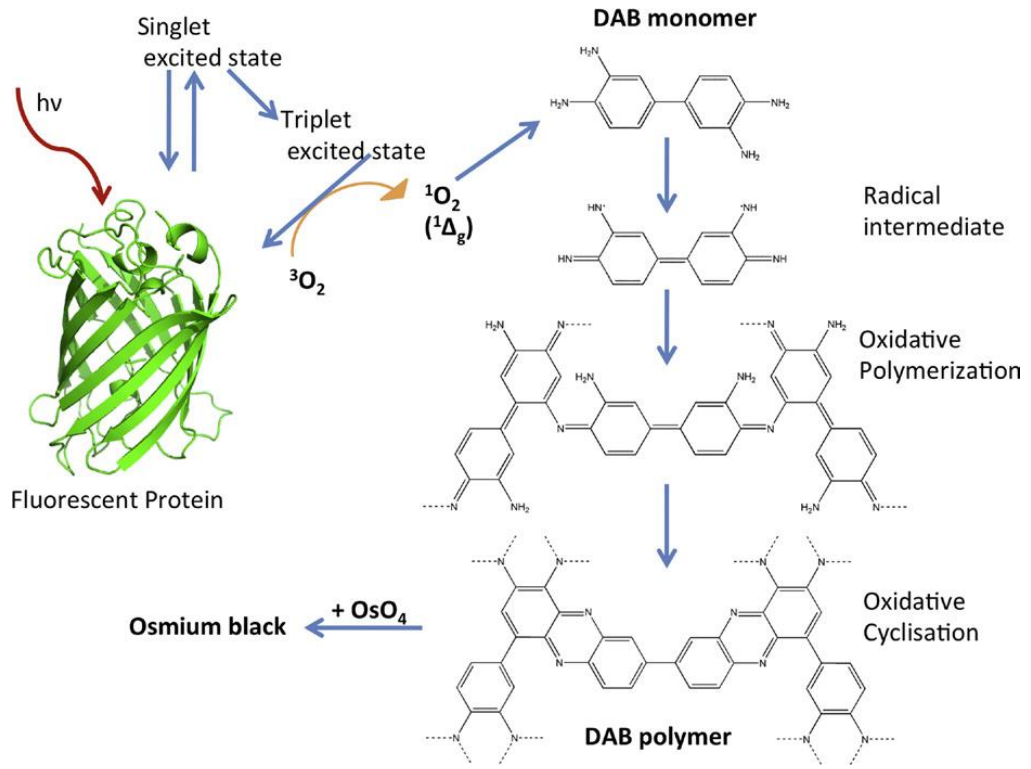

Fig. 30. Schematic representation of the DAB photo-oxidation obtained through GFP photo-bleaching. The excited electrons of GFP generate singlet oxygen radicals, which react with DAB monomers, inducing the polarization process. The insoluble deposition of DAB polymer can be stained by osmium tetroxide (*133*).

A good candidate for a CLEM experiment is the TMR fluorophore (*135*) conjugated to benzylguanine substrate (Fig. 31), necessary to tag the modify enzyme SNAP-tag. The reaction involved between this small protein and its substrate occurs rapidly and specifically to covalently label intracellular proteins of interest. The organic dye TMR (excitation 545 nm, emission 575 nm) is a permeable-dye compatible with live cell imaging and able to induce DAB photo-oxidation during the photo-bleaching process (*135*).

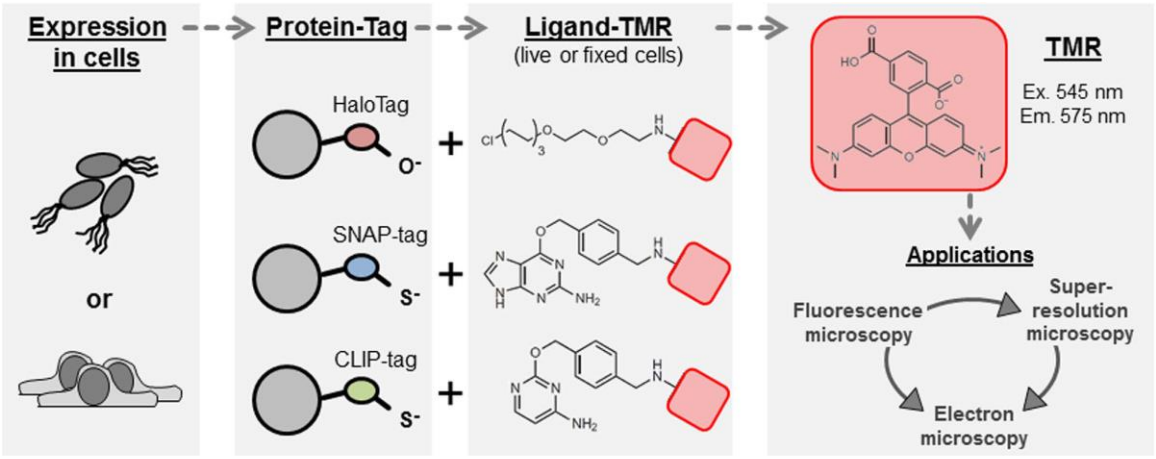

Fig. 31. Proteins of interest are tagged with genetically encoded markers HaloTag, SNAP-tag or CLIP-tag and expressed in eukaryotic cells. TMR is the organic fluorophore involved in the photo-oxidation process (*135*). This strategy can be performed in different fields, such as super resolution techniques (STED) and electron microscopy.

5.2.1 Cell culture, self-labelling reaction and DAB-polymerization

HeLa cells were grown in DMEM supplemented with 10% Fetal Bovine Serum and 1% pen/strep and glutamine. For the transfections, HeLa cells were seeded on 6-well at 60-80% confluence. After 24 h, cells were transiently transfected with the plasmid Lamin A-SNAP tag (#58193, Addgene) using Effectene reagent (Qiagen). After incubation at 37 °C and 5% CO_2 for 24 h, the cells were extracted and seeded on opportune Petri Dish with grid (MaTek). To visualize Lamin A using a fluorescence microscope, the appropriate ligand tetramethylrhodamine (TMR) was added to the transiently transfected sample. After incubation at 37 °C, 5% CO_2 for 30 min, the cells were washed twice with 1 mL of PBS. To allow the excess SNAP-Cell TMR to diffuse out of the cells, the sample were incubated with complete medium for 15 min. After washing twice with 1 mL of PBS, live cell imaging was performed using spinning disk confocal microscope at 37 °C, 5% CO_2. Successively, the cells were fixed with 2% glutaraldehyde and 2% sucrose in PBS for 30 min at room temperature. After several washes with cold PBS, 100 mM glycine for 1 h and 10 mg/ml sodium borohydrate for 40 min were added to block endogenous enzyme activity and endogenous autofluorescence, respectively. For the photo-oxidation process, the sample was incubated in a solution of 1–2 mg/ml DAB in TBS. The illumination of samples for DAB photo-oxidation of fixed cells occurred with a bright fluorescence lamp on an inverted microscope, using a high-numerical-aperture objective (60x, NA 1.4) with green light (filter excitation wavelength 515–560 nm) for 15-20 min (concomitantly with complete disappearance of fluorescence). After three washes with cold distilled water to block the reaction, post-fixation of the sample was performed in 1% osmium tetroxide reduced by 1.5% potassium ferrocyanide for 30 min on ice. After dehydration by incubation in graded ethanol series of 70%, 90%, 96%, 3 × 100% ethanol, 5 min each, the sample was embedded in EPON resin for 1 h at room temperature and incubated in an oven to polymerize at 65 °C for 48 h. Sections of about 70 nm corresponding to the bleach cells were cutted with a diamond knife on a Leica EM UC6 ultramicrotome and deposited on a TEM grid.

5.2.2 Image acquisition

For live cell imaging, the transfected cells were imaged using Spinning disk confocal microscope (Nikon eclipse Ti coupled with Andor Revolution XD) with a 60x, 1.4 NA oil immersion objective, equipped with an incubator. Photo-bleaching and DAB polymerization was performed with a bright fluorescence lamp with green light (filter excitation wavelength 515–560 nm) and high-numerical-aperture objective (60x, NA 1.4).

Transmission electron microscopy (TEM) images were collected with a FEI Tecnai G2 F20 (FEI Company, The Netherlands) and a Jeol JEM 1011 (Jeol, Japan) electron microscopes and recorded with a 1 and 2 Mp charge-coupled device (CCD) camera (Gatan BM Ultrascan and Gatan Orius SC100, respectively).

5.3 ExM protocol

Chozinski and colleagues proposed a variant of the originals ExM in which the samples are labelled with conventional antibodies (*30*) (Fig. 32). We adapted our STED labelling protocol with the expansion microscopy proposed by Chozinski in order to perform STED-ExM. In general, for super resolution techniques and in particular for ExM, a labelling density using antibodies is critical for the final resolution and artifact-free images (*138*). This is due to the strong diminution of fluorescence signal, caused by the digestion of antibodies and expansion of the sample. For this reason, high optimization of the immunofluorescence protocol is request.

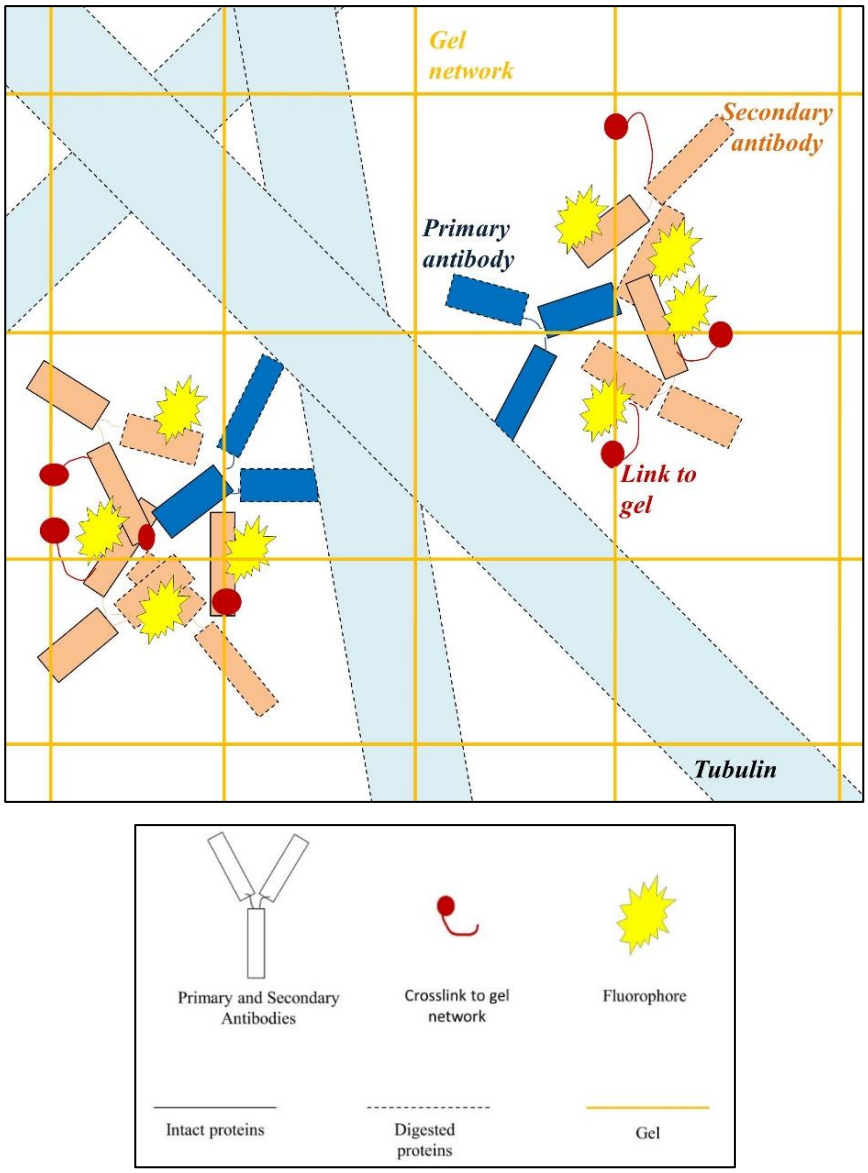

Fig. 32. Schematic representation of the cytoskeleton (tubulin filaments, in blue), primary and secondary antibodies (blue and orange) and the crosslinker to matrix gel (red dot). In this method, GA or MA-NHS are used to label the sample with polymer - linking groups after conventional immunostaining (*7*).

5.3.1 Cell culture, transfection and immunostaining protocol

Hos and Hek cells were grown in DMEM supplemented with 10% Fetal Bovine Serum and 1% pen/strep and glutamine. For nuclear pore labelling, immunofluorescence was carried out using an adopted protocol from Szymborska et al. Hos cells were plated at 70% confluency on 18 mm coverglass and grown overnight. The cells were pre-extracted with 2.4% PFA and 0.3% Triton-X100 in PBS for 3 min. After fixation with 2.4% PFA for 30 min, the cells were blocked for 1 hour with 5% BSA. Next, the cells were incubated overnight at 4 °C with primary antibody (Nup153, ab84872) in

BSA 5%. After washing several times in PBS, the cells were incubated with the secondary antibody at room temperature for 1 hour. For α-Tubulin, Hek cells were pre-extracted with 0.25% glutaraldehyde and 0.3% Triton-X100 for 3 min and successively fixed with 3,2% PFA and 0,25% glutaraldehyde in PBS for 10 minutes. After rinsing with PBS and blocking with 5% BSA and 0.3% Triton-X100 for 1 h, the sample was incubated overnight at 4 °C with primary antibody. After washing several times in PBS, the cells were incubated with the secondary antibody at room temperature for 1 hour.

For lamin A, Hek cells were dehydrated with methanol for 10 min at -20 °C. After BSA incubation, primary antibody was incubated overnight at 4 °C overnight.

For the transfections, HeLa and Hek cells were grown in DMEM medium supplemented with 10% FBS, 1% penicillin–streptomycin and 1% glutamine. For fluorescence and ExM experiments, cells were seeded on 18 mm cover glass inside a 12-well plate at 60-80% confluence. After 24 h, cells were transiently transfected with the plasmid EGFP - ΔLA50 (#17653, Addgene (*139*)) using Effectene reagent (Qiagen). Cells were incubated at 37 °C and 5% CO_2 24 h before imaging. In according to Chozinski at al., to link the antibodies and the fluorescent proteins to the gel, labelled sample was rinsed in 0.25% GA for 10 min or 25 mM MA-NHS for 60 min at room temperature (*30*).

5.3.2 Polymerization, Digestion and Expansion

The samples were soaked in a gelation solution of 2M NaCl, 2.5% (Wt/Wt) acrylamide, 0.15% (Wt/Wt) N,N′-methylenebisacrylamide, 8.625% (Wt/Wt) sodium acrylate, 0.2% (Wt/Wt) tetramethylene diamine (TEMED) and 0.2% (Wt/Wt) ammonium persulfate (APS) in DI water, with the APS added last. The salinity concentration and the ratio between acrylamide and N, N′-methylenebisacrylamide determine a mesh pore size of 1 to 2 nm (*6*). The gelation solution (~50 µl) was placed on the hydrophobic surface, and the coverglass was placed on top of the solution with cells face down. Gelation was allowed to proceed at 37 °C for 20 min. The coverglass and gel were removed with tweezers and placed in digestion buffer (1 × TAE buffer, 0.5% Triton X-100, 0.8 M guanidine HCl) containing 8 units mL^{-1} Proteinase K added freshly. Gels were digested overnight. In Fig. 30 we show a sketch how the sample labelled for tubulin results after the steps

described up to now. To finalize the sample preparation and effectively expand it, the gel was removed from digestion buffer into 60 mm petri dish. Small gel stripes were cut with a thin glass-slice and observed in confocal. After mapping the cells in the gel, the samples were placed in ~50 mL DI water to expand. Water was exchanged every 30 minutes and 4 times until expansion was complete.

5.3.3 Fluorescence microscopy

Both Pre-, Post-Dig and Post-Ex NPC imaging are obtained using a commercial Leica TCS SP5 gated STED-CW microscope (Leica Microsystems, Mannheim, Germany) with a 100x, 1.4 NA oil immersion objective. The excitation and depletion wavelengths are 488 nm and 592 nm respectively, with a collection spectral window of 510-560 nm.

Spinning disk confocal microscope (Nikon Eclipse T*i* coupled with Andor Revolution XD) is used to map a small portion of the gel before expansion using large image modality, with a 20x, NA 0.75 dry objective (Fig. 50). To visualize nuclei and α-tubulin labelled with Hoechst 33342 and Atto647N, the excitation wavelengths used are 405 nm and 640 nm respectively. After mapping different areas, specific cells in different region are acquired using confocal Leica TCS SP5 microscope, visualizing Nup153 and α-Tubulin labeled with Alexa Fluor 488 and Atto647N, with a 100x, 1.4 NA oil immersion objective (Fig. 50, B and C).

To reduce hydrogel drift during microscope acquisition, Poli-L-lysine (Sigma) is applied on 24 mm round #1.5 coverglass for 30 min at 37 °C. After, the expanded gel is soaked in a solution of 2% Agarose to immobilize it.

The same cells acquired in the pre-expansion modality are imaged after expansion using Nikon A1 Confocal Microscope with a 60x Obj, NA 1.4 oil immersion objective. Due to the three-dimensional expansion it is challenging to find the same focus. Thus, different stacks are acquired for the basal portion of the nuclei and successively aligned and summed by Fiji (*140*). After cropping an area of interest, the images are normalized using Fiji.

5.3.4 Data analysis

For the radius analysis, single pores are manually cropped with a diameter of 0.2, 0.4 and 0.9 μm using Fiji. The radius of each pore is calculated using a custom Matlab

script. This algorithm calculates multiple radial intensity profiles along different orientations. For each orientation, the radial distance between the maximum value of the profile and the centre is calculated. Finally, the radius of the pore is calculated as the average of these radial distances. In order to obtain an average value and standard deviation for each sample, we fit the histogram obtained from all the analysed images with a Gaussian distribution.

In the case of the ExSTED sample, for each pore, we also generate an angular intensity profile, by plotting the maximum value of the radial intensity as a function of the orientation. In order to obtain the angular position of the subunits, we fit the angular intensity profile with a multi-Gaussian peaks function. Peaks with a width larger than a given threshold are discarded to reject unresolved subunits (Fig. 32). Peaks with an amplitude lower than a given threshold are discarded to reject unspecific labelling. For each pore, the angular position of the first detected peak is subtracted from all the detected peak angle values. In other words, the first detected subunit is used as a reference (angle=0°). The cumulative histogram relative to the angle values retrieved from the analysis more than 100 pores is fitted with a 7 peaks-Gaussian fit.

Finally, for the microscale analysis, the Pre- and Post-Ex image registrations are carried out using the affine image registration in the TurboReg plugin (*141*) (Fig. 51, C), which cuts, translates and rotates to overlap the images. The Fast 2D Peak Finder script (Version 1.12.0.0, Natan, 11 Oct 2013) is used to calculate the distortion error (Fig. 5, D).

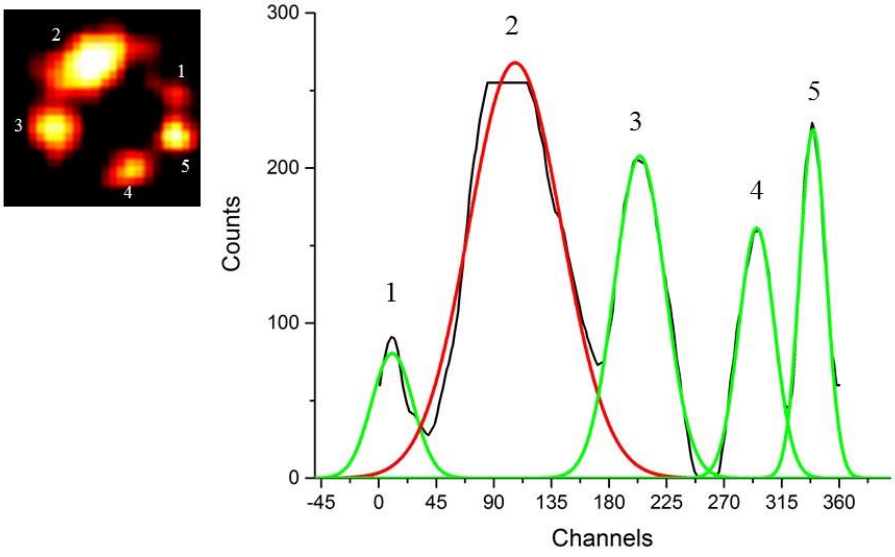

Fig. 32. Confirming octagonal symmetry of Nup153. Example of analysis performed in a single pore. Using the algorithm described in Materials and Methods, we fit the angular profile using a multi-Gaussian peaks function in order to obtain the angular position of the subunits for each peak. Moreover, we discard the peaks with wide angular values (e.g., subunit 2, red peak) and low amplitude, to reject unresolved subunits (e.g., subunit 2) or aspecific labelling. We repeated this analysis for each pore we selected (N>100).

6 Results and discussion

The optimization of the expression of new fluorescent proteins (miRFP703 (*131*)) and the self-labelling method (SNAP tag technology) was my first research project. These strategies allow me achieving 2-colours, tumor spheroids and super-resolved images of living samples.

After, SNAP-tag technology was used to investigate nuclear envelope by combining electron and fluorescence microscopy (CLEM).

These methods have permitted me to achieve more confidence about the preparation of live and fixed samples. In addition, several optical approaches were used to perform these experiments, including inverted Selective Plane Illumination (iSPIM), Confocal, Spinning Disk and STED microscopy.

6.1 Live cell imaging of miRFP703

After the transformation in bacteria and purification of plasmid DNA, the first step was to test the construct miRFP703 fused to tubulin. A confocal microscope was used to evaluate the transfection efficiency in different cancer cells (Fig**.** 33, A).

For an additional detection channel in multicolor live imaging, two different constructs encoded for miRFP703 and SNAP-Tag labelled with Tetramethylrhodamine (TMR) were co-transfected in HeLa cells. As seen previously, TMR is a commercially available substrate for SNAP-tag technology characterized by red emission and membrane permeability (8). The image (Fig. 33, B) was performed using Spinning Disk confocal microscope:

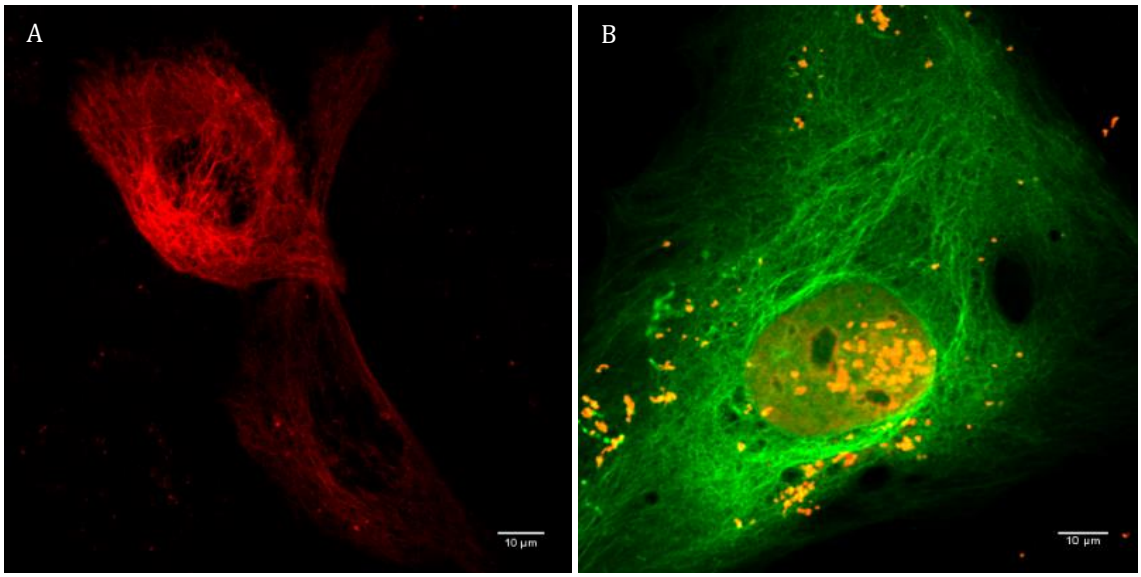

Fig. 33. (A) PC3 cells expressing miRFP703-Tubulin. (B) Hela cells expressing miRFP703-H2B and tubulin-Snap tag with TMR. Spinning Disk live confocal imaging. Exc 640 and 560 nm. Obj 100X, NA: 1.4. Scan format 512x512.

Next, our goal was to evaluate if miRFP703 was a good marker for super resolution technique, in particular for STED nanoscopy. To verify it, different protocols and optimization conditions were tested. Due to the low photo-stability after fixation and the excitation caused by the STED beam ($\lambda = 775$ nm), live samples were used to image miRFP703-tubulin (Fig. 34).

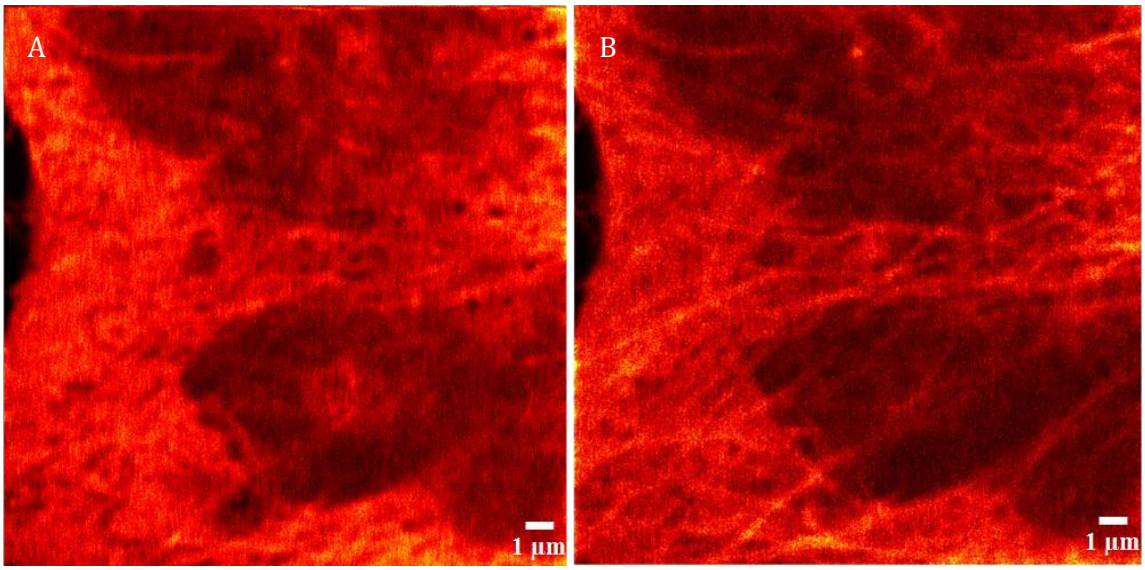

Fig. 34. (A) Confocal and (B) STED imaging of HeLa cells expressing miRFP703 fused to tubulin.

Successively, the increasing curiosity of studying live sample leads me to investigate structures that are more complex than a single cell-layer. For this reason, the stable cell line (HeLa cells expressing miRFP703 fused to histone H2B, Fig. 35, A-C) was used to obtain multicellular tumor spheroids (MTCSs) and analyze them using live fluorescent microscopy. MCTSs are characterized by cell heterogeneity that reflect *in vivo* tumor. Large 3D spheres (> 500 µm) have an outer layer of proliferating cells, an inner layer of quiescent cells and a necrotic core (*132*). miRFP703 is a good marker for tumor spheroids, because its red shifted excitation spectra penetrate with high efficiency the 3D structures, and the scattering and autofluorescence is reduced. Fig 35, D-F shows a large spheroid (~ 400 µm) obtained by seeding $5x10^3$ visualized using Spinning Disk confocal (D) and inverted Selective Plane Illumination Microscopy (iSPIM) (E, F).

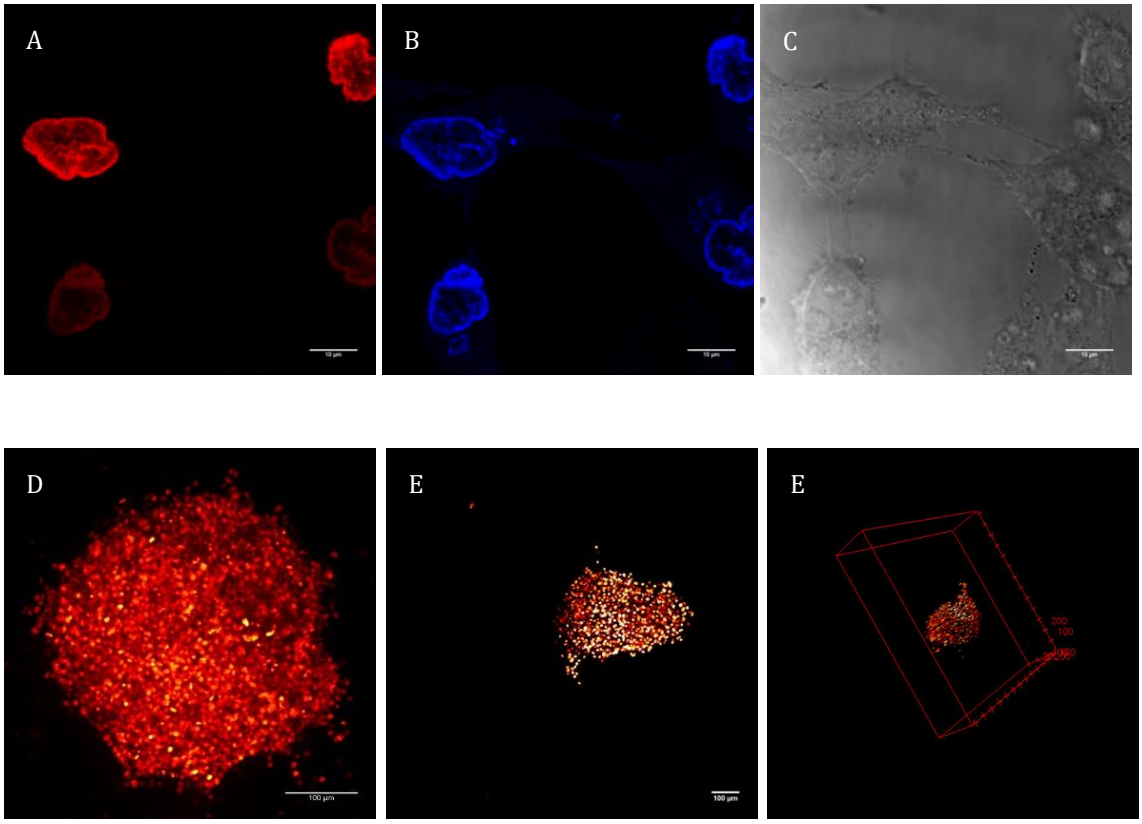

Fig. 35. Live confocal imaging of stable cell line express miRFP703-H2B (A, in red) stained with Hoechst (B, in blue); brightfield imaging (C). Exc: 640 nm; Obj: 100X, NA: 1.4.
Fig. 35 (D) shows a tumor spheroid generated using HeLa cells expressing stably miRFP703 fused to histone H2B. Confocal spinning disk live imaging. Exc 640 nm. Obj 10X, NA 0.30; Z projection. Fig. 34 (E, F) show a tumor spheroid imaged by iSPIM. Exc 640 nm. Obj excitation-detection 10X, NA 0.30.

Finally, MTCSs were employed to test a specific class of chemotherapeutic agents, called photosensitizers (PSs). PSs combined to visible light are used in the photodynamic therapy (PDT) as anti-cancer drugs, because they are able, upon irradiation, to produce reactive oxygen species able of destroying tumor cells (*142, 143*).

6.2 Correlative microscopy to investigate Lamin A meshwork

My interest about the nuclear envelope (NE) leads me to use CLEM to examine it as much resolution as possible. The possibility to image live cell by optical microscopy combined with the EM resolution motivated me to use this approach. In particular, my principal goal is to optimize the conditions necessary to produce a DAB precipitate of sufficient quality. In this way, we are able to investigate the lamin A network by using electron microscope.

Numerous expedients are necessary to implement a CLEM experiment. First, it was necessary to test the plasmid Lamin A fused to SNAP-tag and valuate the efficiency of TMR reaction inside the nucleus. As you can see in Fig. 36, the high signal-to-noise ratios and the excellent brightness allow concluding that the self-labelling approach on nuclear lamin A works perfectly in transfected HeLa cells.

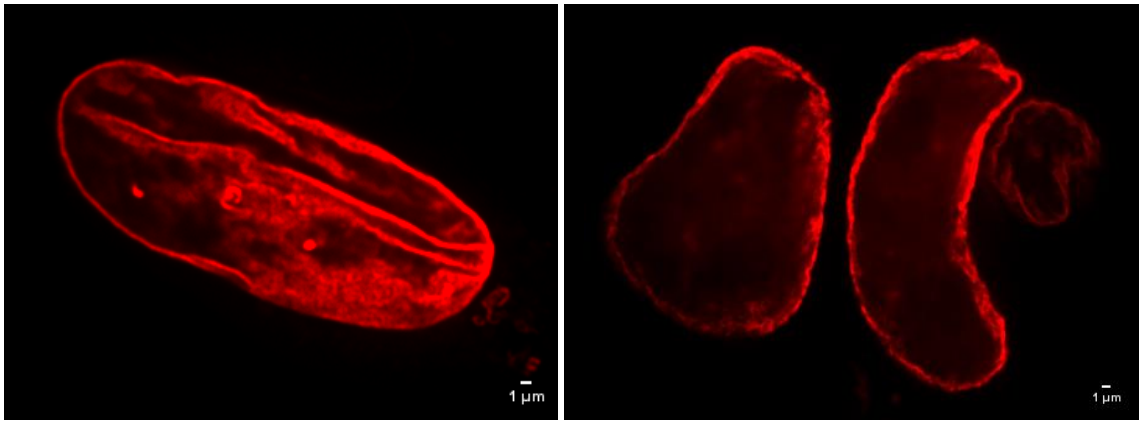

Fig. 36. Hela cells transiently transfected with the plasmid Lamin A-SNAP tag, and labelled with TMR. Confocal imaging, Obj 100x, NA 1.4.

A typical photo - oxidation experiment can be performed in 3 days (*133*). Briefly, day 1 is mainly to seed the cells in opportune petri dish with grid (e.g., MatTek). This

procedure allows finding the area or cell where the DAB photo-oxidation was performed (Fig. 37, A).

During day 2, the central bleaching experiment takes place, including fluorescence microscopy (Fig. 37, B and C), fixation of samples, DAB pre-incubation steps, and TMR bleaching. Next, post-fixation, dehydration, and finally embedding in resin were performed.

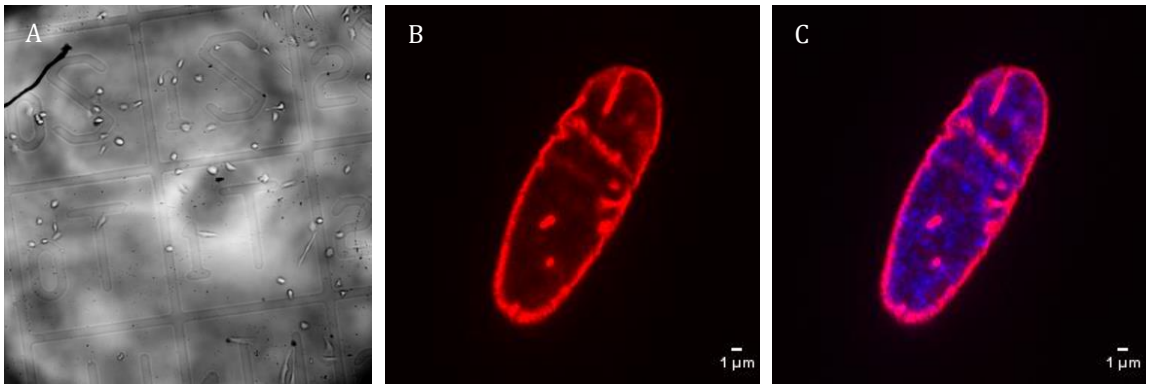

Fig. 37. The figure shows the petri dish with grid used to perform a CLEM experiment. Brightfield imaging, Obj 20x, NA 0.7. (A). From the labeled live sample, a cell was selected and acquired using an Obj 100x, NA 1.4. Live sample labeled with TMR (B) and Hoechst (C), Spinning Disk confocal imaging.

Day 3 includes the removal of the bottom glass from samples, ultrathin sectioning and EM evaluation (Fig. 38).

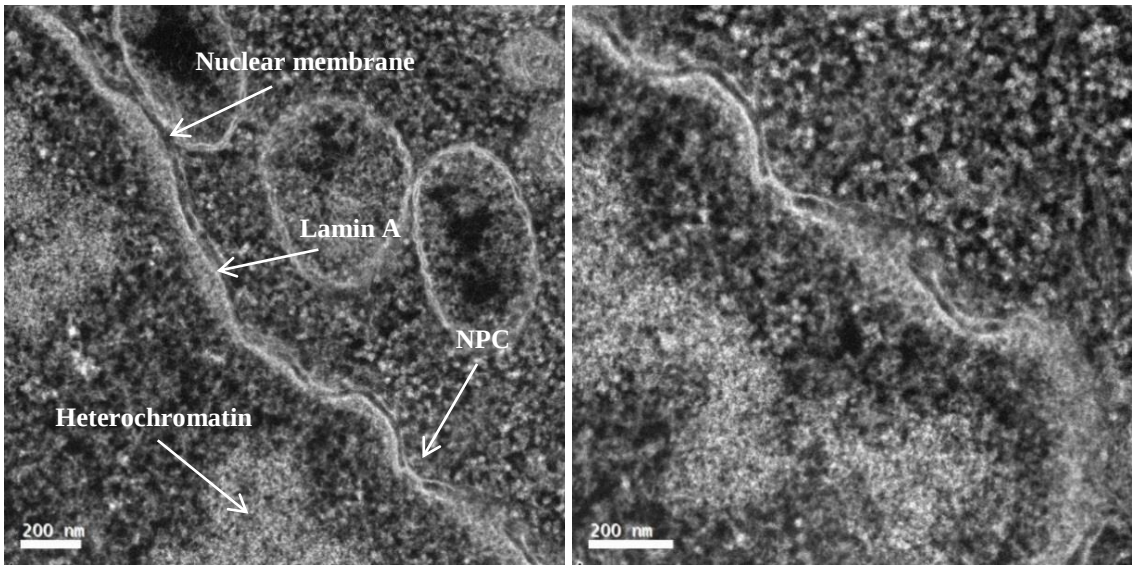

Fig. 38. Particular of the peripheral cellular nucleus. STEM imaging of TMR labelled sample. The heterochromatic region, the NPCs and the nuclear membrane have a good ultrastructural preservation. In addition, an electron dense region close to the nuclear membrane was observed, probably attributable to lamin A.

I obtained an acceptable ultrastructural preservation of the sample, and a significant DAB precipitation in the nuclear lamins region (below the nuclear membrane, STEM imaging; electron dense region in white) (Fig. 38). Unfortunately, the difficulty to improve the resolution in that region is probably attributable to the thin structure labelled and the rapid diffusion of the reactive oxygen radicals, which generate a diffuse cloud under the nuclear membrane. It is possible to notice the electron dense heterochromatin regions localized at the nuclear periphery, and the nuclear membrane discontinuity, attributable to the presence of nuclear pore complex.

6.3 ExM

The diffuse cloud obtained using the DAB polymerization process led me to investigate the NE using another super resolution technique. ExM can be a good compromise, in particular for crowded environment like nucleus. In this part of my research project, I will introduce the protocol used to combine ExM with STED nanoscopy (ExSTED), using samples labelled for tubulin.

However, it is extremely important to analyze quantitatively the isotropy of the expansion process at different scale and magnitude. To investigate the hydrogel characteristics, my attention is focused on nuclear pore complex (NPC, Fig. 18) a preserved structure not resolved using the conventional optical microscopy. Using NPC is possible to characterize and quantify precisely the expansion process and evaluate the compatibility of this method for nuclear structure.

6.3.1 Combination between ExM and STED nanoscopy

Chozinsky and colleagues developed a variant of ExM in which the sample is labelled before the expansion with conventional antibodies (Fig. 32). After gelation, the sample is homogenized using a proteinase K (*30*). We adapted the STED labelling protocol for the expanded tubulin in order to perform ExSTED (*7*). The labelling density plays a critical role in this method. For this reason, indirect immunofluorescent and high concentration of secondary antibodies (1:200) were mandatory. Initially, one colour ExSTED was developed and optimized at the intermediate expansion factor, using a commercial STED microscope. Fig. 39 shows the comparison between Pre-Ex, Post-Ex and ExSTED of HeLa cells labelled for α-

tubulin. The resulting final expansion of about 2.8 folds was calculated by overlapping and rescaling the confocal images of the same cells before and after expansion (*7*). The fluorescent dye used in this experiment was Alexa Fluor 488, because characterized by high photostability and retention to the gel polymerization.

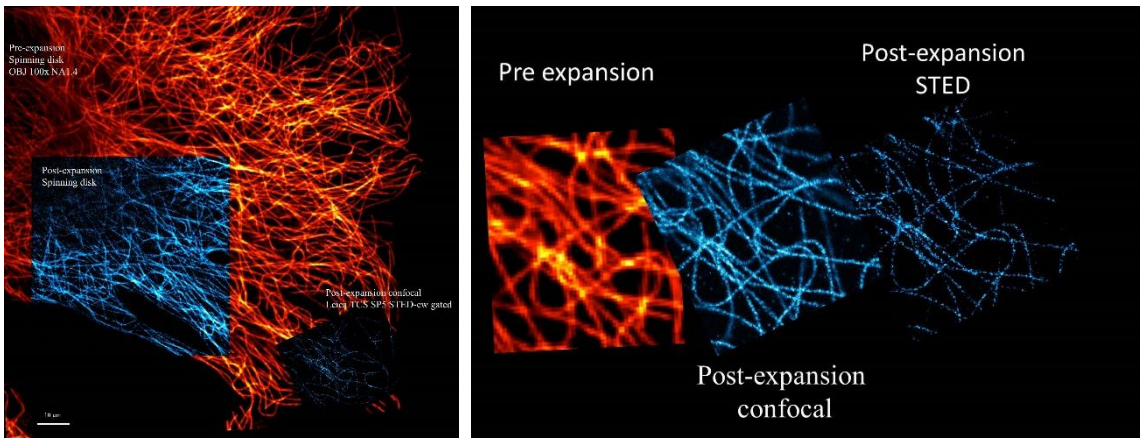

Fig. 39. The images show HeLa cells where α-tubulin is stained with Alexa 488 at different expansion steps. Exc 488 nm, STED line 592 nm, Gating 1.5ns, Obj 100x, NA 1.4 (Leica TCS SP5 STED-CW gated, Leica-Microsystems, Mannheim, Germany).

Succesively, a final expansion of about 4.5 times was achieved to perform 2-colours ExSTED (Fig. 40)

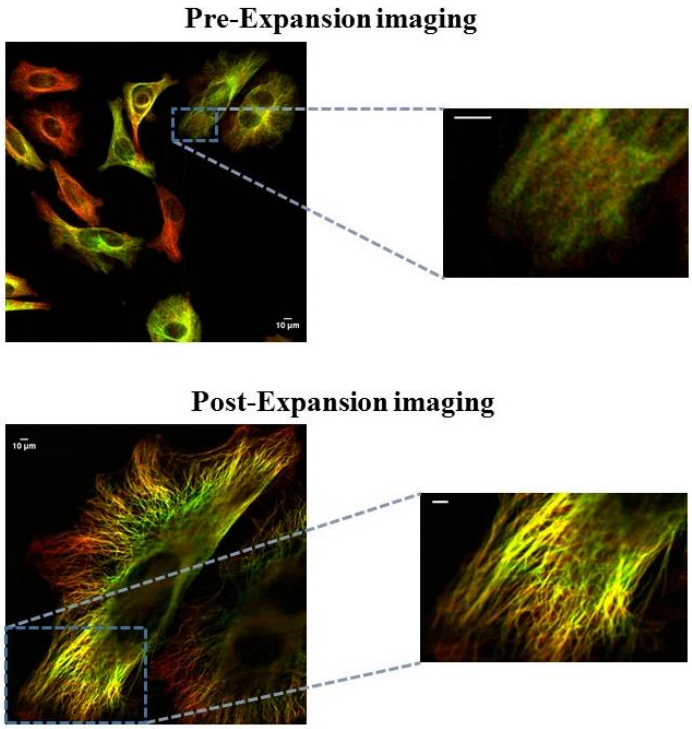

Fig. 40. Pre-expansion and post-expansion images acquired by confocal spinning disk (Nikon eclipse Ti coupled with Andor Revolution XD). The images show HeLa cells where α-tubulin

is stained with Atto 647N (exc 640 nm, in green) and β-tubulin with Atto 590 (exc 561 nm, in red). Scan size is 512 x 512 pixels, objective 20X NA 0.75, scale bar 10 μm. Expansion factor of about 4.5 folds.

α- and β-tubulin were labelled with Atto 647N and Atto 590, respectively. Using ExSTED, the two subunits are clearly distinguishable (Fig. 41, B), whereas, in the ExM confocal image (Fig. 41, A), the two signals are overlapped.

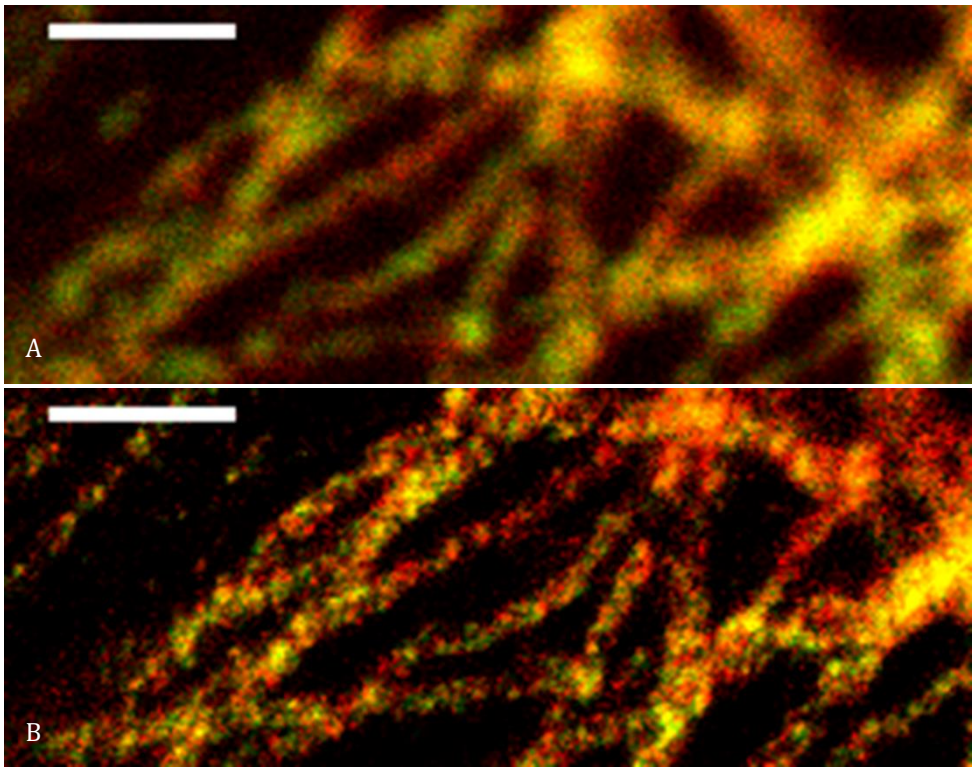

Fig. 41. Confocal (A) and STED (B) imaging of HeLa cells where α-tubulin is stained with Atto 647N (exc 640 nm, in green) and β-tubulin with Atto 590 (exc 561 nm, in red). Post-expansion imaging (4.8X expansion). STED line 745 nm, objective 100X, NA 1.4. Scale bar 0.42 μm (2/4.8 μm).

Using ExM, a wide range of samples has been successfully expanded and imaged. In particular, the neuroscience field has the major applicability. However, we do not know what happens quantitatively at the nanoscale level. Thanks to the resolution achievable, ExSTED can help us to answer at this question.

6.3.2 Quantification of the expansion factor and its isotropy using nuclear pore complex

Our goal is to investigate and compare the expansion factor (EF) at different spatial scales. The Fig. 18 shows a scheme of what we can measure before and after

expansion. At the millimeter scale, we can measure the gel size (Fig.18, A and D), at micrometer scale, we can measure the distances between nuclei (Fig. 1 B and E) and NPCs (Fig. 18, C and F) and finally, at the nanoscale, we can measure size and shape descriptors of the NPCs (Fig. 18, C and F). The well-preserved structure of the NPC makes the calculation of the expansion factor and the distortion at the nanoscale easier, because does not require to map the same NPC before and after expansion. I tested many antibodies against different NPC subunits, to be sure to visualize the ring-like structure using STED nanoscopy. Nup107, Nup133, GP210 and Nup153 were the antibodies commercially available tested in these experiments. These subunits are the principal components of the channels in the nuclear membrane. Although I tested several protocols, the first three antibodies used did not allow visualizing the ring-like structures of the pore using STED nanoscopy. Fig. 42 and 43 show some labelling difficulties that I encountered by labelling Nup133 and Nup107 subunits. Probably this is ascribable to the low affinity and specificity of the antibodies against these subunits.

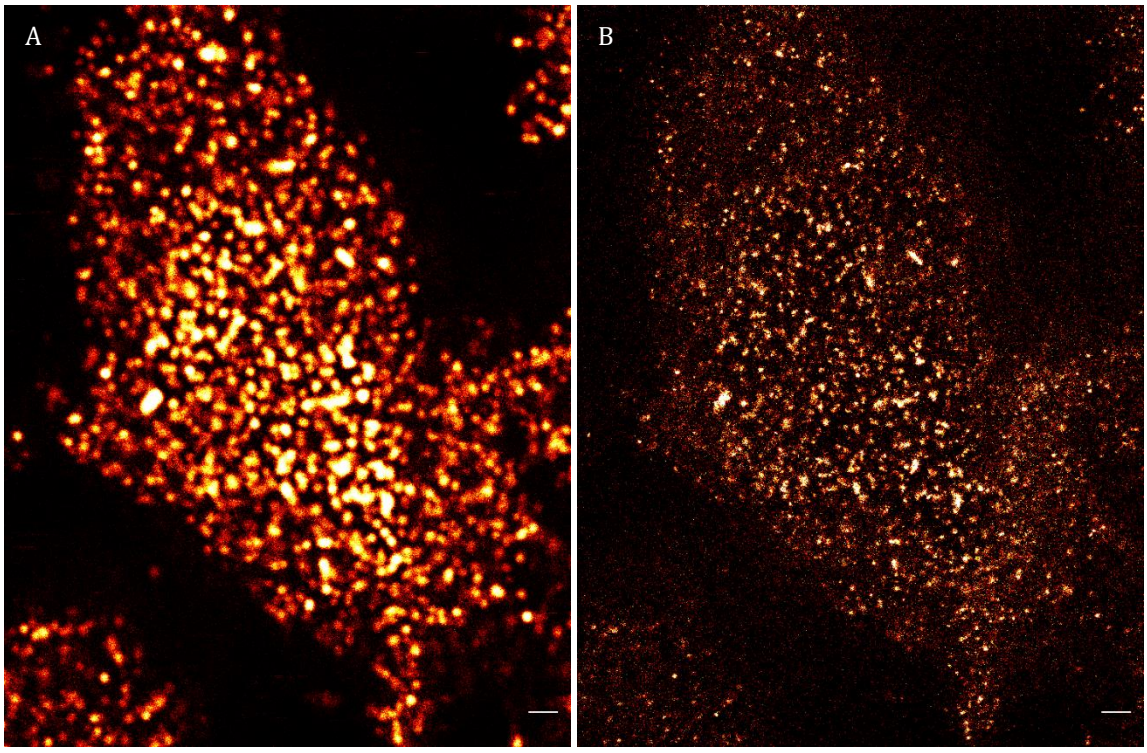

Fig. 42. The images show Hos cells labelled with Nup133 with Alexa488. The images are characterized by aspecific labelling in the cytoplasm. In addition to the background, it was not possible to image the ringlike structure of the pores by using STED nanoscopy (B). Scale bar 1 μm. Obj 100x, NA 1.4.

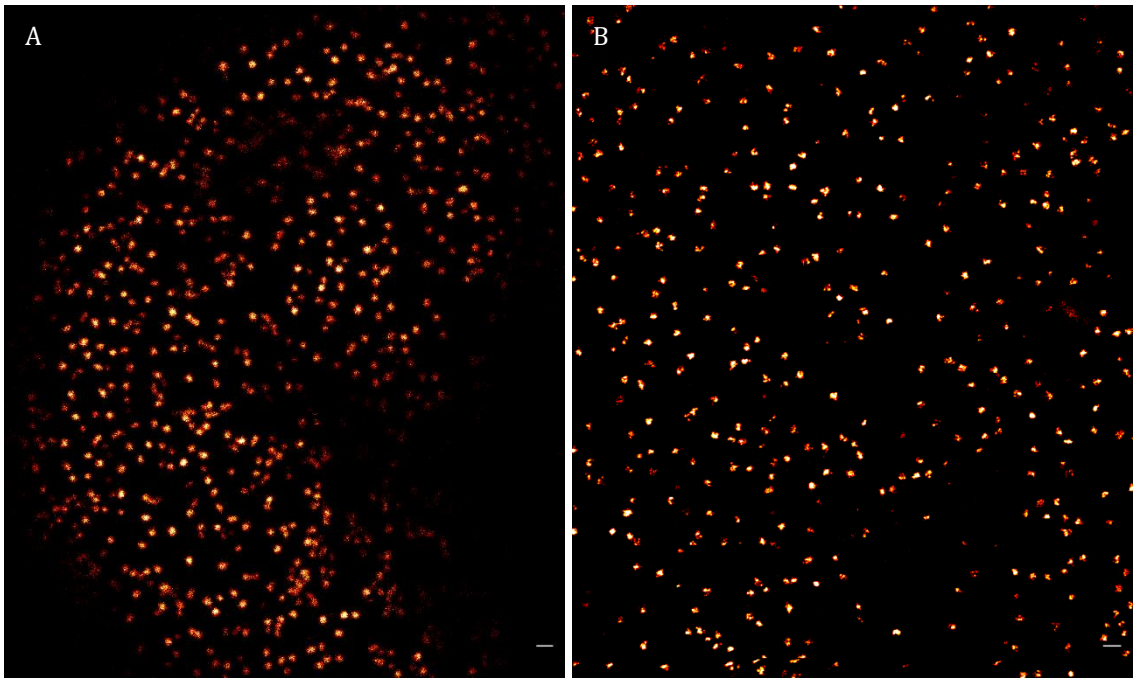

Fig 43. The images show a Pre-ExSTED (A) and Post-ExSTED (B) samples labelled for Nup107 with Alexa488. These images are characterized by low background and high signal to noise ratio, but, unluckily, it was extremely difficult to image the ring-like structures. This is probably due to the low affinity and the steric effects of the antibodies used against this subunit. Scale bar 1 μm for pre-ex image and 0.25 μm for post-ex image. Obj 100x, NA 1.4.

After labelling optimization, I noted that the Nup153 subunit matched perfectly for these experiments (Fig. 44, A and B), because the channel was resolved using the super-resolution techniques. This subunit is localized on the "nuclear basket", a high ordered structure localized on the nucleoplasmic side and composed by eight filaments associated to the channel. Indeed, Walther et al reported a precise localization of Nup153 at the base of the nuclear basket by immunogold labeling, with a distance from the centre of the channel of 47.0 $\pm$ 8.8 nm (*144*).

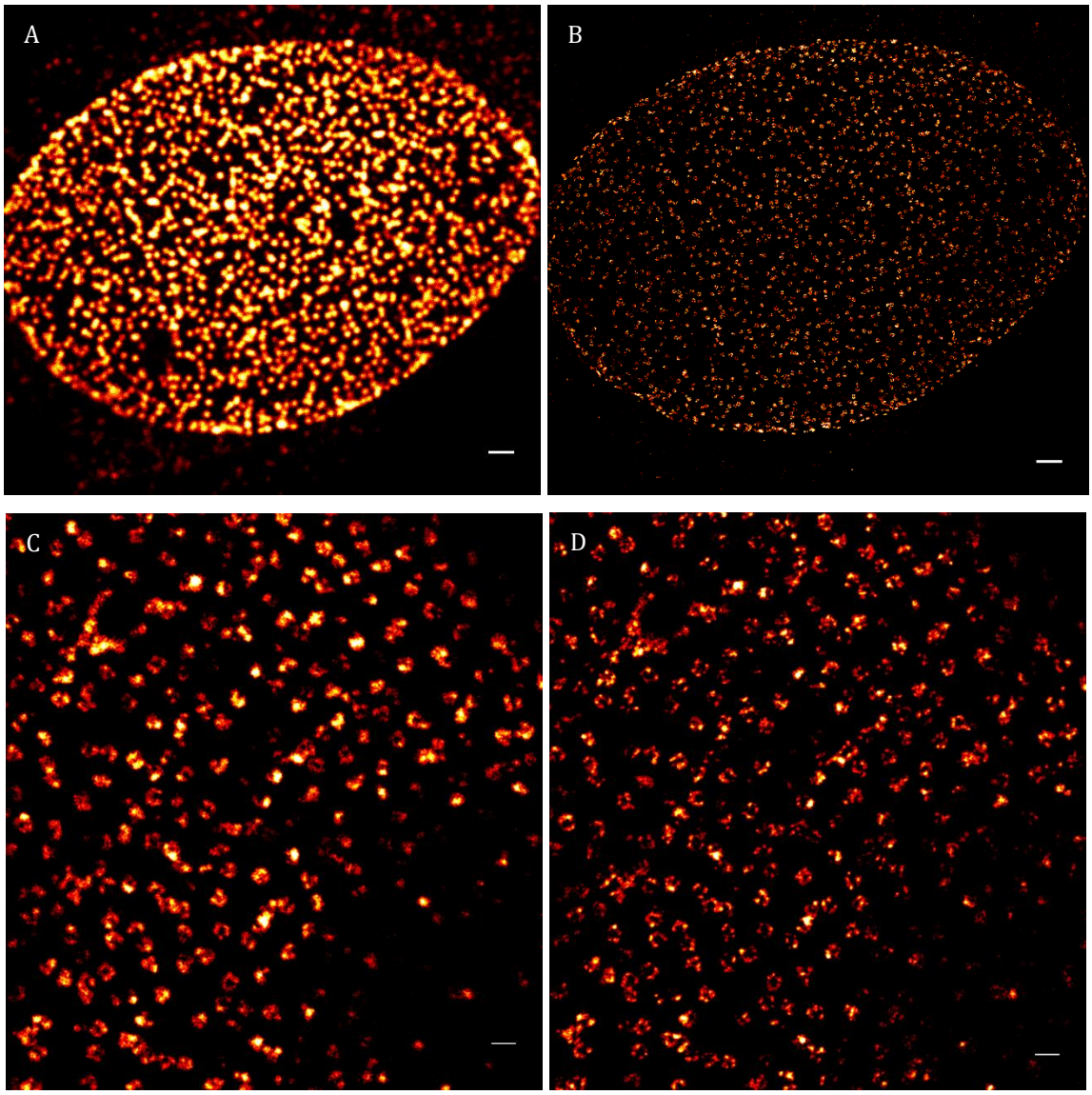

Fig. 44. Entire nucleus of Hos cells labelled for Nup153 with Alexa488. (A) Confocal imaging and (B) STED imaging. Using STED nanoscopy the ring-like structures were visualized labelling the Nup153 subunit. Scale bar 1µm. Particular of expanded nuclei of Hos cells acquired using confocal (C) and STED nanoscopy (D). Using ExM, the ring-like structures were imaged using a confocal microscope. Scale bar 0.25 µm. Obj 100x, NA 1.4.

In this work, we monitor three check points in the expansion process: after gelation (Fig. 45, A), after digestion (Fig. 45, D), and after dialysis in MilliQ water (Fig. 45, G). Although the expansion starts already after digestion, the expansion process reaches its maximum - about 5-fold – only at the last step. An advantage of using a STED microscope is that we can easily tune the optical resolution, for instance by changing the temporal gating and/or the depletion power (*145*). Therefore, we can keep a constant overall resolution at different expansion levels. It immediately results in a

reduction of photo-bleaching: more expansion, less STED power, less photo-bleaching, better signal-to-noise ratio. However, it is worth noting that, in both ExM and STED, the number of fluorescent molecules is reduced by a factor that depends on the reduction of the effective observation volume.

In particular, in Fig. 45 we show an example of NPC imaging at the three check points. We compare Confocal and STED imaging. While confocal imaging on Pre-Ex sample shows a spotty image where the empty basket is not resolved and many NPCs appear to form large aggregates (Fig. 45, A), STED imaging before expansion (Fig. 45, B) and confocal imaging after expansion (Fig. 45, G) clearly show the ring shape of the NPCs at comparable resolution. The Post-Dig sample shows intermediate characteristics in terms of signal and resolution (Fig. 45, A to D) respect to the Pre- and Post-Ex specimens. However, we noticed a worse imaging quality than the other check points, maybe caused by the presence of the digestion buffer in the gel that could quench the fluorescence. At the maximum expansion, confocal microscopy allows observing the characteristic ring-like structure (Fig. 45, G). From a qualitative analysis, we can gather that expansion is isotropic. It confirms that ExM is an excellent tool to investigate molecular structures in any area of the cell. However, to see the single subunits, we need to use STED nanoscopy (Fig. 45, H).

It is worth noting that, in this case, where the sample is expanded, depletion power is much reduced respect to the Pre-Ex case (Fig. 45, B). It means that photo-bleaching is reduced and signal-to-noise ratio is improved, while imaging at unprecedented resolution. Therefore, different EF and the possibility to tune the optical resolution play an important role in the final resolution achievable.

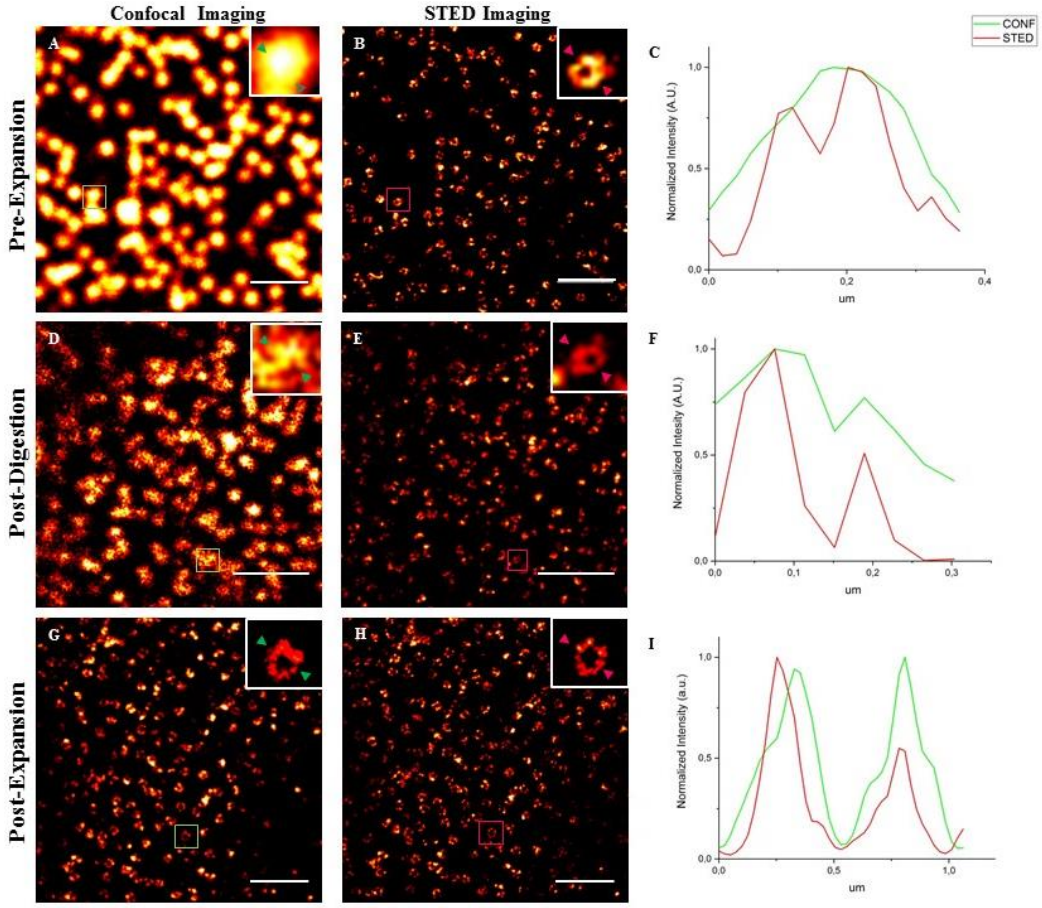

Fig. 45. NPCs visualized at various expansion factors and optical resolutions. Different conditions that can tune the final resolution in an ExM/STED experiment, including the expansion factor, the diameter of the pinhole, Gating and power of the STED beam are considered. (A) Pre-Ex Confocal Imaging, excitation (Exc) at the sample 13.3 µW; (B) Pre-Ex STED Imaging, STED power at the sample 72.2 mW, Gating 2-9.5 ns, Pinhole 0.6 AU. Scale bar Pre-Ex: 1 um; (D) Post-Dig Confocal Imaging, Exc at sample 13.3 µW; (E). Post-Dig STED Imaging, STED power at the sample 41 mW, Gating 1.5-9.5 ns, Pinhole 0.6 AU. EF ~2x, scale bar; (G) Post-Ex Confocal Imaging, Exc at the sample 13.3 µW; (H) Post-Ex STED Imaging, STED power at the sample 27 mW, Gating 1-9.5 ns, Pinhole 1 AU. EF ~4x, scale bar: 1 µm; (C, F, I) Line profiles of selected NPCs.

The ring-like structure of the NPC becomes clearly visible at different expansion folds and confocal resolution in expanded sample (Fig. 45, G). However, only using ExSTED it is possible to resolve finer details and distinguish single Nup153 subunits (Fig. 45, H). We now aim to demonstrate the eightfold symmetry of Nup153 in the Post-Ex samples, by means of a quantitative analysis on ExSTED images of the NPCs. Collecting a large quantity of nuclear pore images, we notice a wide sample heterogeneity (Fig. 46, A). The imperfect labelling of some structures, visible as open

rings, could be due to the digestion process or the staining heterogeneity. In fact, although we follow a labeling protocol for super-resolution imaging, gel polymerization and the digestion process may induce a final fragmented labeling for several Nup153 subunits and a loss of fluorescence signal (Fig. 46, B). To overcome these limitations, we use a statistical approach. From the ExSTED images acquired at the highest resolution, we isolate more than a hundred of single NPCs. For each NPC, we localize the Nup153 subunits and calculate their angular distance with respect to a subunit taken as reference (see Material and Methods). A multi-peaks fit of the cumulative histogram shows an angular difference among the subunits - 7 peaks respect to the reference subunit (imposed to 0°) - that is a multiple of 45 degrees (Fig. 46, C). This analysis thus confirms the eightfold symmetry and disposition of the subunits (Fig. 46, C). This result shows that STED enables a quantitative analysis at the nanoscale in expanded samples, allowing us to define single Nup153 subunits and confirm an eightfold symmetrical arrangement of the ring.

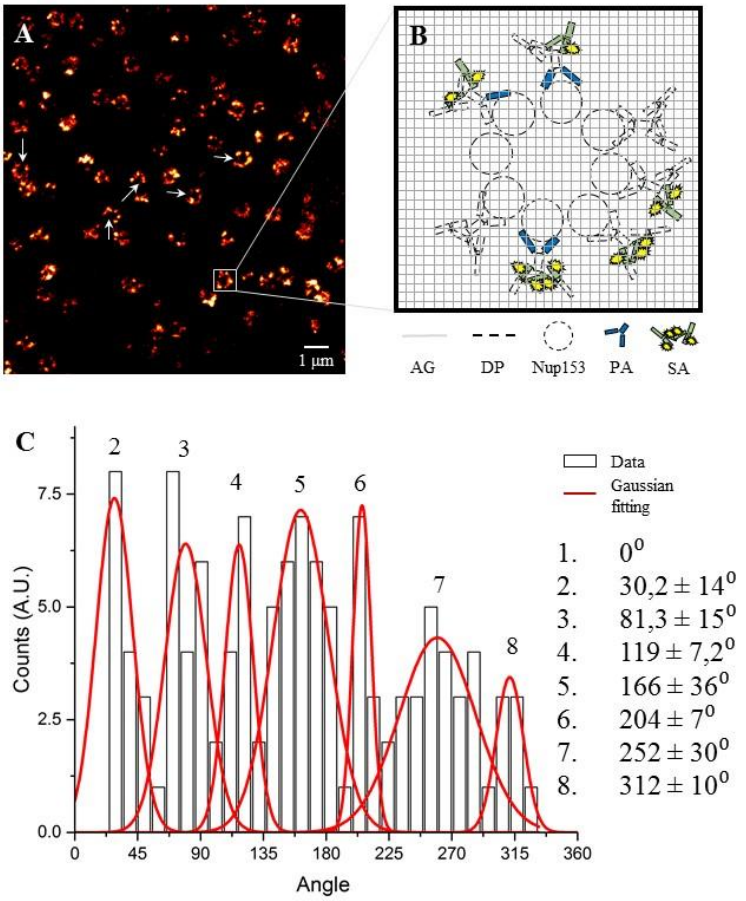

Fig. 46. After expansion, Nup153 preserves its octagonal symmetry. As a consequence of the antibodies used, the polymerization and the digestion process, we have a loss of fluorescent signal from the Nup153 subunits. It is evident in (A) (white arrows), in which the sample is

characterized by a wide heterogeneity. (B) shows a schematic illustration what happens in a single NPC labeled for Nup153 soaked in the gel after expansion. A way to overcome these limitations and clarify the octagonal structure of Nup153 after expansion is particle averaging. The histogram obtained (C) is characterized by 7 peaks, corresponding to the angular difference between the reference subunit (imposed to 0^0) and the other subunits. As shown, the angular difference among each subunits is a multiple of about 45 degree, demonstrating the pore octagonal symmetry of Nup153 subunit after expansion.
GA: Gel network; DG: Digested proteins; PA: Primary antibodies; SA: Secondary antibodies.

We quantify the EF at the nanoscale by measuring the radius of the pores. We image Nup153 by means of STED nanoscopy (Fig. 45, B) at the three check points, i.e., Pre-Ex, Post-Dig and Post-Ex. As in the previous analysis, we manually select more than hundred pores (Fig. 47, B, E and H) to quantify their radius and shape. In keeping with Walther et al (*144*), the measured radius of the ring labeled for Nup153 in the Pre-Ex sample is (55 ± 5) nm. Since the ratio of the size of the gel before and after digestion is 1.79 ± 0.05 (Fig. 47, D), we consider the Post-Dig sample as intermediate expansion. The measured pore radius in this sample is (96 ± 19) nm that corresponds to an $EF_{Post\text{-}Dig}$ of 1.8 ± 0.5 (Fig. 47, F).
In the last step of expansion method, consisting in MilliQ water dialysis, the obtained macroscopic expansion of the gel is 5 ± 0.1 (Fig. 47, G). The pore radius measures (234 ± 21) nm, which correspond to an $EF_{Post\text{-}Ex}$ of 4.3 ± 0.7 (Fig. 47, I).

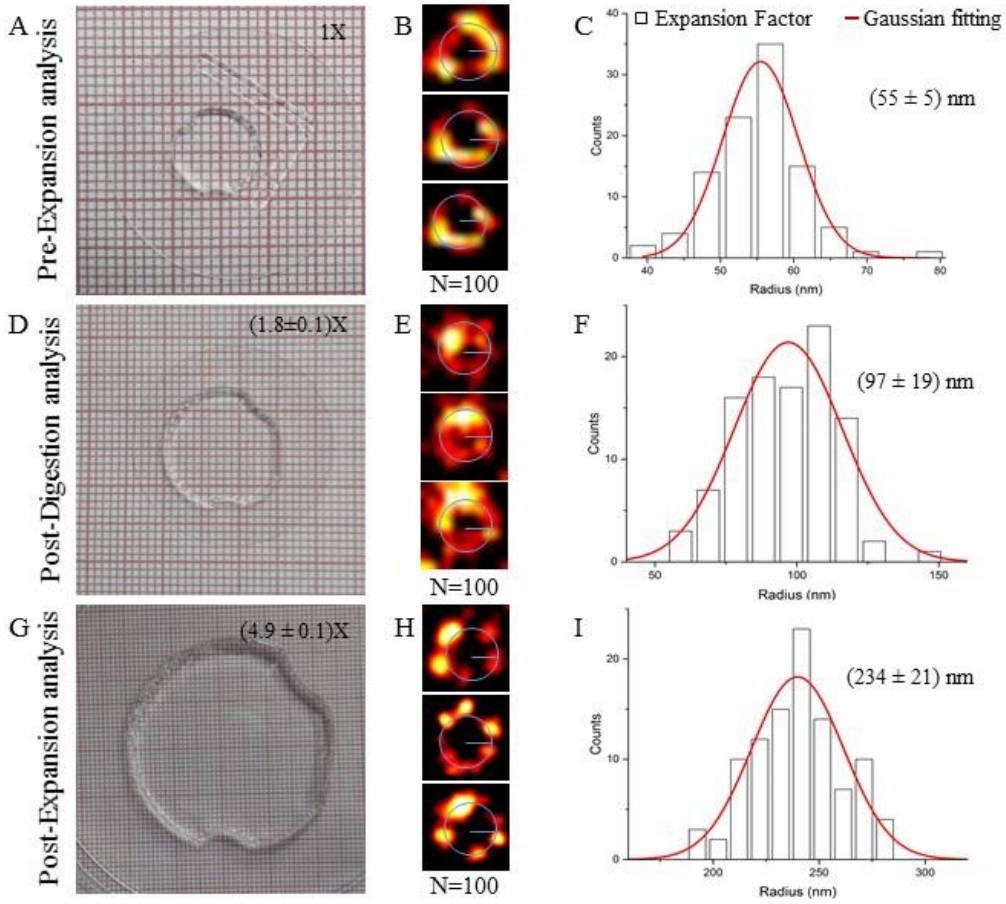

Fig. 47. Quantitative Pre-Ex, Post-Dig and Post-Ex/STED analysis. Macroscopic diameter of the Pre-, Post-Dig (EF = 1.79 ± 0.05) and Post-Ex (EF = 5 ± 0.1) hydrogel. (B, E, H) Examples of NPCs which are selected at different expansion time and imaged by STED Nanoscopy. (C, F, I) The histograms show the quantitative Pre-, Post-Dig and Post-Ex analysis of n=100 NPCs and the medium radius obtained. The EF of the pore radius obtained is 1.8 ± 0.5 after digestion (EFPost-Dig) and 4.3 ± 0.7 after expansion (EFPost-Ex). (L) shows the good correlation between the nanoscale and the macroscale EF.

Fig. 48 shows that the measures of expansion factors obtained on the gel, at the macroscale, and on the pores, at the nanoscale, are in good correlation.

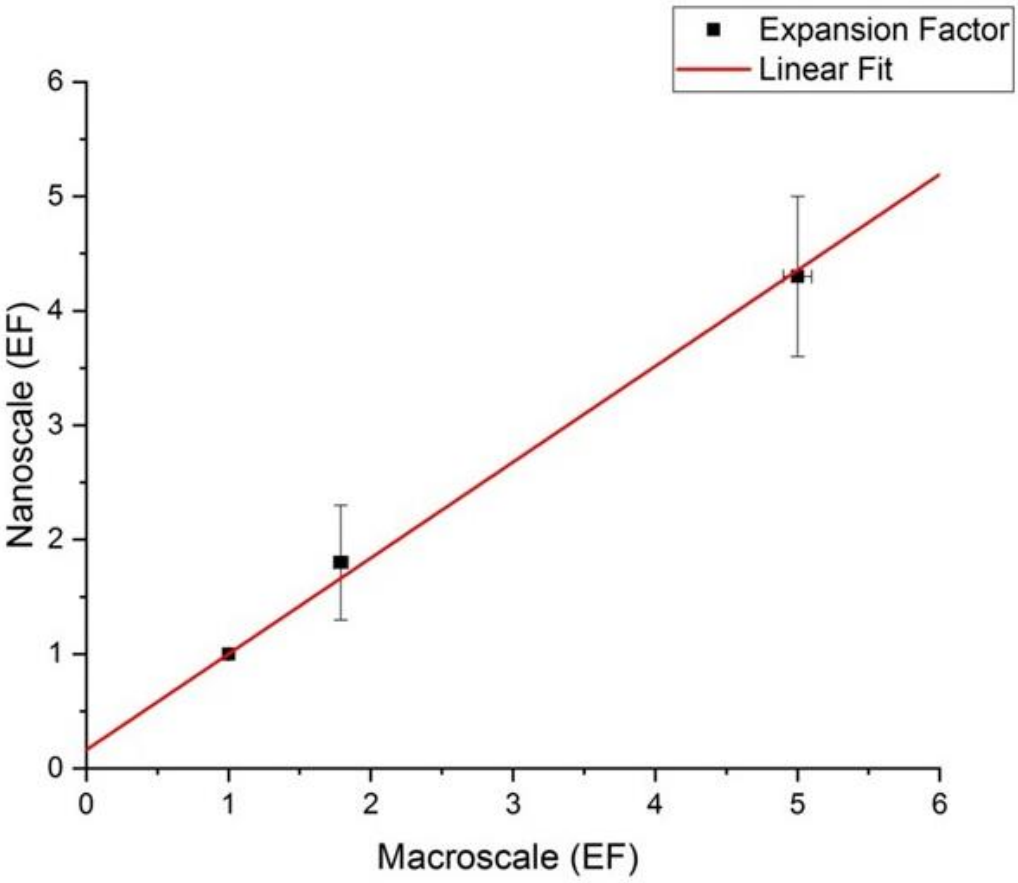

Fig. 48. Correlation between nanoscale and macroscale expansion.

Knowing the precise expansion factor at the nanoscale clarifies the final achievable resolution for the three different check points. The temporal gating (*146*), the depletion power and the pinhole size are modulated as a function of the expansion degree (Fig. 45), and permit us to tune the spatial resolution. The improvement of resolution provided by STED at any given experimental condition is calculated using the method reported in ref. (*145*). In the Pre-Ex sample, the optical conditions allow us obtaining a resolution of about 54 nm (Fig. 49, C). Obviously, an increase of the gel size corresponds to the reduction of the STED intensity, gating time and pinhole opening. In the Post-Dig sample, the estimated optical resolution of the STED microscope is 74 nm (Fig. 49, B), which combined with an expansion factor $EF_{Post\text{-}Dig}$= 1.8 yields a final effective resolution of 74 nm/$EF_{Post\text{-}Dig}$ = 41 nm. In the Post-Ex sample the resolution obtained is 100 nm, which combined with an expansion factor $EF_{Post\text{-}Ex}$= 4.3 yields a final effective resolution of 100 nm/ $EF_{Post\text{-}Ex}$ = 23 nm (Fig. 49, A).

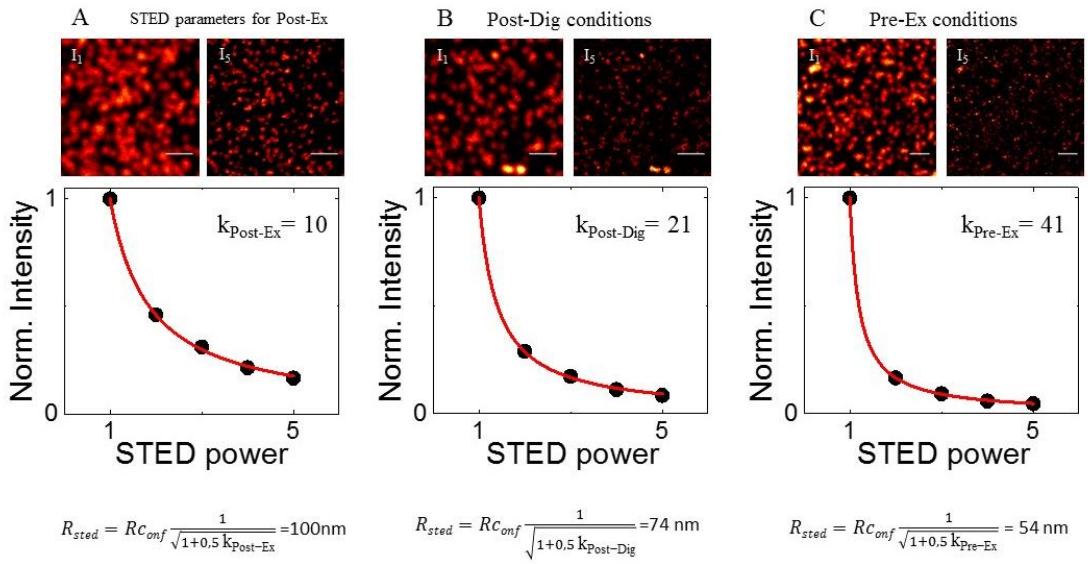

Fig. 49. Estimation of the resolution of the Pre-, Post-Dig and Post-Ex samples combined to STED. The depletion curves are obtained by acquiring linearly five frames by increasing the STED power, from the confocal (I1) to the STED maximum (I5). The conditions used are reported in the main text. The frames shown in Fig. A, B and C are acquired on a Pre-Ex sample, corresponding to a maximum of the STED power of 27 mW, 41 mW and 72.2 mW, respectively. From the average depletion curves we extracted a k parameter necessary to calculate the improvement of the resolution of the different check points. Approximating the confocal resolution (Rconf) of about 250 nm and dividing for the nanoscale expansion factor, we obtain a final resolution (Rf) of 23 nm, 41 nm and 54 nm in the Post-ex, Post-Dig and Pre-Ex, respectively. Scale bar 1 µm.

Finally, we measure the distance between pores localized on the same nucleus and on nuclei of different cells. Since it requires imaging the same cells before and after the expansion (Fig. 50), this procedure is remarkably demanding in terms of time and light exposure. For this reason, we skip the Post-Dig samples in this analysis. The Pre- and Post-Ex stitched confocal images are rescaled by affine registration (Fig. 50 and 51). These measurements are performed mapping eight different cells labelled for NPC and tubulin (Fig. 50).

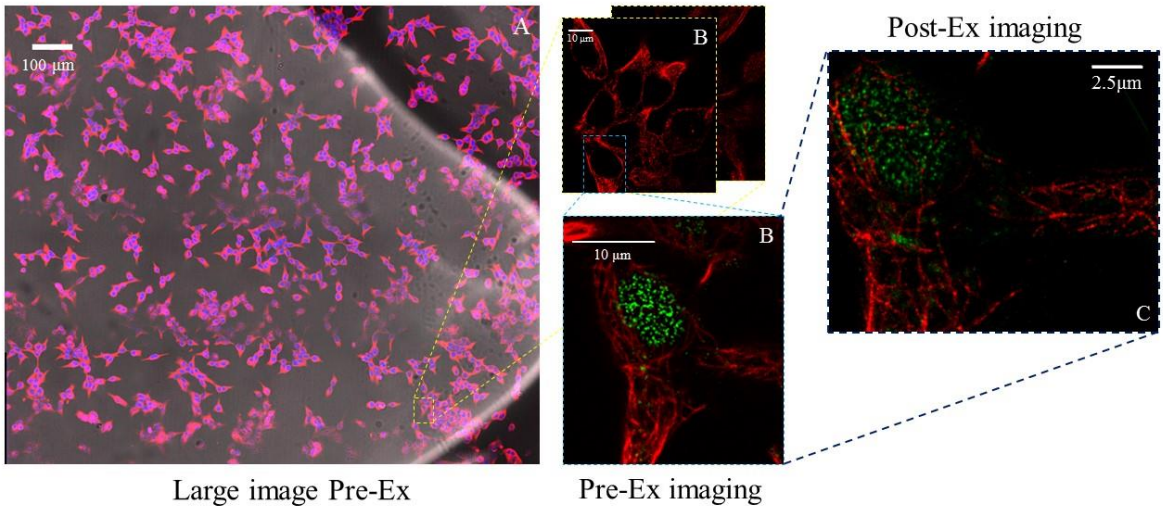

Fig. 50. Mapping method of the soaked sample in the hydrogel for microscale analysis. The expansion factor at the microscale level and the distortion are measured by overlapping and rescaling the confocal images of the same cell before and after expansion. In this way, we analyse the right distribution of NPCs at the microscale level. The expansion factor is calculated by ratio of the Post-Ex and Pre- pixel size in confocal images; these measurements are performed several times on each sample (8 times). The geometric shape of the hydrogel, α-tubulin and DNA labelling permit to map the same cell before and after expansion. (A) shows a large image using Spinning Disk. After mapping, a specific area is selected and imaged using confocal microscope (B). After expansion, the same cells are imaged using a confocal microscope (C).

After registration, using the pixel size ratio between Post- and Pre-Ex imaging, we measure an EF of 3.8 $\pm$ 0.1 from the intra-nuclei pore-to-pore distances and 4.3 $\pm$ 0.4 from the inter-nuclei pore-to-pore distances (Tab. 3). We note that, in this last group, the measured EF seems dependent on the cell localization. In these samples, we notice that Hek cells are clustered and divided by empty region of the hydrogel. The inter-nuclei expansion factor measured from cells in the same cell cluster is 3.9 $\pm$ 0.2, while the inter-nuclei expansion factor measured from cells not belonging to the same cell cluster is 4.6 $\pm$ 0.1, demonstrating a heterogeneous expansion at the microscale in different hydrogel regions.

Expansion Factor				
	Nanoscale	Microscale:		Macroscale
		Intra - nucleus	Inter - nuclei	
Post-digestion	**1.8 ± 0.5**	-	-	**1.79 ± 0.05**
Post-expansion	**4.3 ± 0.7**	**3.8± 0.1**	**4.3 ± 0.4**	**5.0 ± 0.1**

Tab. 3. Correlation between nano-, micro- and macroscale expansion. The table synthetize the expansion values obtained using the quantitative analysis at different EF and scale. For the microscale validation, we apply an affine registration on single cells nuclei and cellular clustered nuclei to determine the distance between the pores (intra- and inter-nuclei analysis). The data obtained correlate with the other expansion factors.

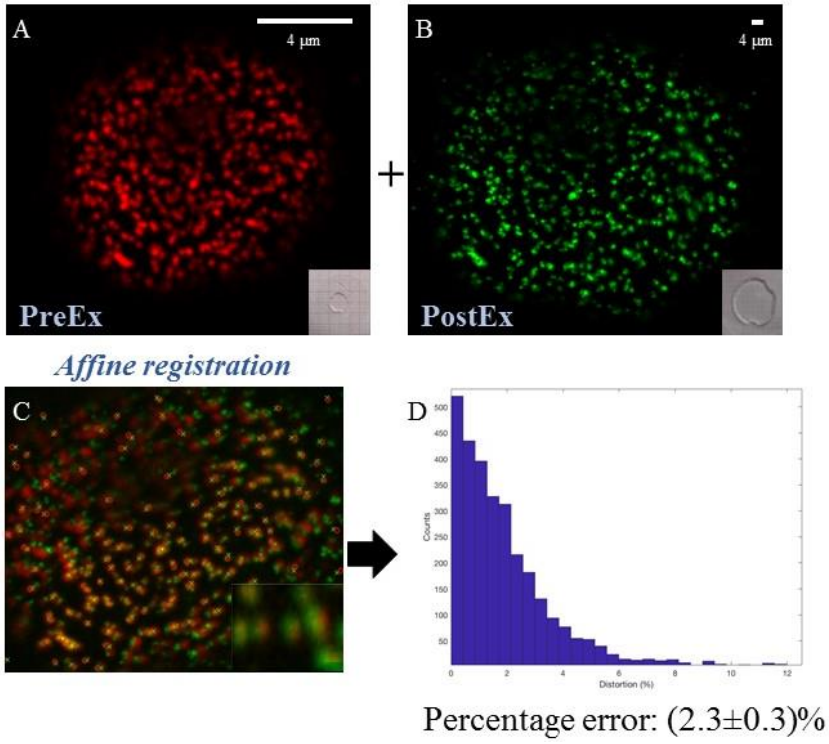

Fig. 51. Calculating of the expansion and distortion factor by affine registration. (A) and (B) show a confocal Pre- and Post-Ex imaging of the same nucleolus labelled for NPC with Nup153. (C) shows the affine registration between the two images using TurboReg (Fiji). This strategy allows us to obtain the expansion factor by pixel size ratio and the distortion error, calculating the distance pore to pore (red circle: Nup pre-expansion; green cross: Nup post-expansion).

After registration, we use the Fast 2D Peak Finder script (Version 1.12.0.0, Natan, 11 Oct 2013), which allows the maximum relative values to be found, corresponding to the NPCs of the Pre- and Post-Ex. The distance between pores and an estimation of the percentage error are calculated (D).

6.3.3 Nanoscale imaging of the Lamin A network

Next to the validation of ExM for nuclear structures by using NPC analysis, my attention was focused on nuclear lamins. Although Shimi et al characterized the supramolecular structures of lamin A, C, B1, and B2 in mouse embryo fibroblast nuclei (*147*), the structural organization of the proteins composing the lamina network is poorly defined.

The unsuccessfully attempt to visualize lamin A meshwork by CLEM is the principal reason that leads me to change approach. Obviously, to image the lamins using STED nanoscopy and ExM, the density of the labelling and the right choice of the fluorophore are critical aspects to consider. Since the secondary antibodies carry on more than one fluorophore, the indirect immunostaining remains the best option for a sufficient labelling density and high signal to noise ratio.

I investigated the meshwork of the wild type lamin A using different approaches. The comparison between confocal and STED of Hek cells labelled for lamin A with Alexa 488 are shown in Fig. 52:

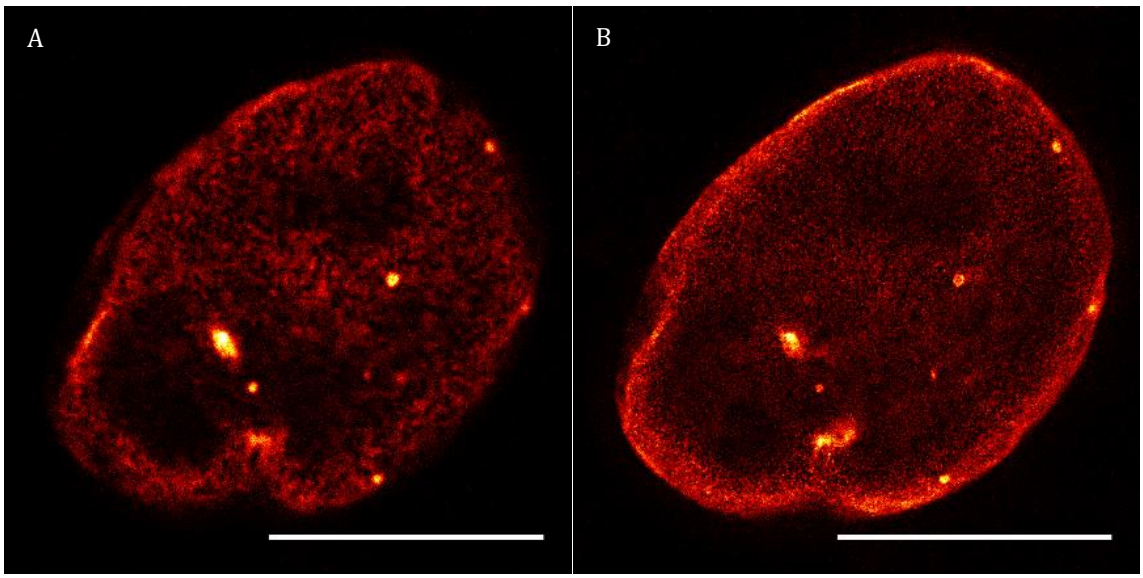

Fig. 52. HEK cells where Lamin A is stained with Alexa 488. A. Confocal imaging, Exc 488 nm, Obj 100x, NA 1.4. B. STED imaging, Exc 488nm, STED line 592 nm, Gating 1.5ns, Obj 100x, NA 1.4 (Leica TCS SP5 STED-CW gated, Leica-Microsystems, Mannheim, Germany). Scale bar 10 μm (*84*).

STED nanoscopy on labelled lamin A allows me revealing tube-like invaginations, termed nucleoplasmic reticulum (NR) (*148*), with a diameter of 100–500 nm (Fig. 53). The existence of such network of invaginations formed by the NR could provide sites that are capable of carrying out the NE functions deep within the nucleus.

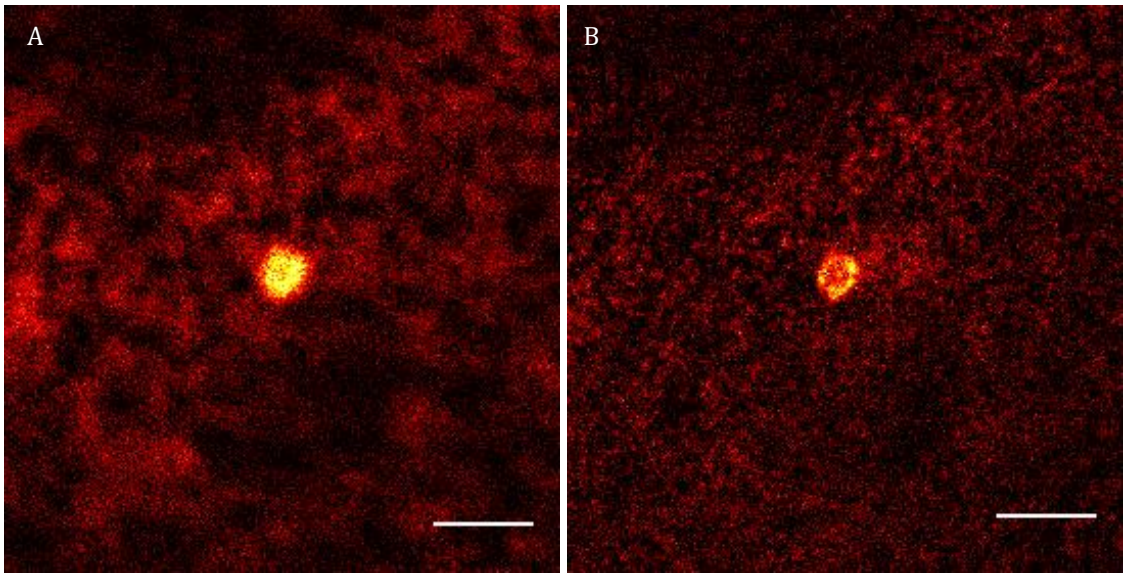

Fig. 53. Particular of the nucleoplasmic reticulum of the sample labelled for Lamin A imaged with confocal (A) and STED (B).

After optimization of the labelling protocol for STED nanoscopy, I used ExM to image the lamin A meshwork. As shown in Fig. 54, I obtained an appreciable expanded network of lamin A using a confocal microscope.

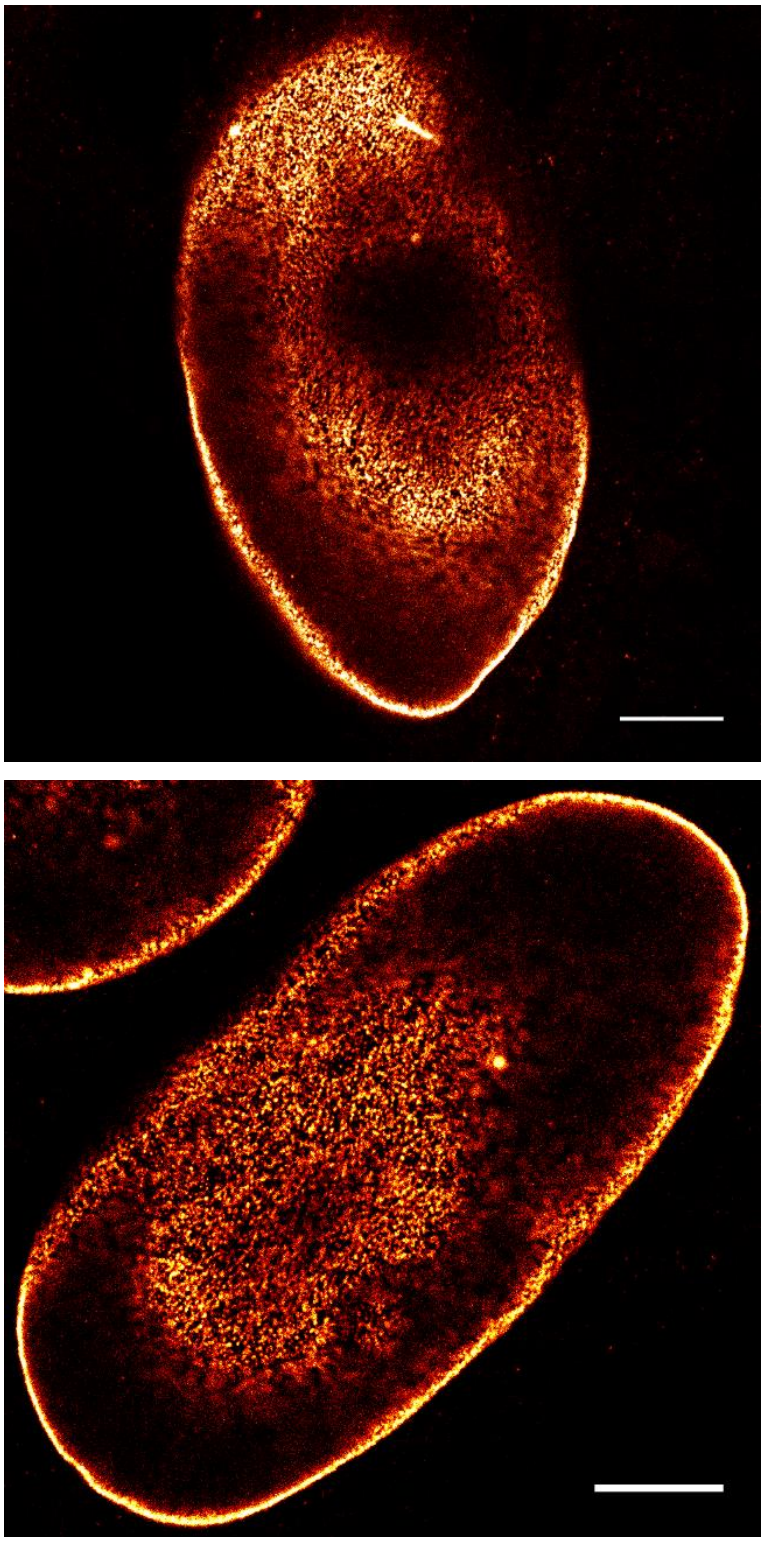

Fig. 54. Expanded HEK cells where Lamin A is stained with Alexa 488 (Nikon A1 Confocal Microscope), Obj 60x, NA 1.4, scale bar 10/4=2.5 μm (*84*).

However, STED nanoscopy depends on high laser power, representing a challenge for the acquisition of 3-dimensional stacks of cells. Such observation motives me to image 3D labelled structures using a conventional microscope combined with ExM.

Fig 55 shows a pre-expansion imaging Hek nuclei labelled for lamin A with Alexa 488:

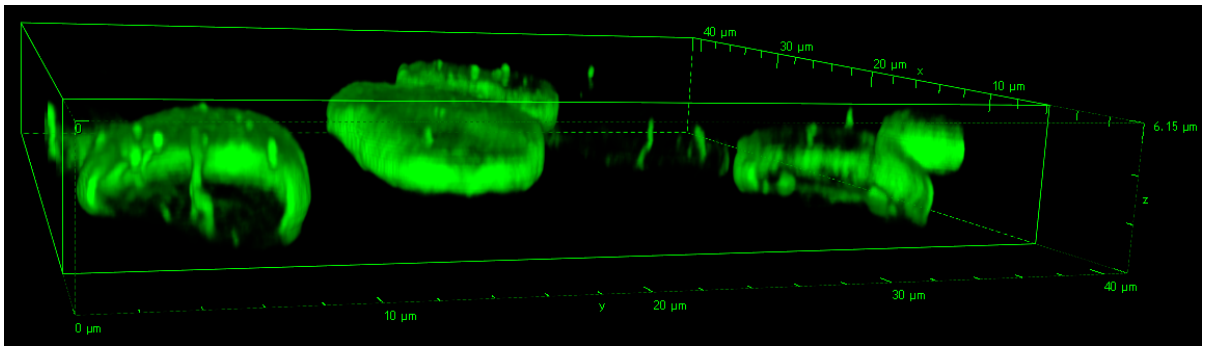

Fig. 55. Pre-expansion 3D imaging of Lamin A organization. Nikon A1 Confocal Microscope, Obj 60x, NA 1,4.

To obtain expanded 3D stacks of Hek cells (Fig. 56), it is extremely important to soak the hydrogel in a solution of 2% Agarose to immobilize it and avoid drift during the microscope acquisition.

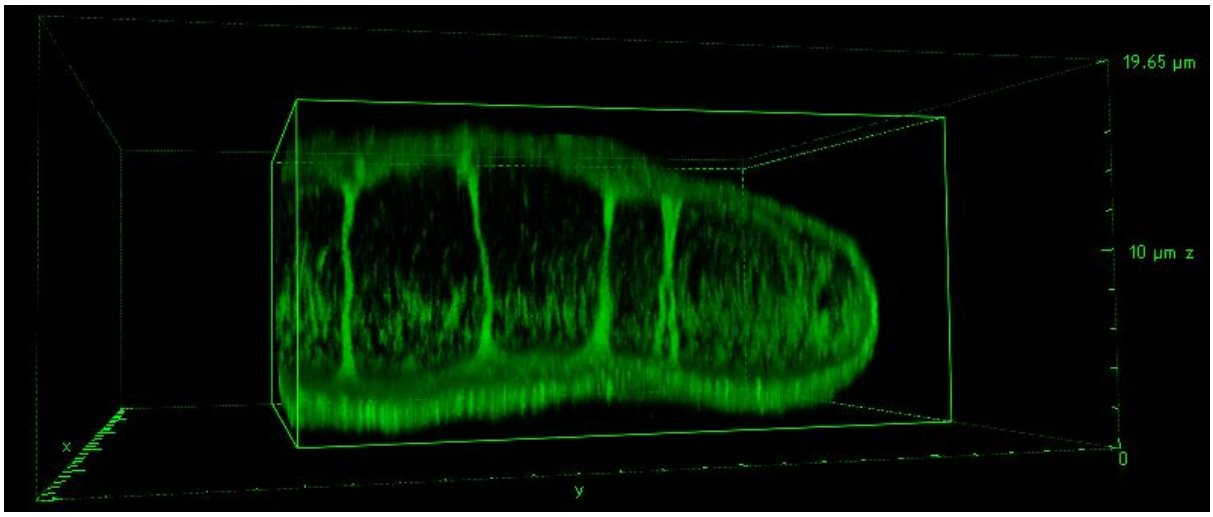

Fig. 56. Post-expansion 3D imaging of Lamin A organization. Nikon A1 Confocal Microscope, Obj 60x, NA 1,4 (*84*).

After, Hoechst was performed on expanded Hek cells labelled for lamin. This staining strategy can help me to decipher the chromatin – DNA characteristics around the nuclear invagination. As shown in Fig. 57, B, the high-density of the Hoechst staining associate with the NR suggest the presence of heterochromatic regions close to nucleoplasmic reticulum.

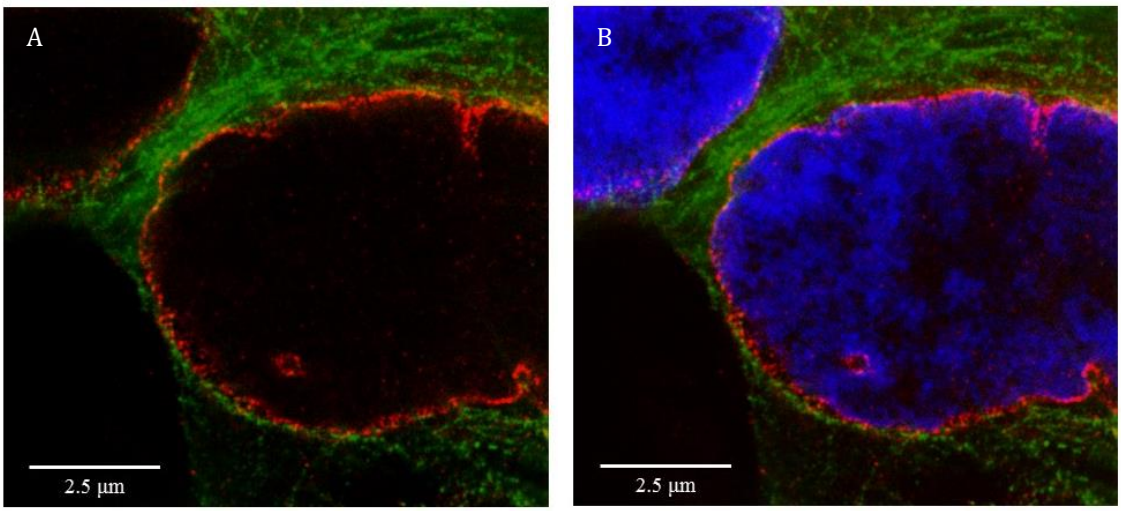

Fig. 57. Expanded Hek cells labelled for beta-tubulin with Atto590, Lamin with Atto647N (A) and Hoechst (B). Confocal imaging, Obj 60x, NA 1.4. Expansion factor of 4.5 folds.

As shown, the presence of the wild type lamin A generates a linear structure and circular shape of the nuclear membrane. In addition, using ExM was possible to resolve with more accuracy the physiological invagination of the nuclear envelope in 3D stack.

6.3.4 Nanoscale imaging of ΔLA50

The expression of wild type lamin A maintains the regular shape of the nuclei in mammalian cells. This observation comes from the phenotypic differences due to the expression of a mutated form, called Progerin or ΔLA50 (*96, 139*). ΔLA50 induces an alteration in the nuclear architecture and formation of the pathological blebs. This is due to the accumulation of the farnesylated protein in the NE. By transfection of the truncated form (without 50 aminoacids in the C-terminal) fused to gene reporter, we can visualize the nuclear alteration using a fluorescence microscopy. Fig. 58 shows Hek cells transfected with a plasmid encoding for ΔLA50-GFP and visualized using a confocal microscope. In this mode, the heterozygosity and the dominant genetic alteration are induced in normal cells. Obviously, the transfected sample is characterized by different expression level of ΔLA50-GFP, depending on the uptake of the plasmid DNA and the cell vitality.

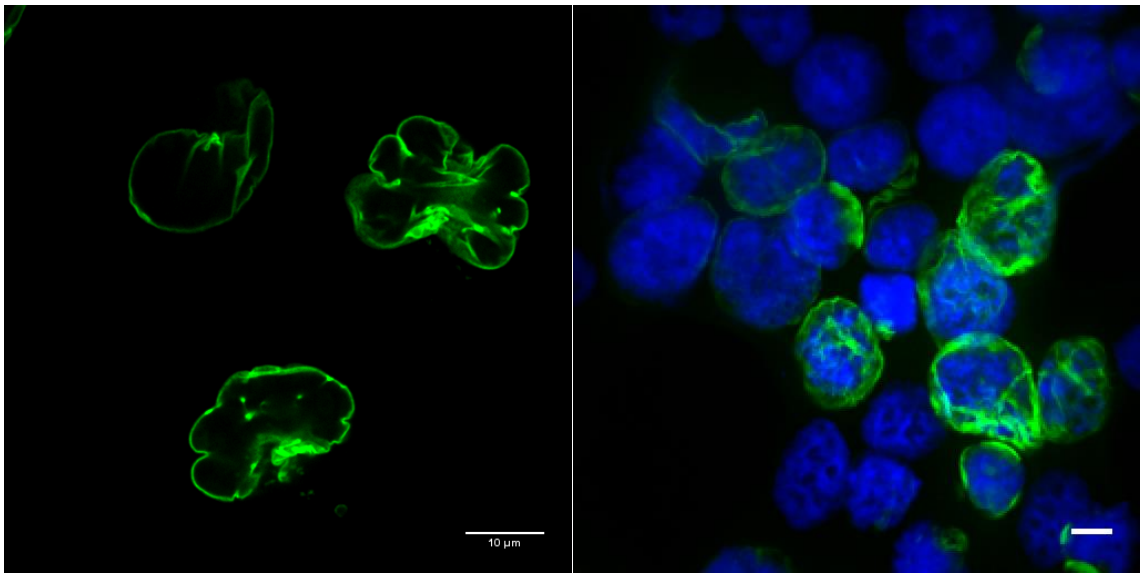

Fig. 58. HEK cells transfected with ΔLA50-GFP (A) and stained with Hoechst (B). Confocal imaging, Obj 60x, NA 1.4. Scale bar 10 µm.

In addition, the expression of ΔLA50 can cause alteration in the epigenetic state of normal and HGPS cells. Indeed, McClintock and colleagues demonstrated that normal fibroblasts accumulate ΔLA50 as a function of their age in culture, showing an alteration in the nuclear shape and architecture (*126*). Concurrently, they display a loss of heterochromatic marker, like methylated histone, responsible of the chromatin DNA compaction and gene silencing at the nuclear periphery.

The decrease of the heterochromatic marker in cells from older individual or in cells from patients with premature aging syndrome, demonstrates a misregulation of many genes that are silenced in young healthy.

Using Hek cell line expressing ΔLA50-GFP, we can examine changes in the epigenetic histone markers, such as histone H3 (di methyl K9), in function of the protein expression (Fig. 59).

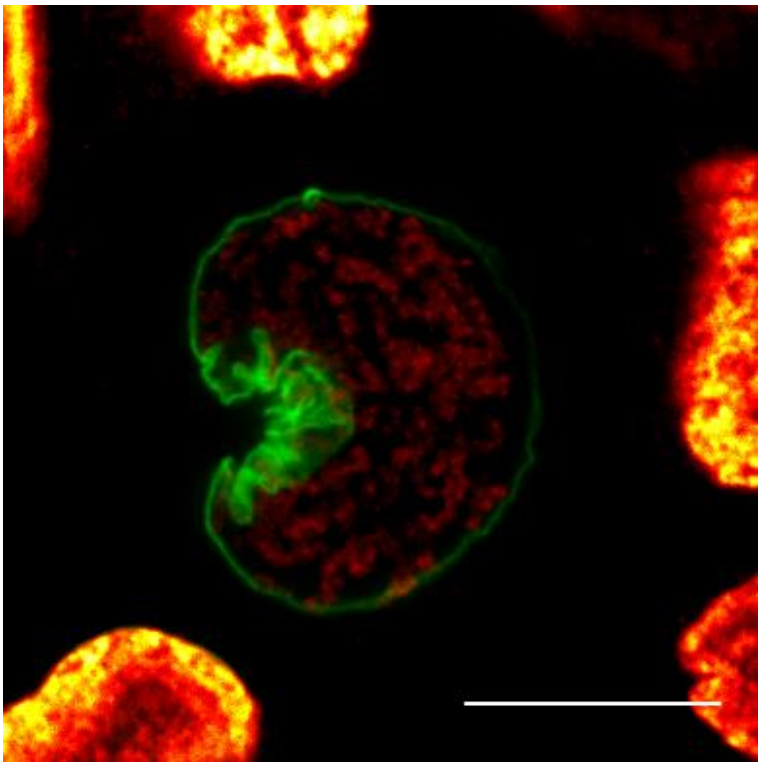

Fig. 59. HEK cells transfected with ΔLA50-GFP (green) and stained for Histone H3 (di-methyl K9) with Atto647N (red). Confocal Leica Microscope. Obj 100x, NA 1.4. Scale bar 10 µm.

After, I used ExM to image lobulated nuclei expressing ΔLA50-GFP. In this case, the digestion time is a critical aspect, necessary to preserve the fluorescence signal of GFP after expansion. Indeed, after fixation of the sample, the anchor groups (necessary for crosslinking to the hydrogel) were generated by using glutaraldehyde, with a maximum digestion time of 30 min (Fig. 60).

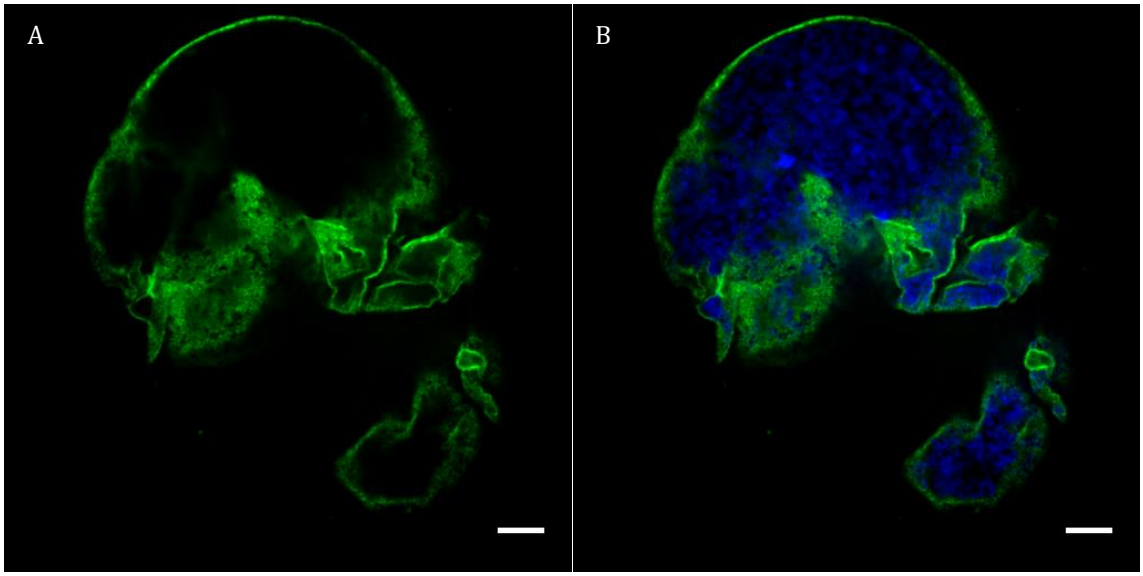

Fig. 60. Expanded HEK cells transfected for ΔLA50-GFP (A) and stained with Hoechst (B). Expansion factor ~ 4 times. Confocal Spinning Disk. Scan size is 512 x 512 pixels, objective 60x NA 1.4, scale bar 10/4=2.5 µm (*84*).

To obtain expanded 3D stacks of transfected Hek cells, I soaked the hydrogel in a solution of 2% Agarose to avoid drift during the microscope acquisition. The low fluorescence signal and photo-stability after expansion of GFP forced me to image the transfected sample by Spinning Disk confocal microscope (Fig. 61).

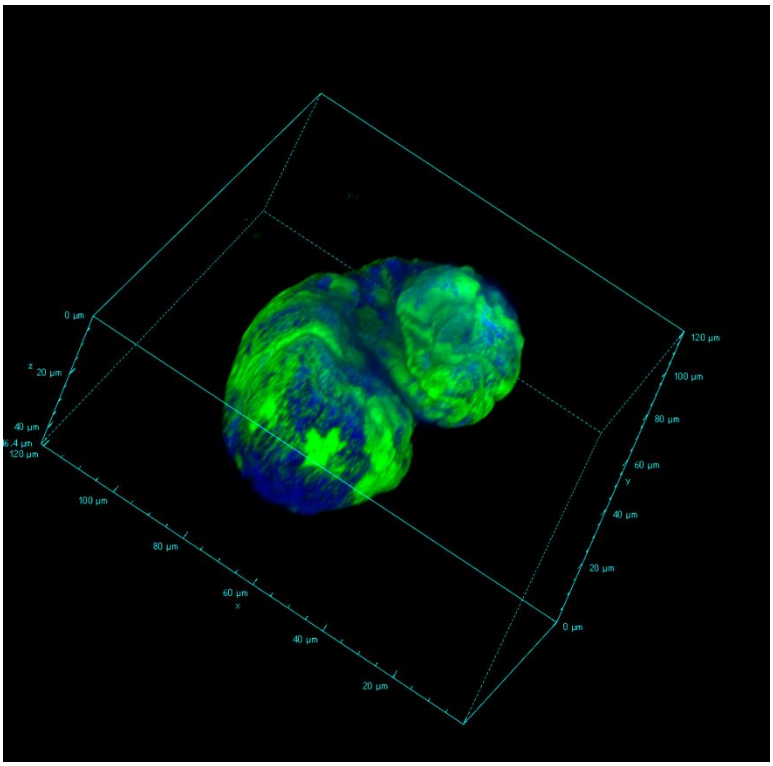

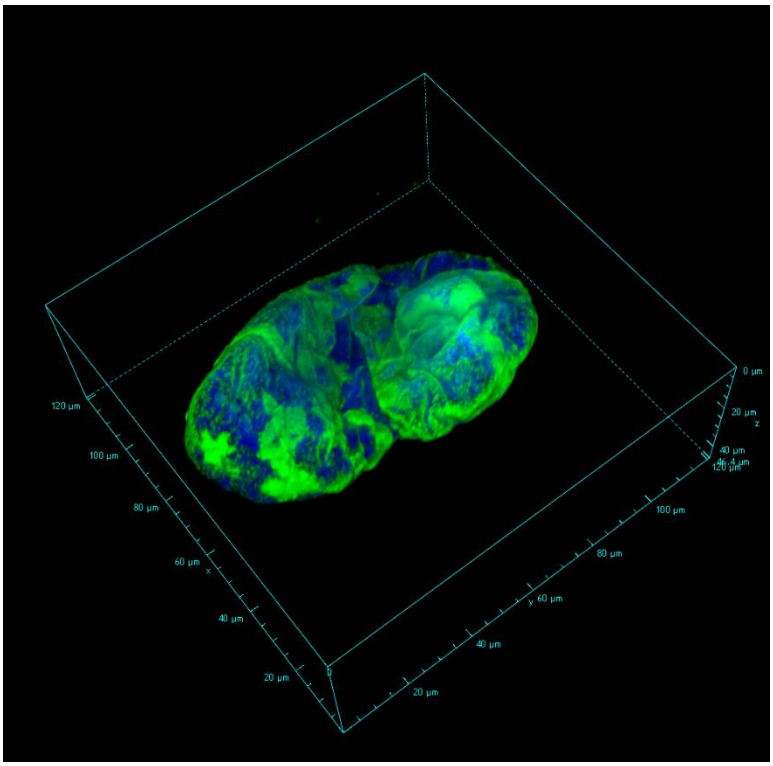

Fig. 61. Post-expansion 3D imaging of ΔLA50-GFP and the chromatin organization. Confocal Spinning Disk, Obj 60x, NA 1.4 (*84*).

7 Conclusions

The presence of irregularities in the nuclear structure and size (termed pleomorphism) associate with changes in the chromatin organization and distribution, are the characteristics in common for cancer and aged cells. Formation of pathological blebs, undulations and folds of the nuclear membrane occur in neoplastic process and often are phenotypic features observed for a right diagnosis of several medical conditions. These features are commonly used in the medical fields, for the cytological diagnosis using a fluorescence microscope. However, the molecular mechanisms involved in the genesis of nuclear irregularities are not clarified, resulting an open field for fluorescence microscopy. Obviously, to understand the main characters in this process could be an excellent strategy for the early diagnosis in cancer and aging related diseases.

In recent years, the NE has been found to play important roles in different cellular pathways. Although it is the principal determinant of the nuclear shape, NE also regulates the chromatin-DNA organization and the epigenetic state in the cells. During my Ph.D., I investigated two groups of proteins belonging to the NE: nuclear pore complex (NPC) and lamin A. NPC was used as biological reporter to verify the isotropy and precisely quantify the expansion for biological structures in correlation with the gel size. The possibility of the distortion of complex molecular assemblies due to the expansion process is a potential problem of this technique and it must be deeply investigated. We implemented a quantitative approach applying STED Nanoscopy on expanded samples, to verify the native arrangement of molecules embedded in the gel. Obviously, the optimization of the protocol to combine ExM with STED nanoscopy was mandatory. Primarily, it was necessary to compare our data with published electron microscopy studies to understand the localization and the radius of Nup153 in the NPC. I found only a few studies about this specific subunit, which are in keeping with our data. After expansion, the visualization of the ring-like structure using a confocal microscope was the first qualitative demonstration that the expansion was isotropic. After demonstrating the eightfold symmetry of Nup153 by the combination between particle averaging and ExM, we apply a quantitative analysis to measure the pore radius, verifying the distortion due to the gelation and expansion at the nanoscale level. This analysis confirms that the

relative error does not change in the pre- and post-expansion sample (9%). This shows that the pore size variability is due to the heterogeneity of the labelling for NPCs, and not to the distortion induced by gelation and expansion. In comparison, the post-digestion sample is characterized by a high error value (20%), probably attributable to incomplete and not isotropic expansion. These data are confirmed by the pre- and post-expansion pixel size ratio between pores belong to the same nucleus or to adjacent nuclei (microscale analysis, Tab. 3). Finally, I distinguish two different EF for neighboring cells at microscale level (Fig. 62). Our hypothesis to explain it is that the hydrogel without biological sample is characterized by higher expansion factor values (space between not connected cells, expansion factor of (4.6 $\pm$ 0.1), while the presence of chromatin DNA and/or the incomplete digestion in some cell clusters can cause resistance to the expansion ((3.9 $\pm$ 0.2), Fig. 62).

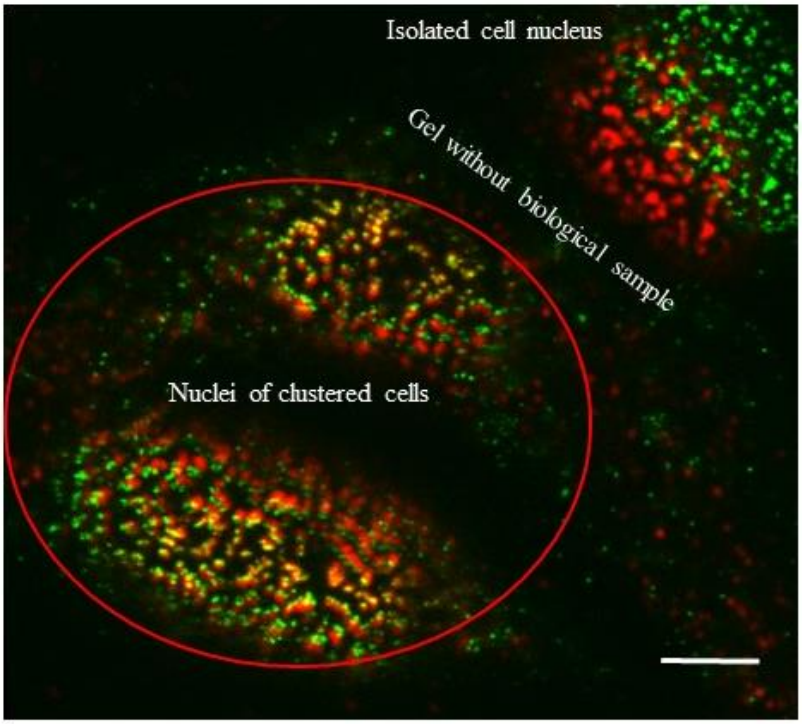

Fig. 62. The microscale analysis demonstrates an heterogenic expansion factor. The affine registration between Pre- (red) and Post-Ex (green) images shows a heterogenic expansion. Indeed, the inter-nuclei EF measured from cells belonging to the same cluster is 3.9 $\pm$ 0.2, while the inter-nuclei EF calculated from cells not belonging to the same cell cluster is (4.6 $\pm$ 0.1). We cannot record the third cells (on the top right), because the EF is higher respect to the clustered cells (measure performed with four different cells).

After demonstration the isotropic process for nuclear structures, my interest was focused on lamin A and its truncated mutation. Using ExM, I was able to image the 3D lamin A network with a resolution similar to STED nanoscopy. In addition, in lamin A-labelled sample, I noted particular invaginations called nucleoplasmic reticulum (NR). Based on the immunofluorescence staining, it is possible to distinguish type I and type II invaginations. The type II NR were acquired in expanded labelled sample for nuclear lamins. They were characterized by a diameter range of 100-500 µm, penetrated in the nucleus and contained INM, ONM, NPCs, and were invested with the nuclear lamins (*148, 149*). In addition, these channels present a cytoplasmic core, containing cytoskeletal elements such as microfilaments, intermediate filament and microtubules (*150*).

However, the formation of this nuclear structure remained largely unknown. An educated hypothesis is that the chromatin-lamins interactions and the large-scale rearrangements of chromatin can act as a pulling force. When the condensation and decondansation of chromatin occurred, the interaction of the NE proteins (in particular nuclear Lamins) could be pulled both into the nucleus and, hence, generated the nuclear invaginations (*149*) (Fig. 63). In accordance to this theory, I observed high density of chromatin-DNA in proximity to the type II NR (Fig. 57, B).

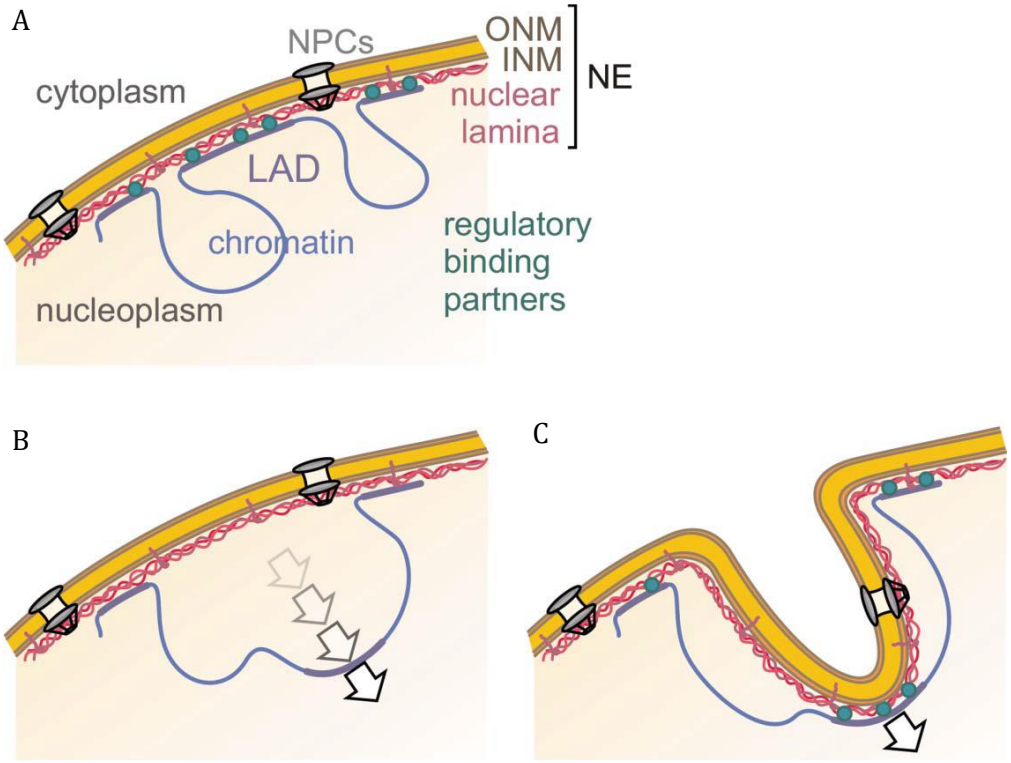

Fig. 63. Schematic illustration of the mechanism involved in the nucleoplasmic reticulum formation. (A) Chromatin regions (i.e., LADs) interact with the NE. several proteins of the

nuclear lamina and chromatin-binding partners dynamically regulated these interaction. (B) During genomic translocations, LADs detach from the NE, move into the nucleus, and eventually bind to the nucleolar periphery. (C) Alternatively, if the connection between LADs and the NE is strong, the NE might be pulled inward along with the LAD, forming a tube-like invagination (*149*).

ExM could help to investigate the aging process using the HGPS cell model. The global decrease in peripheral heterochromatin is concomitant with the misregulation and misexpression of several genes that are silenced in young healthy people (*151*) (Fig. 59). This important factor is probably the key to understand the molecular mechanism involved in aging. In addition, the nuclear distortion induced by deletion or mutation of nuclear lamins are also connected to several human diseases, including cancer and dementia. The nuclear shape is strictly dependent to the chromatin organization and gene positioning, and it is possible that the expression of mutated lamin A could alter this pattern, contributing to the neoplastic transformation. In fact, several cancers are characterized by similar characteristics. For example, loss of heterochromatin aggregates are characteristics features of papillary thyroid carcinoma, which is diagnosed on the basis of these changes (*152*). Indeed, recent studies demonstrated that progerin is expressed in several cancer cell lines, including PC-3, DU145, LN-CAP and MCF-7 cell. (*153, 154*). The high DNA damage susceptibility of these cells demonstrated that progerin has a central role also in tumorigenesis (Fig. 64). Although these mechanisms are still unclear, probably, in the future, the communication between pathologist, biophysics and molecular biology could find a specific and not invasive target therapy to cure these medical conditions.

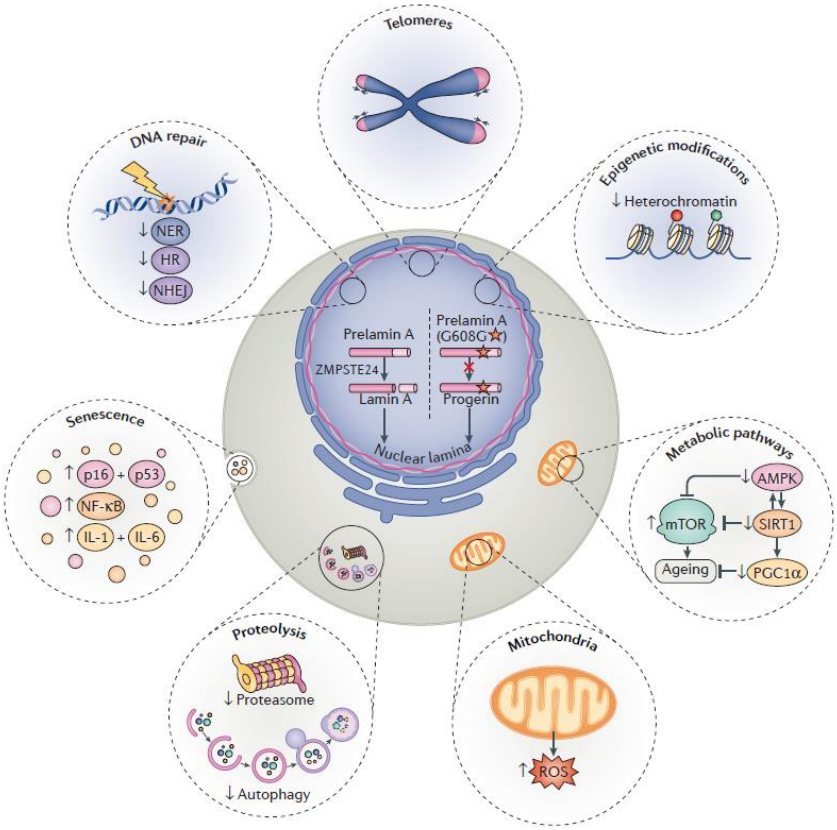

Fig. 64. The picture shows the cellular ageing defects that underlie premature ageing disorders, regular ageing, ageing-associated disease and, finally, tumorigenesis. These ageing defects include reduced DNA repair pathway efficiency, loss of genomic integrity, a global loss of heterochromatin, alterations in metabolic signaling, increased formation of reactive oxygen species (ROS) by mitochondria, reduced activity of proteostasis-promoting proteolytic pathways and activation of senescence pathways (*155*).

8 Bibliography

1. G. T. Di Francia, Super-gain antennas and optical resolving power. *Il Nuovo Cimento (1943-1954)* **9**, 426-438 (1952).
2. S. W. Hell, J. Wichmann, Breaking the diffraction resolution limit by stimulated emission: stimulated-emission-depletion fluorescence microscopy. *Optics Letters* **19**, 780-782 (1994).
3. C. J. R. Sheppard, T. Wilson, The theory of the direct-view confocal microscope. *Journal of Microscopy* **124**, 107-117 (1981).
4. S. Hell, E. H. K. Stelzer, Properties of a 4Pi confocal fluorescence microscope. *J. Opt. Soc. Am. A* **9**, 2159-2166 (1992).
5. Gustafsson, Agard, Sedat, I5M: 3D widefield light microscopy with better than 100 nm axial resolution. *Journal of Microscopy* **195**, 10-16 (1999).
6. F. Chen, P. W. Tillberg, E. S. Boyden, Expansion microscopy. *Science* **347**, 543 (2015).
7. I. Cainero *et al.*, Combining Expansion Microscopy and STED Nanoscopy for the Study of Cellular Organization. *Biophysical Journal* **112**, 140a (2017).
8. M. L. Watson, THE NUCLEAR ENVELOPE. *The Journal of Biophysical and Biochemical Cytology* **1**, 257 (1955).
9. N. Kubben, T. Misteli, Shared molecular and cellular mechanisms of premature ageing and ageing-associated diseases. *Nature Reviews Molecular Cell Biology* **18**, 595 (2017).
10. P. McClintock, *Fundamentals of fluorescence microscopy: exploring life with light, by Partha Pratim Mondal and Alberto Diaspro*. (2016), vol. 58, pp. 1.
11. E. Abbe, Beiträge zur Theorie des Mikroskops und der mikroskopischen Wahrnehmung. *Archiv für mikroskopische Anatomie* **9**, 413-418 (1873).
12. J. Tam, D. Merino, Stochastic optical reconstruction microscopy (STORM) in comparison with stimulated emission depletion (STED) and other imaging methods. *Journal of Neurochemistry* **135**, 643-658 (2015).
13. P. Engerer, C. Fecher, T. Misgeld, Super-resolution microscopy writ large. *Nature Biotechnology* **34**, 928 (2016).
14. K. Chung *et al.*, Structural and molecular interrogation of intact biological systems. *Nature* **497**, 332 (2013).
15. Etsuo A. Susaki *et al.*, Whole-Brain Imaging with Single-Cell Resolution Using Chemical Cocktails and Computational Analysis. *Cell* **157**, 726-739 (2014).
16. S. W. Hell, Strategy for far-field optical imaging and writing without diffraction limit. *Physics Letters A* **326**, 140-145 (2004).
17. S. W. Hell, Toward fluorescence nanoscopy. *Nature Biotechnology* **21**, 1347 (2003).
18. W. H. Stefan *et al.*, The 2015 super-resolution microscopy roadmap. *Journal of Physics D: Applied Physics* **48**, 443001 (2015).
19. P. de Boer, J. P. Hoogenboom, B. N. G. Giepmans, Correlated light and electron microscopy: ultrastructure lights up! *Nature Methods* **12**, 503 (2015).
20. U. Schnell, F. Dijk, K. A. Sjollema, B. N. G. Giepmans, Immunolabeling artifacts and the need for live-cell imaging. *Nature Methods* **9**, 152 (2012).
21. B. N. G. Giepmans, S. R. Adams, M. H. Ellisman, R. Y. Tsien, The Fluorescent Toolbox for Assessing Protein Location and Function. *Science* **312**, 217 (2006).
22. N. C. Shaner, G. H. Patterson, M. W. Davidson, Advances in fluorescent protein technology. *Journal of Cell Science* **120**, 4247 (2007).
23. C. J. Peddie *et al.*, Correlative and integrated light and electron microscopy of in-resin GFP fluorescence, used to localise diacylglycerol in mammalian cells. *Ultramicroscopy* **143**, 3-14 (2014).
24. K. T. Tokuyasu, A TECHNIQUE FOR ULTRACRYOTOMY OF CELL SUSPENSIONS AND TISSUES. *The Journal of Cell Biology* **57**, 551 (1973).

25. K. T. Tokuyasu, Immunochemistry on ultrathin frozen sections. *The Histochemical Journal* **12**, 381-403 (1980).
26. S. Watanabe *et al.*, Protein localization in electron micrographs using fluorescence nanoscopy. *Nature Methods* **8**, 80 (2010).
27. K. A. Sochacki, G. Shtengel, S. B. van Engelenburg, H. F. Hess, J. W. Taraska, Correlative super-resolution fluorescence and metal-replica transmission electron microscopy. *Nature Methods* **11**, 305 (2014).
28. A. Löschberger, C. Franke, G. Krohne, S. van de Linde, M. Sauer, Correlative super-resolution fluorescence and electron microscopy of the nuclear pore complex with molecular resolution. *Journal of Cell Science* **127**, 4351 (2014).
29. M. G. Paez-Segala *et al.*, Fixation-resistant photoactivatable fluorescent proteins for CLEM. *Nature methods* **12**, 215-218 (2015).
30. T. J. Chozinski *et al.*, Expansion Microscopy with Conventional Antibodies and Fluorescent Proteins. *Nature methods* **13**, 485-488 (2016).
31. P. W. Tillberg *et al.*, Protein-retention expansion microscopy of cells and tissues labeled using standard fluorescent proteins and antibodies. *Nature biotechnology* **34**, 987-992 (2016).
32. R. Gao, S. M. Asano, E. S. Boyden, Q&A: Expansion microscopy. *BMC Biology* **15**, 50 (2017).
33. J.-B. Chang *et al.*, Iterative expansion microscopy. *Nature Methods* **14**, 593 (2017).
34. T. Ku *et al.*, Multiplexed and scalable super-resolution imaging of three-dimensional protein localization in size-adjustable tissues. *Nature Biotechnology* **34**, 973 (2016).
35. F. Chen *et al.*, Nanoscale Imaging of RNA with Expansion Microscopy. *Nature methods* **13**, 679-684 (2016).
36. A. Kumar *et al.*, Influenza virus exploits tunneling nanotubes for cell-to-cell spread. *Scientific Reports* **7**, 40360 (2017).
37. Y. S. Zhang *et al.*, Hybrid Microscopy: Enabling Inexpensive High-Performance Imaging through Combined Physical and Optical Magnifications. *Scientific Reports* **6**, 22691 (2016).
38. Y. Zhao *et al.*, Nanoscale imaging of clinical specimens using pathology-optimized expansion microscopy. *Nature Biotechnology* **35**, 757 (2017).
39. E. F. Fornasiero, F. Opazo, Super-resolution imaging for cell biologists. *BioEssays* **37**, 436-451 (2015).
40. C. A. Wurm, D. Neumann, R. Schmidt, A. Egner, S. Jakobs, in *Live Cell Imaging: Methods and Protocols,* D. B. Papkovsky, Ed. (Humana Press, Totowa, NJ, 2010), pp. 185-199.
41. D. Hopwood, Cell and tissue fixation, 1972–1982. *The Histochemical Journal* **17**, 389-442 (1985).
42. D. Hopwood, Fixatives and fixation: a review. *The Histochemical Journal* **1**, 323-360 (1969).
43. D. Hopwood, Theoretical and practical aspects of glutaraldehyde fixation. *The Histochemical Journal* **4**, 267-303 (1972).
44. D. D. Sabatini, K. Bensch, R. J. Barrnett, CYTOCHEMISTRY AND ELECTRON MICROSCOPY. *The Journal of Cell Biology* **17**, 19 (1963).
45. K. A. K. Tanaka *et al.*, Membrane molecules mobile even after chemical fixation. *Nature Methods* **7**, 865 (2010).
46. D. R. Whelan, T. D. M. Bell, Image artifacts in Single Molecule Localization Microscopy: why optimization of sample preparation protocols matters. *Scientific Reports* **5**, 7924 (2015).
47. T. S. Reese, M. J. Karnovsky, FINE STRUCTURAL LOCALIZATION OF A BLOOD-BRAIN BARRIER TO EXOGENOUS PEROXIDASE. *The Journal of Cell Biology* **34**, 207 (1967).

48. Y. Matsubayashi, L. Iwai, H. Kawasaki, Fluorescent double-labeling with carbocyanine neuronal tracing and immunohistochemistry using a cholesterol-specific detergent digitonin. *Journal of Neuroscience Methods* **174**, 71-81 (2008).
49. C. A. Combs, H. Shroff, Fluorescence Microscopy: A Concise Guide to Current Imaging Methods. *Current Protocols in Neuroscience* **79**, 2.1.1-2.1.25 (2018).
50. R. R. Porter, The hydrolysis of rabbit γ-globulin and antibodies with crystalline papain. *Biochemical Journal* **73**, 119-127 (1959).
51. C. Hamers-Casterman *et al.*, Naturally occurring antibodies devoid of light chains. *Nature* **363**, 446 (1993).
52. A. D. Ellington, J. W. Szostak, In vitro selection of RNA molecules that bind specific ligands. *Nature* **346**, 818 (1990).
53. G. Lukinavičius *et al.*, Fluorogenic probes for live-cell imaging of the cytoskeleton. *Nature Methods* **11**, 731 (2014).
54. G. Lukinavičius *et al.*, SiR–Hoechst is a far-red DNA stain for live-cell nanoscopy. *Nature Communications* **6**, 8497 (2015).
55. O. Shimomura, F. H. Johnson, Y. Saiga, Extraction, Purification and Properties of Aequorin, a Bioluminescent Protein from the Luminous Hydromedusan, Aequorea. *Journal of Cellular and Comparative Physiology* **59**, 223-239 (1962).
56. D. C. Prasher, V. K. Eckenrode, W. W. Ward, F. G. Prendergast, M. J. Cormier, Primary structure of the Aequorea victoria green-fluorescent protein. *Gene* **111**, 229-233 (1992).
57. M. Chalfie, Y. Tu, G. Euskirchen, W. W. Ward, D. C. Prasher, Green fluorescent protein as a marker for gene expression. *Science* **263**, 802 (1994).
58. J. Lippincott-Schwartz, G. H. Patterson, Development and Use of Fluorescent Protein Markers in Living Cells. *Science* **300**, 87 (2003).
59. D. M. Shcherbakova, A. A. Shemetov, A. A. Kaberniuk, V. V. Verkhusha, Natural Photoreceptors as a Source of Fluorescent Proteins, Biosensors, and Optogenetic Tools. *Annual review of biochemistry* **84**, 519-550 (2015).
60. D. M. Shcherbakova, O. M. Subach, V. V. Verkhusha, Red Fluorescent Proteins: Advanced Imaging Applications and Future Design. *Angewandte Chemie International Edition* **51**, 10724-10738 (2012).
61. A. Keppler *et al.*, A general method for the covalent labeling of fusion proteins with small molecules in vivo. *Nature Biotechnology* **21**, 86 (2002).
62. H. Liu, M. Xu-Welliver, A. E. Pegg, The role of human O6-alkylguanine-DNA alkyltransferase in promoting 1,2-dibromoethane-induced genotoxicity in Escherichia coli. *Mutation Research/Fundamental and Molecular Mechanisms of Mutagenesis* **452**, 1-10 (2000).
63. A. Gautier *et al.*, An Engineered Protein Tag for Multiprotein Labeling in Living Cells. *Chemistry & Biology* **15**, 128-136 (2008).
64. P. A. Pellett *et al.*, Two-color STED microscopy in living cells. *Biomed. Opt. Express* **2**, 2364-2371 (2011).
65. T. J. Chozinski, L. A. Gagnon, J. C. Vaughan, Twinkle, twinkle little star: Photoswitchable fluorophores for super-resolution imaging. *FEBS Letters* **588**, 3603-3612 (2014).
66. A. El-Osta, A. P. Wolffe, DNA Methylation and Histone Deacetylation in the Control of Gene Expression: Basic Biochemistry to Human Development and Disease. *Gene Expression* **9**, 63-75 (2000).
67. K. H. Schreiber, B. K. Kennedy, When Lamins Go Bad: Nuclear Structure and Disease. *Cell* **152**, 1365-1375 (2013).
68. A. Haddow, What is Life? The Physical Aspect of the Living Cell. *Cancer Research* **5**, 670 (1945).
69. P.-O. Löwdin, Proton Tunneling in DNA and its Biological Implications. *Reviews of Modern Physics* **35**, 724-732 (1963).
70. M. Beck *et al.*, Nuclear Pore Complex Structure and Dynamics Revealed by Cryoelectron Tomography. *Science* **306**, 1387 (2004).

71. M. Beck, V. Lučić, F. Förster, W. Baumeister, O. Medalia, Snapshots of nuclear pore complexes in action captured by cryo-electron tomography. *Nature* **449**, 611 (2007).
72. L. J. Terry, E. B. Shows, S. R. Wente, Crossing the Nuclear Envelope: Hierarchical Regulation of Nucleocytoplasmic Transport. *Science* **318**, 1412 (2007).
73. E. C. Schirmer, L. Gerace, The nuclear membrane proteome: extending the envelope. *Trends in Biochemical Sciences* **30**, 551-558 (2005).
74. A. Mattout, T. Dechat, S. A. Adam, R. D. Goldman, Y. Gruenbaum, Nuclear lamins, diseases and aging. *Current Opinion in Cell Biology* **18**, 335-341 (2006).
75. S. Heessen, M. Fornerod, The inner nuclear envelope as a transcription factor resting place. *EMBO reports* **8**, 914 (2007).
76. K. L. Reddy, J. M. Zullo, E. Bertolino, H. Singh, Transcriptional repression mediated by repositioning of genes to the nuclear lamina. *Nature* **452**, 243 (2008).
77. A. Akhtar, S. M. Gasser, The nuclear envelope and transcriptional control. *Nature Reviews Genetics* **8**, 507 (2007).
78. E. C. Schirmer, R. Foisner, Proteins that associate with lamins: Many faces, many functions. *Experimental Cell Research* **313**, 2167-2179 (2007).
79. E. G. Neilan, Laminopathies, other progeroid disorders, and aging: Common pathogenic themes and possible treatments. *American Journal of Medical Genetics Part A* **149A**, 563-566 (2009).
80. H. J. Worman, G. Bonne, "Laminopathies": A wide spectrum of human diseases. *Experimental Cell Research* **313**, 2121-2133 (2007).
81. D. A. Starr, M. Han, ANChors away: an actin based mechanism of nuclear positioning. *Journal of Cell Science* **116**, 211 (2003).
82. K. Wilhelmsen, M. Ketema, H. Truong, A. Sonnenberg, KASH-domain proteins in nuclear migration, anchorage and other processes. *Journal of Cell Science* **119**, 5021 (2006).
83. Y. Gruenbaum, K. L. Wilson, A. Harel, M. Goldberg, M. Cohen, Review: Nuclear Lamins—Structural Proteins with Fundamental Functions. *Journal of Structural Biology* **129**, 313-323 (2000).
84. L. Pesce, M. Cozzolino, L. Lanzanò, A. Diaspro, P. Bianchini, Expansion Microscopy: A Tool to Investigate Hutchinson-Gilford Progeria Syndrome at Molecular Level. *Biophysical Journal* **114**, 536a (2018).
85. M. Peter *et al.*, Cloning and sequencing of cDNA clones encoding chicken lamins A and B1 and comparison of the primary structures of vertebrate A- and B-type lamins. *Journal of Molecular Biology* **208**, 393-404 (1989).
86. K. Vorburger, G. T. Kitten, E. A. Nigg, Modification of nuclear lamin proteins by a mevalonic acid derivative occurs in reticulocyte lysates and requires the cysteine residue of the C-terminal CXXM motif. *The EMBO Journal* **8**, 4007-4013 (1989).
87. D. A. Parry, J. F. Conway, P. M. Steinert, Structural studies on lamin. Similarities and differences between lamin and intermediate-filament proteins. *Biochemical Journal* **238**, 305-308 (1986).
88. I. Krimm *et al.*, The Ig-like Structure of the C-Terminal Domain of Lamin A/C, Mutated in Muscular Dystrophies, Cardiomyopathy, and Partial Lipodystrophy. *Structure* **10**, 811-823 (2002).
89. T. Dechat, S. A. Adam, P. Taimen, T. Shimi, R. D. Goldman, Nuclear Lamins. *Cold Spring Harbor Perspectives in Biology* **2**, a000547 (2010).
90. A. E. Rusiñol, M. S. Sinensky, Farnesylated lamins, progeroid syndromes and farnesyl transferase inhibitors. *Journal of Cell Science* **119**, 3265 (2006).
91. Douglas P. Corrigan *et al.*, Prelamin A endoproteolytic processing in vitro by recombinant Zmpste24. *Biochemical Journal* **387**, 129 (2005).
92. A. M. Winter-Vann, P. J. Casey, Post-prenylation-processing enzymes as new targets in oncogenesis. *Nature Reviews Cancer* **5**, 405 (2005).
93. T. Dechat *et al.*, Nuclear lamins: major factors in the structural organization and function of the nucleus and chromatin. *Genes & Development* **22**, 832-853 (2008).

94. L. Guelen *et al.*, Domain organization of human chromosomes revealed by mapping of nuclear lamina interactions. *Nature* **453**, 948 (2008).
95. L. Schermelleh *et al.*, Subdiffraction Multicolor Imaging of the Nuclear Periphery with 3D Structured Illumination Microscopy. *Science (New York, N.Y.)* **320**, 1332-1336 (2008).
96. P. Scaffidi, T. Misteli, Lamin A-Dependent Nuclear Defects in Human Aging. *Science* **312**, 1059 (2006).
97. V. Nikolova *et al.*, Defects in nuclear structure and function promote dilated cardiomyopathy in lamin A/C–deficient mice. *The Journal of Clinical Investigation* **113**, 357-369 (2004).
98. T. Sullivan *et al.*, Loss of a-Type Lamin Expression Compromises Nuclear Envelope Integrity Leading to Muscular Dystrophy. *The Journal of Cell Biology* **147**, 913 (1999).
99. D. K. Shumaker *et al.*, Mutant nuclear lamin A leads to progressive alterations of epigenetic control in premature aging. *Proceedings of the National Academy of Sciences* **103**, 8703 (2006).
100. J. S. H. Lee *et al.*, Nuclear Lamin A/C Deficiency Induces Defects in Cell Mechanics, Polarization, and Migration. *Biophysical Journal* **93**, 2542-2552 (2007).
101. F. Houben, F. C. S. Ramaekers, L. H. E. H. Snoeckx, J. L. V. Broers, Role of nuclear lamina-cytoskeleton interactions in the maintenance of cellular strength. *Biochimica et Biophysica Acta (BBA) - Molecular Cell Research* **1773**, 675-686 (2007).
102. K. N. Dahl, A. J. S. Ribeiro, J. Lammerding, Nuclear shape, mechanics, and mechanotransduction. *Circulation research* **102**, 1307-1318 (2008).
103. K. L. Wydner, J. A. McNeil, F. Lin, H. J. Worman, J. B. Lawrence, Chromosomal Assignment of Human Nuclear Envelope Protein Genes LMNA, LMNB1, and LBR by Fluorescencein SituHybridization. *Genomics* **32**, 474-478 (1996).
104. G. Bonne *et al.*, Mutations in the gene encoding lamin A/C cause autosomal dominant Emery-Dreifuss muscular dystrophy. *Nature Genetics* **21**, 285 (1999).
105. A. E. H. Emery, Emery–Dreifuss muscular dystrophy – a 40 year retrospective. *Neuromuscular Disorders* **10**, 228-232 (2000).
106. D. Fatkin *et al.*, Missense Mutations in the Rod Domain of the Lamin A/C Gene as Causes of Dilated Cardiomyopathy and Conduction-System Disease. *New England Journal of Medicine* **341**, 1715-1724 (1999).
107. A. Muchir *et al.*, Identification of mutations in the gene encoding lamins A/C in autosomal dominant limb girdle muscular dystrophy with atrioventricular conduction disturbances (LGMD1B). *Human Molecular Genetics* **9**, 1453-1459 (2000).
108. S. N. Jackson *et al.*, A defect in the regional deposition of adipose tissue (partial lipodystrophy) is encoded by a gene at chromosome 1q. *American journal of human genetics* **63**, 534-540 (1998).
109. J. M. Peters *et al.*, Localization of the gene for familial partial lipodystrophy (Dunnigan variety) to chromosome 1q21–22. *Nature Genetics* **18**, 292 (1998).
110. H. Cao, R. Hegele, *Nuclear lamin A/C R482Q mutation in Canadian kindreds with Dunnigan-type familial partial lipodystrophy*. (2000), vol. 9.
111. R. A. Speckman *et al.*, Mutational and haplotype analyses of families with familial partial lipodystrophy (Dunnigan variety) reveal recurrent missense mutations in the globular C-terminal domain of lamin A/C. *American journal of human genetics* **66**, 1192-1198 (2000).
112. C. Vigouroux *et al.*, Lamin A/C gene: sex-determined expression of mutations in Dunnigan-type familial partial lipodystrophy and absence of coding mutations in congenital and acquired generalized lipoatrophy. *Diabetes* **49**, 1958 (2000).
113. M. Tazir *et al.*, Phenotypic variability in autosomal recessive axonal Charcot–Marie–Tooth disease due to the R298C mutation in lamin A/C. *Brain* **127**, 154-163 (2004).

114. J. Hutchinson, Congenital Absence of Hair and Mammary Glands with Atrophic Condition of the Skin and its Appendages, in a Boy whose Mother had been almost wholly Bald from Alopecia Areata from the age of Six. *Medico-chirurgical transactions* **69**, 473-477 (1886).
115. V. A. McKusick, The Gordon Wilson Lecture: The clinical legacy of Jonathan Hutchinson (1828-1913): syndromology and dysmorphology meet genomics. *Transactions of the American Clinical and Climatological Association* **116**, 15-38 (2005).
116. F. L. DeBusk, The Hutchinson-Gilford progeria syndrome: Report of 4 cases and review of the literature. *The Journal of Pediatrics* **80**, 697-724 (1972).
117. M. Eriksson *et al.*, Recurrent de novo point mutations in lamin A cause Hutchinson–Gilford progeria syndrome. *Nature* **423**, 293 (2003).
118. A. De Sandre-Giovannoli *et al.*, Lamin A Truncation in Hutchinson-Gilford Progeria. *Science* **300**, 2055 (2003).
119. C. L. Moulson *et al.*, Increased progerin expression associated with unusual LMNA mutations causes severe progeroid syndromes. *Human Mutation* **28**, 882-889 (2007).
120. J. Lammerding *et al.*, Lamin A/C deficiency causes defective nuclear mechanics and mechanotransduction. *The Journal of Clinical Investigation* **113**, 370-378 (2004).
121. S. H. Yang *et al.*, Blocking protein farnesyltransferase improves nuclear blebbing in mouse fibroblasts with a targeted Hutchinson–Gilford progeria syndrome mutation. *Proceedings of the National Academy of Sciences of the United States of America* **102**, 10291 (2005).
122. B. C. Capell *et al.*, Inhibiting farnesylation of progerin prevents the characteristic nuclear blebbing of Hutchinson-Gilford progeria syndrome. *Proceedings of the National Academy of Sciences of the United States of America* **102**, 12879 (2005).
123. B. Liu *et al.*, Genomic instability in laminopathy-based premature aging. *Nature Medicine* **11**, 780 (2005).
124. M. A. Merideth *et al.*, Phenotype and Course of Hutchinson–Gilford Progeria Syndrome. *New England Journal of Medicine* **358**, 592-604 (2008).
125. J.-H. Baek, T. McKenna, M. Eriksson. (2013), pp. 65-87.
126. D. McClintock *et al.*, The Mutant Form of Lamin A that Causes Hutchinson-Gilford Progeria Is a Biomarker of Cellular Aging in Human Skin. *PLOS ONE* **2**, e1269 (2007).
127. M. Chaouch *et al.*, The phenotypic manifestations of autosomal recessive axonalCharcot–Marie–Tooth due to a mutation in Lamin A/C gene. *Neuromuscular Disorders* **13**, 60-67 (2003).
128. A. E. H. Emery, Emery–Dreifuss muscular dystrophy – a 40 year retrospective. *Neuromuscular Disorders* **10**, 228-232 (2000).
129. G. Novelli *et al.*, Mandibuloacral dysplasia is caused by a mutation in LMNA-encoding lamin A/C. *American journal of human genetics* **71**, 426-431 (2002).
130. J. A. Towbin, N. E. Bowles, The failing heart. *Nature* **415**, 227 (2002).
131. D. M. Shcherbakova *et al.*, Bright monomeric near-infrared fluorescent proteins as tags and biosensors for multiscale imaging. *Nature Communications* **7**, 12405 (2016).
132. L.-B. Weiswald, D. Bellet, V. Dangles-Marie, Spherical cancer models in tumor biology. *Neoplasia (New York, N.Y.)* **17**, 1-15 (2015).
133. M. Grabenbauer, in *Methods in Cell Biology,* T. Müller-Reichert, P. Verkade, Eds. (Academic Press, 2012), vol. 111, pp. 117-138.
134. M. Grabenbauer *et al.*, Correlative microscopy and electron tomography of GFP through photooxidation. *Nature Methods* **2**, 857 (2005).
135. V. Liss, B. Barlag, M. Nietschke, M. Hensel, Self-labelling enzymes as universal tags for fluorescence microscopy, super-resolution microscopy and electron microscopy. *Scientific Reports* **5**, 17740 (2015).

136. H. D. Ou *et al.*, ChromEMT: Visualizing 3D chromatin structure and compaction in interphase and mitotic cells. *Science* **357**, (2017).
137. M. H. Ellisman, T. J. Deerinck, X. Shu, G. E. Sosinsky, in *Methods in Cell Biology,* T. Müller-Reichert, P. Verkade, Eds. (Academic Press, 2012), vol. 111, pp. 139-155.
138. P. Bianchini *et al.*, STED nanoscopy: a glimpse into the future. *Cell and Tissue Research* **360**, 143-150 (2015).
139. P. Scaffidi, T. Misteli, Reversal of the cellular phenotype in the premature aging disease Hutchinson-Gilford progeria syndrome. *Nature medicine* **11**, 440-445 (2005).
140. J. Schindelin *et al.*, Fiji - an Open Source platform for biological image analysis. *Nature methods* **9**, 10.1038/nmeth.2019 (2012).
141. P. Thevenaz, U. E. Ruttimann, M. Unser, A pyramid approach to subpixel registration based on intensity. *IEEE Transactions on Image Processing* **7**, 27-41 (1998).
142. T. J. Dougherty, PHOTODYNAMIC THERAPY. *Photochemistry and Photobiology* **58**, 895-900 (1993).
143. P. Agostinis *et al.*, Photodynamic therapy of cancer: an update. *CA: a cancer journal for clinicians* **61**, 250-281 (2011).
144. T. C. Walther *et al.*, The nucleoporin Nup153 is required for nuclear pore basket formation, nuclear pore complex anchoring and import of a subset of nuclear proteins. *The EMBO Journal* **20**, 5703-5714 (2001).
145. M. J. Sarmento *et al.*, Exploiting the tunability of stimulated emission depletion microscopy for super-resolution imaging of nuclear structures. *Nature Communications* **9**, 3415 (2018).
146. G. Vicidomini *et al.*, Sharper low-power STED nanoscopy by time gating. *Nature Methods* **8**, 571 (2011).
147. T. Shimi *et al.*, Structural organization of nuclear lamins A, C, B1, and B2 revealed by superresolution microscopy. *Molecular biology of the cell* **26**, 4075-4086 (2015).
148. A. Malhas, C. Goulbourne, D. J. Vaux, The nucleoplasmic reticulum: form and function. *Trends in Cell Biology* **21**, 362-373 (2011).
149. I. Schoen, L. Aires, J. Ries, V. Vogel, Nanoscale invaginations of the nuclear envelope: Shedding new light on wormholes with elusive function. *Nucleus* **8**, 506-514 (2017).
150. B. H. Clubb, M. Locke, 3T3 cells have nuclear invaginations containing F-actin. *Tissue and Cell* **30**, 684-691 (1998).
151. E. L. Greer, Y. Shi, Histone methylation: a dynamic mark in health, disease and inheritance. *Nature Reviews Genetics* **13**, 343 (2012).
152. D. Zink, A. H. Fischer, J. A. Nickerson, Nuclear structure in cancer cells. *Nature Reviews Cancer* **4**, 677 (2004).
153. Y. Tang, Y. Chen, H. Jiang, D. Nie, Promotion of tumor development in prostate cancer by progerin. *Cancer cell international* **10**, 47-47 (2010).
154. K. M. Sakthivel, P. Sehgal, A Novel Role of Lamins from Genetic Disease to Cancer Biomarkers. *Oncology reviews* **10**, 309-309 (2016).
155. N. Kubben, T. Misteli, *Shared molecular and cellular mechanisms of premature ageing and ageing-associated diseases*. (2017), vol. 18.